

Optimierung der Vortexdetektion in SU(2)-QCD

Die Gestützte Maximale Zentrums Eichung

DISSERTATION

zur Erlangung des akademischen Grades

Doktor der Naturwissenschaften

eingereicht von

Dipl.-Ing. Rudolf Golubich, BSc.

Matrikelnummer 01028778

an der Fakultät für Physik

der Technischen Universität Wien

Betreuung: Ao.Univ.Prof.i.R. Dipl.-Ing. Dr.techn. Manfred Faber

Diese Dissertation haben begutachtet:

Vitaly Bornyakov

Wolfgang Lucha

Wien, 28. Jänner 2022



Rudolf Golubich

Improvement of vortex detection in SU(2)-QCD

The Guided Maximal Center Gauge (GMCG)

DISSERTATION

submitted in partial fulfillment of the requirements for the degree of

Doktor der Naturwissenschaften

by

Dipl.-Ing. Rudolf Golubich, BSc.

Registration Number 01028778

to the Faculty of Physics

at the TU Wien

Advisor: Ao.Univ.Prof.i.R. Dipl.-Ing. Dr.techn. Manfred Faber

The dissertation has been reviewed by:

Vitaly Bornyakov

Wolfgang Lucha

Vienna, 28th January, 2022



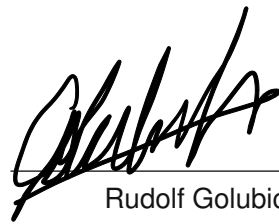
Rudolf Golubich

Erklärung zur Verfassung der Arbeit

Dipl.-Ing. Rudolf Golubich, BSc.

Hiermit erkläre ich, dass ich diese Arbeit selbständig verfasst habe, dass ich die verwendeten Quellen und Hilfsmittel vollständig angegeben habe und dass ich die Stellen der Arbeit – einschließlich Tabellen, Karten und Abbildungen –, die anderen Werken oder dem Internet im Wortlaut oder dem Sinn nach entnommen sind, auf jeden Fall unter Angabe der Quelle als Entlehnung kenntlich gemacht habe.

Wien, 28. Jänner 2022



Rudolf Golubich

Kurzfassung

Die Quantenchromodynamik beschreibt das Verhalten von Quarks, den Bestandteilen der Nukleonen, und deren Wechselwirkung mit Gluonen, den Trägern der starken Kernkraft. Sie beschreibt, wie die Nukleonen gebildet und Atomkerne zusammengehalten werden. Die Quantenchromodynamik ist kaum störungstheoretisch lösbar: nur numerische Näherungen sind zugänglich.

Die Tatsache, dass keine freien Quarks beobachtet werden können wird als *Quark-Einschluss* oder *Farb-Einschluss* bezeichnet.

Eine mögliche Erklärung hierfür bietet das *Zentrumsvortexmodell*, indem es annimmt, dass Zentrumsvortices, geschlossene farb-magnetische Flusslinien, das Vakuum durchdringen.

Um dieses Modell zu testen, müssen Zentrums-Vortices in Gittersimulationen identifiziert werden. Dies geschieht in einer bestimmten Eichung durch Projektion auf die Zentrumsfreiheitsgrade. Die Vortexdetektion kann durch Uneindeutigkeiten bei der Eichung, sogenannte *Gribov-Probleme*, gestört werden und wird ebenso in glatten Konfigurationen problematisch.

Durch Verwendung von *nicht-trivialen Zentrumsregionen*, dh Gebieten, deren Rand zu einem nicht-trivialen Zentrumsselement ausgewertet wird, können die Methoden der Vortexdetektion verbessert werden: Wir präsentieren die *Gestützte Maximale Zentrumszeichnung*.

Abstract

Quantum Chromodynamics governs the behaviour of Quarks, the constituents of the nucleons and their interaction with Gluons, the carrier of the strong force. It describes how the nucleons are formed and where the nuclear force that holds together nuclei arises. Quantum Chromodynamics is highly non-perturbative: only numerical approximations are accessible.

The fact that no free quarks can be observed is called *quark confinement* or *color confinement*.

The *center vortex model* gives a possible explanation for this by stating that center vortices, closed color magnetic flux lines, percolate the vacuum.

To test this model, center vortices need to be detected within lattice simulations. This is done in a specific gauge by projection on the center degrees of freedom. The vortex detection can be troubled by gauge ambiguities, so called *Gribov problems* and it can become problematic in smooth configurations.

By usage of *non-trivial center regions*, that is, regions whose boundary evaluates to a non-trivial center element, the vortex detection procedures can be improved: We present the *Guided Maximal Center Gauge*.

Contents

Kurzfassung	vii
Abstract	ix
Contents	xi
1 Introduction	1
2 Quantum Chromodynamics	3
2.1 Approaching the lattice	16
2.2 From center symmetry to center vortices	24
2.3 Implementing the gluonic path integral	27
2.4 Observables on the lattice	31
3 Detecting center vortices	37
3.1 Center regions	38
3.2 P-Vortices	46
3.3 Thick vortices	53
3.4 Achieved improvements and restrictions	54
4 Algorithmic restrictions from vortex properties	59
4.1 Thickness and size	59
4.2 Color structure	69
4.3 Combined restrictions	79
5 Future outlook and perspectives	81
List of Figures	83
List of Algorithms	85
Bibliography	87

Introduction

The nucleons and other non-elementary particles are considered composite particles of color-neutral charge that are built from colored elementary particles so that their total color-charges add up to neutral color, white, see Fig. 1.1. The two simplest composite



Figure 1.1: In Quantum Chromodynamics it is assumed that all composite particles are built by color elementary particles so that their total color charge sums up to white: We speak of *color singlets*. This can be achieved by adding three (anti-)colors or by combining a color and its anti-color.

particles are either built by three colored particles (referred to as *Baryons*) or by a colored particle and an anti-colored anti-particle (referred to as *Mesons*). The elementary colored particles are called *Quarks*. Quantum Chromodynamics is the theory that describes the interaction of these quarks via gluons, the carrier of the strong nuclear force.

In comparison to the electric charge giving rise to electromagnetism, the color charge is more complex: It gives rise to 8 different color-electric and color-magnetic fields that interact with each other. In electrodynamics free electric charges can be experimentally observed, whereas the color charge is not directly accessible to our observation: We only see white particles. This fact is called *color-confinement* or *quark-confinement*. An explanation for this confinement is given by the assumption of a linearly (or stronger) growing quark anti-quark potential: pulling a quark anti-quark pair apart, the potential energy rises until another quark anti-quark pair can emerge from the vacuum. Hence, no single quark can be observed. This is referred to as *string breaking* and schematically depicted in Fig. 1.2.

The *center vortex model* is a model of the confining forces that cause the collimation of the color-flux into flux tubes. It can explain confinement and chiral symmetry breaking

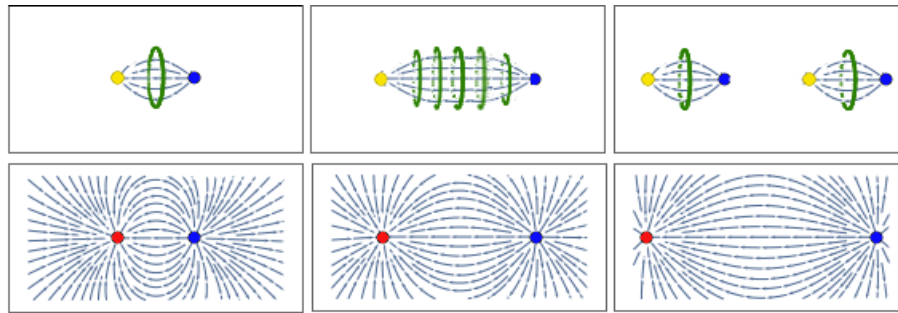


Figure 1.2: In the upper part the *string-breaking* is shown from left to right for a quark anti-quark pair that gets pulled apart. The color electric flux lines between color charges are shown as blue lines. They are collimated into a flux tube by color-magnetic monopoles moving along the world lines that are shown in green. The lower part shows the situation for electrodynamics where no confinement occurs and the particles can be pulled apart arbitrarily far.

that is related to the mass of the nucleons as will be shown later. The model assumes that confinement is caused by excitations of the center degrees of freedom, that is, by center vortices: closed color magnetic flux lines that evolve in the vacuum and collimate the color electric flux into flux tubes.

To allow for better tests of the center vortex model it is necessary to detect center vortices in lattice simulations. This vortex detection can be troubled not only by *Gribov copies* [1, 2] but by high smoothness of the lattice. We will present a method of vortex detection that can overcome some of the troubles by usage of *center regions*: the *Guided Maximal Center Gauge* (GMCG).

First we will relate Quarks to ladder-operators that are constructed from the algebra of $SU(2)$ and introduce gauge invariance which will lead us to Gluons. This clears the way for the Lagrangian of Quantum Chromodynamics and allows to make a rough introduction of the concepts of *regularization*, *renormalization* and the *running coupling*. Then we will discuss in short how Chiral symmetry is related to the particle mass and to center vortices.

In the next step we will let find the Lagrangian onto the lattice and prepare the way for quantisation via the path integral. We will discuss discretization effects and finite size effects and introduce the concept of center vortices more formally. Then we will show how the path integral can be solved on the lattice and how different observables are evaluated within this formalism.

This will be followed by a discussion of vortex detection with introducing the concept of *center regions* and continued with *P-vortices* until our method how to detect *thick vortices* is presented. Analyzing some properties of vortices we can then identify for which choice of parameters our procedures work best and where there is still potential for further improvements.

We will end with a short discussion of possibilities for such further improvements and potential for future research.

Quantum Chromodynamics

We will now first introduce the Lagrangian of QCD step by step based on $SU(3)$ invariance. On this way we also take a look at the group theoretical aspects that define the properties of the fundamental particles in quantum chromodynamics: the quarks. Gluons will be introduced to ensure the invariance of the Lagrangian and the interaction of all those particles will be discussed before we show how the lattice formalisation allows numerical solutions. For the further parts of this work only the gluonic part of a simplified model of QCD will be of interest. Despite that, we first carry along the fermionic parts and the whole $SU(3)$ before simplifying to our final model of gluonic $SU(2)$ QCD.

We start from the Lagrangian of relativistic massive particles, $\bar{\psi}_f (i \gamma_\mu \partial^\mu - m_f) \psi_f$, with $\bar{\psi}_f = \psi_f^\dagger \gamma_0$ and the index $f \in \{\text{up, down, strange}\}$ distinguishing the different quark flavors. The Gamma matrices γ_μ generate a *Clifford algebra*, that is, they are defined by their anti-commutation relation

$$\{\gamma^\mu, \gamma^\nu\} = \gamma^\mu \gamma^\nu + \gamma^\nu \gamma^\mu \stackrel{!}{=} 2\eta^{\mu\nu} \mathbb{1}_4, \quad (2.1)$$

with Minkowskian metric $\eta^{\mu\nu} = \text{diag}(1, -1, -1, -1)$,

$$\gamma_\mu = \eta_{\mu\nu} \gamma^\nu. \quad (2.2)$$

In *Dirac representation* the Gamma matrices are given by

$$\gamma^0 = \begin{pmatrix} \mathbb{1}_2 & \mathbb{0}_2 \\ \mathbb{0}_2 & -\mathbb{1}_2 \end{pmatrix} \quad \text{and} \quad \gamma^{k \in \{1, 2, 3\}} = \begin{pmatrix} \mathbb{0}_2 & \sigma_k \\ -\sigma_k & \mathbb{0}_2 \end{pmatrix}, \quad (2.3)$$

with Pauli matrices σ_k in turn given by

$$\sigma_1 = \begin{pmatrix} 0 & 1 \\ 1 & 0 \end{pmatrix}, \quad \sigma_2 = \begin{pmatrix} 0 & -i \\ i & 0 \end{pmatrix}, \quad \sigma_3 = \begin{pmatrix} 1 & 0 \\ 0 & -1 \end{pmatrix}. \quad (2.4)$$

The spinors ψ_f can be represented by four dimensional vectors and give rise to the conserved *Dirac current*

$$j_f = \bar{\psi}_f \gamma^\mu \psi_f, \quad (2.5)$$

the current of the different flavored quarks.

Quantum Chromodynamics is reached by enforcing a local $SU(3)$ invariance: Transforming the spinors ψ_{fc} with $\Omega(x^\mu) = e^{i g \alpha_i(x^\mu) t_i} \in SU(3)$, with $\alpha_i(x^\mu) t_i \in su(3)$ working on the additional color index c , should let the Lagrangian invariant. It yields

$$\psi_{fc} \rightarrow \psi'_{fc'} = \Omega_{c'}^c(x^\mu) \psi_{fc} \quad \text{and} \quad \bar{\psi}_{fc} \rightarrow \bar{\psi}'_{fc'} = \bar{\psi}_{fc} \Omega_{c'}^\dagger(x^\mu), \quad (2.6)$$

with α_i the transformation parameters and $\text{Tr}(t_i) = 0$. The generators t_i can be explicitly given by the *Gell-Mann matrices* with a factor $\frac{1}{2}$ as

$$\begin{aligned} t_1 &= \frac{1}{2} \begin{pmatrix} 0 & 1 & 0 \\ 1 & 0 & 0 \\ 0 & 0 & 0 \end{pmatrix}, & t_2 &= \frac{1}{2} \begin{pmatrix} 0 & -i & 0 \\ i & 0 & 0 \\ 0 & 0 & 0 \end{pmatrix}, & t_3 &= \frac{1}{2} \begin{pmatrix} 1 & 0 & 0 \\ 0 & -1 & 0 \\ 0 & 0 & 0 \end{pmatrix}, \\ t_4 &= \frac{1}{2} \begin{pmatrix} 0 & 0 & 1 \\ 0 & 0 & 0 \\ 1 & 0 & 0 \end{pmatrix}, & t_5 &= \frac{1}{2} \begin{pmatrix} 0 & 0 & -i \\ 0 & 0 & 0 \\ i & 0 & 0 \end{pmatrix}, & & \\ t_6 &= \frac{1}{2} \begin{pmatrix} 0 & 0 & 0 \\ 0 & 0 & 1 \\ 0 & 1 & 0 \end{pmatrix}, & t_7 &= \frac{1}{2} \begin{pmatrix} 0 & 0 & 0 \\ 0 & 0 & -i \\ 0 & i & 0 \end{pmatrix}, & t_8 &= \frac{1}{2\sqrt{3}} \begin{pmatrix} 1 & 0 & 0 \\ 0 & 1 & 0 \\ 0 & 0 & -2 \end{pmatrix}. \end{aligned} \quad (2.7)$$

They act on the color index $c \in \{\text{red, green, blue}\}$ with

$$\text{red} \hat{=} \begin{pmatrix} 1 \\ 0 \\ 0 \end{pmatrix}, \quad \text{green} \hat{=} \begin{pmatrix} 0 \\ 1 \\ 0 \end{pmatrix}, \quad \text{blue} \hat{=} \begin{pmatrix} 0 \\ 0 \\ 1 \end{pmatrix}. \quad (2.8)$$

This new index corresponds to the relevant charge of strong interaction: the color charge. We will now explore some of the symmetries within the aforementioned matrices to identify properties of the particles that we are dealing with before we finish the construction of the Lagrangian. We assume that the strong interaction binds together the nucleons, but does not distinguish between neutron and proton. Looking for the constituents of the nucleons, this arising $SU(2)$ symmetry has to be respected and we will uncover it now.

That two of the matrices can be simultaneously diagonalized gives rise to two quantum numbers:

- The eigenvalues of t_3 define the *Isospin* T_3 ,
- the eigenvalues of $\frac{2}{\sqrt{3}} t_8$ define the *Hypercharge* Y ,

with the remaining six matrices we can construct ladder-operators that act on these two quantum numbers:

- $T_{\pm} := t_1 \pm i t_2$ causes $T_3 \rightarrow T_3 \pm 1$,
- $V_{\pm} := t_4 \pm i t_5$ causes $T_3 \rightarrow T_3 \pm \frac{1}{2}$ and $Y \rightarrow Y \pm 1$,
- $U_{\pm} := t_6 \pm i t_7$ causes $T_3 \rightarrow T_3 \mp \frac{1}{2}$ and $Y \rightarrow Y \pm 1$.

We denote with T_3 and Y the corresponding matrices as well as the eigenvalues of respective eigenstates. It should be clear from the context whether the matrix or the eigenvalue is meant. The influence of these ladder operators on Isospin and Hypercharge can also be seen from their commutation relations

$$\begin{aligned}
 [T_3, T_{\pm}] &= \pm T_{\pm}, & [T_3, V_{\pm}] &= \pm \frac{1}{2} V_{\pm}, & [T_3, U_{\pm}] &= \mp \frac{1}{2} U_{\pm} \\
 [Y, T_{\pm}] &= 0, & [Y, V_{\pm}] &= \pm V_{\pm}, & [Y, U_{\pm}] &= \pm U_{\pm}.
 \end{aligned}
 \tag{2.9}$$

These relations are depicted in Fig. 2.1 where each arrow shows how the respective ladder-operator changes the two quantum numbers. By restricting these ladder operators

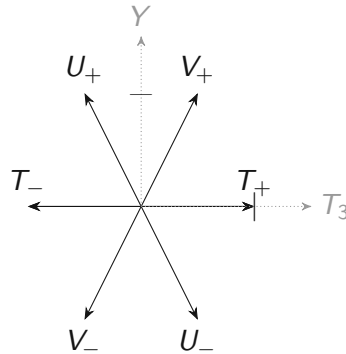


Figure 2.1: The effect of the ladder operators on Isospin T_3 and Hypercharge Y is shown.

one can uncover two further $su(2)$ algebras: The $su(2)$ Isospin algebra that is generated by

$$V_1 = t_1, \quad V_2 = t_2, \quad V_3 = \frac{1}{2} \begin{pmatrix} 1 & 0 & 0 \\ 0 & 0 & 0 \\ 0 & 0 & -1 \end{pmatrix} = \frac{1}{2} T_3 + \frac{3}{4} Y.
 \tag{2.10}$$

And the U-spin $SU(2)$ generated by

$$U_1 = t_6, \quad U_2 = t_7, \quad U_3 = \frac{1}{2} \begin{pmatrix} 0 & 0 & 0 \\ 0 & 1 & 0 \\ 0 & 0 & -1 \end{pmatrix} = -\frac{1}{2} T_3 + \frac{3}{4} Y.
 \tag{2.11}$$

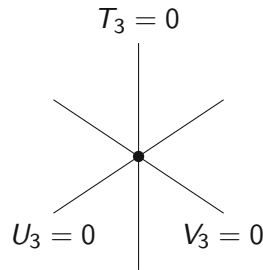


Figure 2.2: The threefold symmetry of SU(3) that arises from the SU(2) subgroups.

These $su(2)$ sub-algebras give rise to a three fold symmetry as depicted in Fig. 2.2. This symmetry is related to the particles we are interested in. They arise as the lowest non-vanishing eigenvectors of T_3 and Y and span the triplet $\mathbf{3}$ that is depicted in the left side of Fig. 2.3. The anti-particles span an anti-triplet $\bar{\mathbf{3}}$ that is depicted on the right

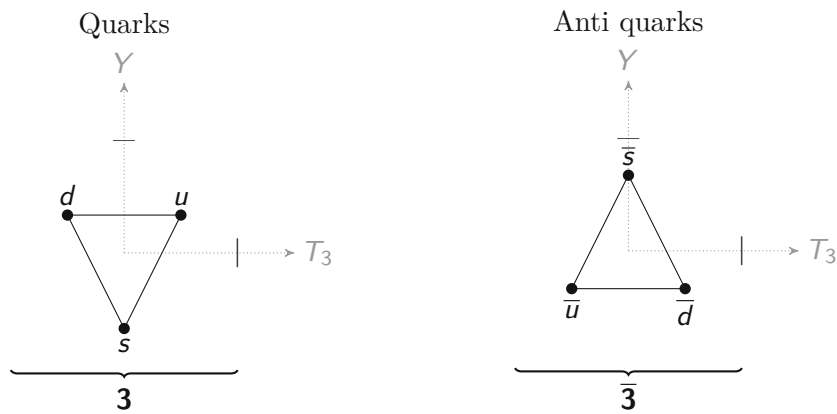


Figure 2.3: Isospin T_3 and Hypercharge Y of the constituents of the triplet $\mathbf{3}$ and anti-triplet $\bar{\mathbf{3}}$. side. It can be reached from the generators of the antiparticles $\bar{t}_i = -t_i^*$. The respective eigenvalues T_3 and Y are related to the electric charge Q via the Gell-Mann–Nishijima formula

$$Q = T_3 + \frac{1}{2}Y \quad (2.12)$$

and we obtain the properties of quarks as given in the following table 2.1 which is complemented by some experimental data. The mass differences cause that the SU(2) symmetries are not exact. This is the reason why we took into account only the three lightest quarks: For them, the SU(2) symmetries are less disturbed. The quarks are considered as spin $\frac{1}{2}$ particles and are the constituents of a vast number of particles, such as Mesons (built by a quark anti-quark pair) or Baryons (built by three quarks). The Nucleons are considered being built by

- the three quarks udd for a Proton with mass $m_p = 938.272081(6)$ MeV,
- the three quarks uud for a neutron with mass $m_n = 939.565413(6)$ MeV,

Quarks	u	d	s	\bar{u}	\bar{d}	\bar{s}
Isospin T_3	$+\frac{1}{2}$	$-\frac{1}{2}$	0	$-\frac{1}{2}$	$+\frac{1}{2}$	0
Hypercharge Y	$+\frac{1}{3}$	$+\frac{1}{3}$	$-\frac{2}{3}$	$-\frac{1}{3}$	$-\frac{1}{3}$	$+\frac{2}{3}$
Electric charge Q [e]	$+\frac{2}{3}$	$-\frac{1}{3}$	$-\frac{1}{3}$	$-\frac{2}{3}$	$+\frac{1}{3}$	$+\frac{1}{3}$
Mass m [MeV]	$2.16^{+0.49}_{-0.26}$	$4.67^{+0.48}_{-0.17}$	93^{+11}_{-5}	$= m_u$	$= m_d$	$= m_s$

Table 2.1: Some properties of quarks and anti-quarks. The values of the masses are taken from [3] with the 2021 update.

with masses again taken from [3] (2021 update). Observe that the three respective quarks constitute only little to the nucleon mass: Most of it is generated dynamically by the interactions of quarks and gluons. The latter will be introduced in the following.

Now we come back to the Lagrangian and enforce that local $SU(3)$ transformations $\Omega(x^\mu)$ generated by the Gell-Mann matrices in color space should leave the Lagrangian

$$\mathcal{L}(\psi, \bar{\psi}, A_a^\mu) \rightarrow \mathcal{L}'(\psi', \bar{\psi}', A_a'^\mu) = \mathcal{L}(\psi, \bar{\psi}, A_a^\mu), \quad (2.13)$$

with new gluonic field A_a^μ , invariant. These new fields result from *minimal substitution* $\partial^\mu \rightarrow D^\mu = \partial^\mu + i g A_a^\mu t_a$, which leads us to the QCD Lagrangian

$$\mathcal{L}_{\text{QCD}} = \underbrace{\bar{\psi}_{fc}(i\gamma_\mu D^\mu - m_q)\psi_{fc}}_{\mathcal{L}_{\text{quarks}}} + \underbrace{-g\bar{\psi}_{fc}\gamma_\mu A_a^\mu t_a\psi_{cf}}_{\mathcal{L}_{\text{interaction}}} + \underbrace{-\frac{1}{4}F_{a\mu\nu}F_a^{\mu\nu}}_{\mathcal{L}_{\text{gluons}}}, \quad (2.14)$$

to which external sources $J = j_f + j_{\text{gluons}}^\mu A_\mu$ can be added. Gluons do not have mass but can be considered to carry two charges: a color and a different anti-color. That is, they are related to octet states of $\mathbf{3} \otimes \bar{\mathbf{3}}$. Let us picture the influence of gluons on quarks in a simplified, schematic way: Assuming that a red quark absorbs an anti-red and blue gluon, color and anti-color neutralize and a blue quark is obtained: Gluons change the color of quarks. If there would be a color neutral gluon, then also color neutral states would feel the full strong interaction, which is not observed. The 8 gluons describe rotations in color space. Their dynamics is governed by $\mathcal{L}_{\text{gluons}}$, which is built by the gluonic field strength tensor

$$F^{\mu\nu} = D^\mu A_a^\nu t_a - D^\nu A_a^\mu t_a = \partial^\mu A_a^\nu t_a - \partial^\nu A_a^\mu t_a + i g A_a^\mu A_b^\nu [t_a, t_b], \quad (2.15)$$

written component wise as

$$F_a^{\mu\nu} = \partial^\mu A_a^\nu - \partial^\nu A_a^\mu - g f_{abc} A_b^\mu A_c^\nu, \quad (2.16)$$

with f_{abc} being the structure constants of $SU(3)$ defined via the commutator

$$[t_a, t_b] = i f_{abc} t_c \quad (2.17)$$

and g the coupling constant.

The Lagrangian of Eq. (2.14) is evaluated via a *path integral*

$$Z(J) := \frac{\langle 0_{-\infty} | 0_{+\infty} \rangle_J}{\langle 0_{-\infty} | 0_{+\infty} \rangle_{J=0}} = \frac{\int e^{-i(\mathcal{L}_{\text{QCD}}+J)} DA D\psi D\bar{\psi}}{\int e^{-i(\mathcal{L}_{\text{QCD}})} DA D\psi D\bar{\psi}}, \quad (2.18)$$

the vacuum-to-vacuum transition amplitude under influence of the external sources J . This formalism will be discussed in more detail in section 2.3. We have neglected $\mathcal{L}_{\text{ghost}}$ and $\mathcal{L}_{\text{gauge}}$ that are usually inserted to cope with gauge fixings.

The non-vanishing commutator in Eq. (2.17) allows the various gluonic interactions and the complexity of QCD with a non-trivial vacuum and confinement, which we explain by center vortices.

The $\mathcal{L}_{\text{quarks}}$ describes the propagation of non-interacting quarks and $\mathcal{L}_{\text{interaction}}$ allows scattering process of quarks and gluons. The invariance of the Lagrangian enforces the gluonic field to transform as

$$A_a^\mu t_a \rightarrow \Omega A_a^\mu t_a \Omega^\dagger + i(\partial_\mu \Omega) \Omega^\dagger. \quad (2.19)$$

Specific gauges can make calculations of different observables easy or complicated. Keep in mind, that only such observables are considered physical, that are gauge invariant.

That the color charge introduced by the SU(3) invariance is not observed is dubbed *color confinement*. Only such hadrons can be observed, that are built from a color neutral set of particles: three colors (Baryons), three anti-colors (anti Baryons), a color anti-color pair (Mesons) or more complicated combinations of them. The meson structure is depicted in Fig. 2.4. By combining three quarks, that is $\mathbf{3} \otimes \mathbf{3} \otimes \mathbf{3}$, nucleons and many more particles can be built. Nucleons can exchange mesons, which makes them prone to a residual part of the strong force. Hence, mesons can be considered as the force carrier of this nuclear force that ensures the stability of nuclear cores. Due to the finite half life of mesons, this nuclear force has a finite range: the mesons disintegrate before having an effect on nucleons at farther distance. The masses and half life of the lightest Mesons, the pions, are given in Table 2.2. The pion mass will be later related to the string tension, the linear rise of the quark anti-quark potential that causes confinement. Mesons as well as Baryons consist of confined quarks that are strongly bound by gluons, the carrier of the strong force. They prevent that any color-neutral combination of particles can be split apart into single colored particles. This confining property of the strong interaction can be understood within the center vortex model that will be presented step by step later. The relation to the dynamics of the gluonic fields will be discussed now.

The Lagrangian can be split into two parts $\mathcal{L}_{\text{QCD}} = \mathcal{L}_{\text{Gauss}} + \mathcal{L}_{-\text{Gauss}}$, with

$$\mathcal{L}_{\text{Gauss}} = \underbrace{\bar{\psi}(i\gamma^\mu \partial_\mu - m)\psi}_{\text{quark}} - \underbrace{\frac{1}{4}(\partial_\mu A_\nu - \partial_\nu A_\mu)(\partial_\mu A_\nu - \partial_\nu A_\mu)}_{\text{gluon}} - \underbrace{\frac{1}{2\lambda}(\partial_\mu A_a^\mu)^2}_{\mathcal{L}_{\text{gauge}}}, \quad (2.20)$$



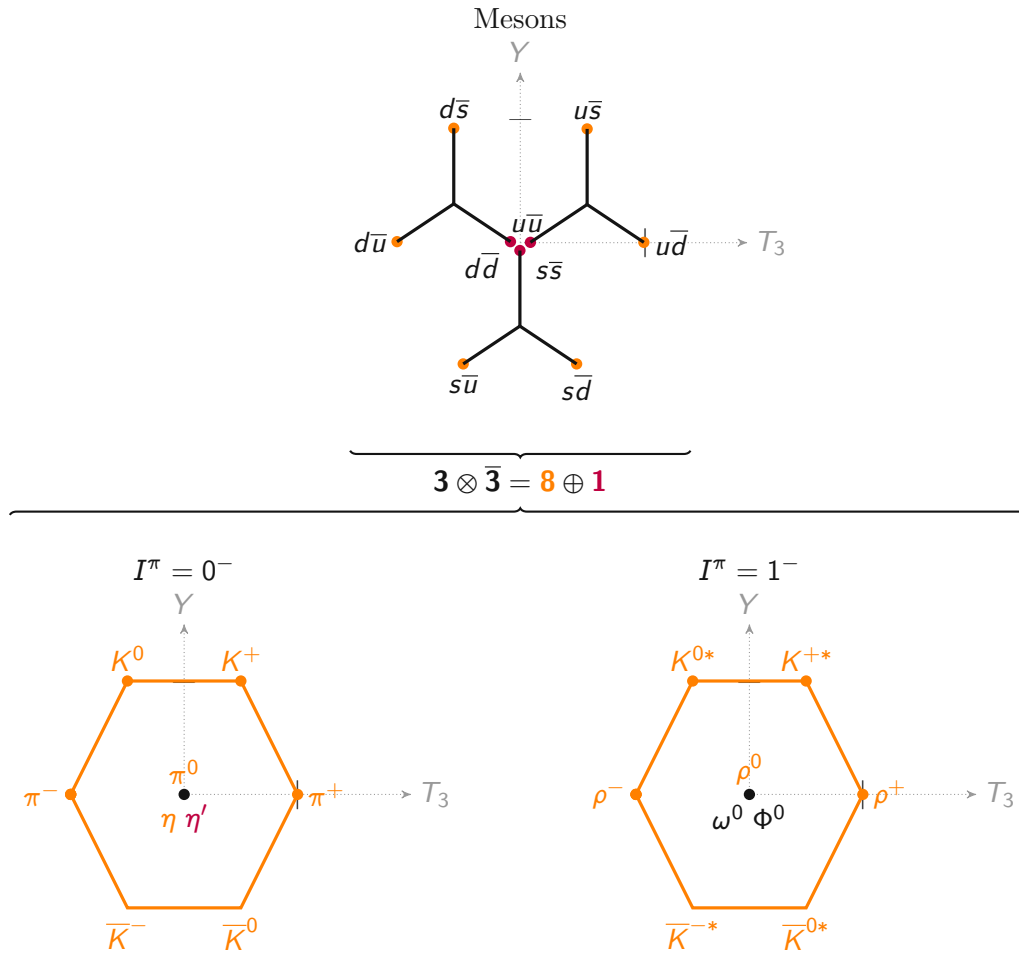


Figure 2.4: Quark anti-quark pairs as depicted in the upper part give rise to the **octet** and **singlet states** shown below. The multiplets are highlighted by color, mixed states are drawn in black color. The spins of the two particles can be parallel or anti-parallel, resulting in a total spin I^π of 0^- for *scalar mesons* and 1^- for *vector mesons*.

collecting all terms that result in a Gaussian integral in the path integral formalism when Fourier transformed. Here we have inserted a term $\mathcal{L}_{\text{gauge}}$ fixing the gauge. The respective terms define the free propagation of quarks and gluons. All terms that do not give rise to a Gaussian integral are collected in

$$\mathcal{L}_{\text{-Gauss}} = \underbrace{-g\bar{\psi}\gamma_\mu t_a \psi A_a^\mu}_{\text{quark-gluon vertex}} - \underbrace{gf_{abc}(\partial_\nu A_{a\mu})A_b^\mu A_c^\nu}_{\text{gluon-gluon vertex}} - \underbrace{\frac{g^2}{4}f_{abc}A_{a\mu}A_{b\nu}f_{cde}A_c^\mu A_d^\nu}_{\text{gluon-gluon-gluon vertex}} \quad (2.21)$$

Scalar Mesons	π^\pm	π^0
Isospin T_3	± 1	0
Hypercharge Y	0	0
Electric charge Q [e]	± 1	0
Mass m [MeV]	139.57039(1)	134.9768(5)
$\frac{1}{2}$ -live time τ [s]	$2.6033(5) * 10^{-8}$	$8.43(13) * 10^{-17}$

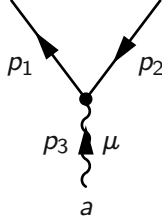
Table 2.2: Mass and half life of the pions are taken from [3] with the 2021 update, Isospin, Hypercharge and Charge are derived group theoretical.

and have to be evaluated numerical. Faddeev–Popov ghosts are neglected here. They are usually required to prevent wrong weighted gauge orbits. We can neglect them since we will later aim for a solely gluonic SU(2) model in which they do not take part. Feynman diagrams for the interaction terms are shown in Eq.(2.21). Each vertex, \bullet , corresponds to a coordinate x^μ at which one of the field variables, $\psi(x^\mu)$, $\bar{\psi}(x^\mu)$ or $A_a^\mu(x^\mu)$, is evaluated. A straight line, \leftarrow , corresponds to the propagation of a quark in direction of the arrow or an anti-quark against direction of the arrow and a wiggled line, \sim , to the propagation of gluons. Feynman diagrams that are build from these objects are interpreted by fixing a direction of time. In dependence of this choice of time direction, different interpretations arise. The 3-Gluonvertex and the 4-Gluonvertex are caused by the non-vanishing commutator of the gluon fields. Let us discuss the diagrams in short.

- The first term can be interpreted either as
 - the absorption or emission of a gluon by a quark,
 - the annihilation of a quark anti-quark pair with the creation of a gluon or
 - the disintegration of a gluon into a quark anti-quark pair,
- the second term correspondingly as
 - the absorption or emission of a gluon by a gluon,
 - the fusion of two gluons or
 - the disintegration of a gluon into two gluons,
- the last term describes
 - gluon gluon scattering processes,
 - the emission or absorption of a gluon pair by a gluon.

At each vertex where two or more lines meet, (relativistic) momentum conservation has to be respected. The total Lagrangian gives rise to an infinite sum of arbitrary nestings of

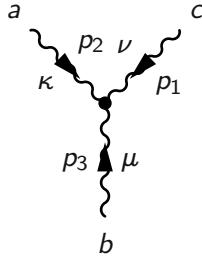
the shown diagrams via the series expansion of the exponential function used to calculate the path integral. After a Fourier transformation, the integration in the path integral of Eq. (2.18) runs over the momenta p^μ instead of x^μ and the following algebraic expressions for the vertices can be derived with arrows indicating the sign of the momentum p :



$$\hat{=} \int d p_1 d p_2 d p_3 (2\pi)^4 \delta^4(p_1 - p_2 - p_3) \quad (2.22)$$

$$(-i g) \bar{\psi}(p_1) t_a \psi(p_2) A_a^\mu(p_3),$$

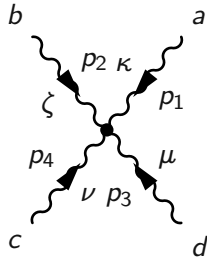
which can be achieved trivially from the first term. The expression resulting from the second term is given by



$$\hat{=} \int d p_1 d p_2 d p_3 (2\pi)^4 \delta^4(p_1 + p_2 + p_3) \quad (2.23)$$

$$(-g) f_{abc} \eta_{\kappa\mu} p_{1\nu} A_a^\kappa(p_1) A_b^\mu(p_3) A_c^\nu(p_2).$$

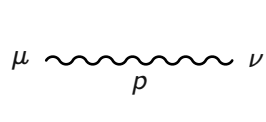
The contraction of the Minkowski indices is explicitly shown in this and the next equation.



$$\hat{=} \int d p_1 d p_2 d p_3 (2\pi)^4 \delta^4(p_1 + p_2 + p_3 + p_4) \quad (2.24)$$

$$\left(-\frac{i g^2}{4}\right) A_a^\kappa(p_1) A_b^\zeta(p_2) A_c^\nu(p_3) A_d^\mu(p_4) f_{abc} f_{cde} \eta_{\kappa\mu} \eta_{\zeta\nu}.$$

The arrows of the gluonic lines are allowed to change direction at vertices. Each propagation contributes



$$\hat{=} \int d p \frac{-i}{(2\pi)^4} \underbrace{\frac{1}{p^\kappa p_\kappa + i\epsilon} (\eta^{\mu\nu} - (1-\lambda) \frac{p^\mu p^\nu}{p_\kappa p^\kappa})}_{D_{aa}^{\mu\nu}(p)}, \quad (2.25)$$

$$\begin{array}{c} \longleftarrow \\ \hline p \end{array} \hat{=} \int d^4p \frac{i}{(2\pi)^4} \underbrace{\frac{p_\mu \gamma^\mu + m}{p^\nu p_\nu - m^2 + i\epsilon}}_{S(p)} \quad (2.26)$$

with $i\epsilon$ inserted to bypass the poles within the integral. Single vertices with only one line entering, so called *legs*, contribute a factor $\int d^4p e^{-i p x}$.

As long as a nesting of such diagrams does not contain loops, the corresponding integral of the resulting diagram converges, but within loops the momenta can become arbitrarily large and cause diverging integrals. Coping with this is called *regularization* and there are many different approaches to do so: the lattice is one of them. We will restrain from an in detail explanation besides the lattice and just introduce some intuitive concepts that help to understand the *running coupling* and the *asymptotic freedom* of quantum chromodynamics. This is required to understand the scaling behaviour of lattice simulations, that is, to determine the lattice spacing.

The central idea is to approximate the series expansion of the exponential by taking only specific diagrams into account and to reformulate the theory in terms of loop-approximations. One possibility is to reformulate the theory in terms of *dressed* propagators and vertices. In one-loop approximation the dressed quark propagator

$$\begin{array}{c} \longleftarrow \\ \hline \end{array} := \begin{array}{c} \longleftarrow \\ \hline \end{array} + \begin{array}{c} \longleftarrow \\ \hline \end{array} \text{---} \text{---} \text{---} \begin{array}{c} \longleftarrow \\ \hline \end{array} \quad (2.27)$$

averages all quark propagations that do not contain nested loops. The gluonic vertices give rise to dressed gluon propagators,

$$\text{---} := \text{---} + \text{---} \text{---} \text{---} + \text{---} \text{---} \text{---} \quad (2.28)$$

If one manages to rewrite or approximate these diagrams as a geometric series with Σ_ψ and Σ_A being finite quark and gluon self energy respective,

$$\begin{array}{c} \longleftarrow \\ \hline \end{array} = \begin{array}{c} \longleftarrow \\ \hline \end{array} + \begin{array}{c} \longleftarrow \\ \hline \end{array} \text{---} \text{---} \begin{array}{c} \longleftarrow \\ \hline \end{array} + \begin{array}{c} \longleftarrow \\ \hline \end{array} \text{---} \text{---} \text{---} \begin{array}{c} \longleftarrow \\ \hline \end{array} + \dots = \begin{array}{c} \longleftarrow \\ \hline \end{array} * \frac{1}{1 - \text{---} \text{---} \begin{array}{c} \longleftarrow \\ \hline \end{array}}, \quad (2.29)$$

$$\text{---} = \text{---} + \text{---} \text{---} \text{---} + \text{---} \text{---} \text{---} \text{---} \text{---} + \dots = \text{---} * \frac{1}{1 - \text{---} \text{---} \text{---}}, \quad (2.30)$$

a dressed theory can be generated from the original formulation with modified propagators. In this dressed theory we restrict ourselves to loop free diagrams.

Now let us take a look at renormalization

$$A \rightarrow \sqrt{Z_A} * A, \quad \psi \rightarrow \sqrt{Z_\psi} * \psi, \quad m \rightarrow Z_m * m, \quad (2.31)$$

with the multiplicative factors Z_A , Z_ψ and Z_m . We will neglect from now on also the gauge fixing term $\mathcal{L}_{\text{gauge}}$ and the corresponding factor λ because on the lattice the gauge fixing is handled differently. One finds that the Lagrangian can only be invariant under renormalization,

$$\mathcal{L}(A, \psi, m, g) \rightarrow \mathcal{L}'(\sqrt{Z_A} * A, \sqrt{Z_\psi} * \psi, Z_m * m, g') = \mathcal{L}(\sqrt{Z_A} * A, \sqrt{Z_\psi} * \psi, Z_m * m, g') \quad (2.32)$$

if also the coupling "constant" g is changed: $g \rightarrow g'$. Let us write the collection of valid renormalization parameters as $\mathcal{M} = \{Z_A, Z_\psi, Z_m, Z_g\}$ and define the dressed vertex functions via

$$V_{\bar{\psi}A\psi} \hat{=} \text{diagram} \approx \text{diagram}_1 + \text{diagram}_2 + \text{diagram}_3, \quad (2.33)$$

$$V_{AAA} \hat{=} \text{diagram} \approx \text{diagram}_1 + \text{diagram}_2 + \text{diagram}_3 + \text{diagram}_4, \quad (2.34)$$

$$V_{AAAA} \hat{=} \text{diagram} \approx \text{diagram}_1 + \text{diagram}_2 + \text{diagram}_3 + \text{diagram}_4 + \text{diagram}_5, \quad (2.35)$$

Then the invariance can be written as

$$\frac{dV_i}{d\mathcal{M}} \stackrel{!}{=} 0 \quad \text{with } i \in \{\bar{\psi}A\psi, AAA, AAAAA\}, \quad (2.36)$$

which expresses that the different renormalized interactions should give rise to the same physical behaviour of the system. This allows to determine $g(\mathcal{M})$ and $m(\mathcal{M})$, the renormalization dependent couplings. The vertex functions are homogeneous in the momenta, that is

$$V_i(\zeta * p_1, \zeta * p_2, \dots, \zeta * p_n, \zeta * g, \zeta * m_i, \zeta * \mathcal{M}) = \zeta^{d_i} * V_i(p_1, p_2, \dots, p_n, g, m_i, \mathcal{M}), \quad (2.37)$$

with d_i being a vertex-specific constant. This allows to relate \mathcal{M} to a momentum scaling ζ . Remember that diagrams with closed loops diverged due to the momenta becoming arbitrarily large and that the lattice introduces a cutoff to the momenta. We can write Eq. (2.36) now with an explicit derivative of the momentum scaling instead of the explicit derivative on \mathcal{M} as

$$0 \stackrel{!}{=} \left(-\zeta \frac{\partial}{\partial \zeta} + \underbrace{\mathcal{M} \frac{dg}{d\mathcal{M}}}_{:=g(\mathcal{M}) * \beta(\mathcal{M})} \frac{\partial}{\partial g} + \left(\underbrace{\mathcal{M} \frac{dm_i}{d\mathcal{M}}}_{:=m_i(\mathcal{M}) * \gamma_f(\mathcal{M})} - 1 \right) \frac{\partial}{\partial m_i} \right) V_i(\zeta p, \zeta p_n, g, \zeta \mathcal{M}), \quad (2.38)$$

a variant of the *Callan-Symanzik equation*. The γ_f -function is not to be mistaken with the Dirac matrices and the β -function should not be mistaken with the inverse coupling to be introduced later. With the substitution $\zeta = e^t$ we obtain

$$\begin{aligned} \frac{dg(t)}{dt} &= g(t) * \beta(g(t), m(t)), \\ \frac{dm_i(t)}{dt} &= m(t) * \gamma_i(g(t), m(t)). \end{aligned} \quad (2.39)$$

For a SU(N) with n_f massless quarks one obtains

$$\begin{aligned} \beta(g) &= -\beta_0 g^3 - \beta_1 g^5 + \mathcal{O}(g^5), \text{ with} \\ \beta_0 &= \frac{1}{(4\pi)^2} \left(\frac{11}{3} N - \frac{2}{3} n_f \right) \underset{n_f=0}{SU(2)} \frac{11}{24\pi^2}, \\ \beta_1 &= \frac{1}{(4\pi)^4} \left(\frac{34}{3} N^2 - \frac{10}{3} N n_f - \frac{N^2 - 1}{N} n_f \right) \underset{n_f=0}{SU(2)} \frac{17}{96\pi^4}, \end{aligned} \quad (2.40)$$

see [4]. This leads to the asymptotic freedom of quantum chromodynamics,

$$t \rightarrow \infty \xrightarrow{\zeta=e^t} \zeta \rightarrow \infty \xrightarrow{\frac{k\alpha\zeta}{(2.37)}} k \rightarrow \infty \xrightarrow{(2.39)} g \rightarrow 0. \quad (2.41)$$

For large momenta p , the coupling g vanishes and we end up with free quarks. We will later relate the momentum scaling ζ to the lattice spacing.

Before we continue our way onto the lattice by discretizing the Lagrangian given in Eq. (2.14), a Wick rotation

$$\begin{aligned} x^0 &\rightarrow i x^0, & \partial_0 &\rightarrow -i \partial_0, & A^0 &\rightarrow -i A^0 \\ F_{00} &\rightarrow -F_{00}, & F_{0i} &\rightarrow -i F_{0i} \end{aligned} \quad (2.42)$$

is performed to end up with an euclidean lattice instead of a minkowskian. With this we work in imaginary time but do no longer need to distinguish upper and lower indices. The gamma matrices we use for the euclidean formulation read

$$\gamma_0 = \begin{pmatrix} \mathbb{0}_2 & \mathbb{1}_2 \\ \mathbb{1}_2 & \mathbb{0}_2 \end{pmatrix} \quad \text{and} \quad \gamma_{k \in \{1, 2, 3\}} = \begin{pmatrix} \mathbb{0}_2 & -i \sigma_k \\ i \sigma_k & \mathbb{0}_2 \end{pmatrix}, \quad (2.43)$$

with Pauli matrices σ_k . This leads us to our final Lagrangians

$$\mathcal{L}_{\text{quarks}}^{\text{euclidean}} = \bar{\psi}_{fc} (\gamma_\mu \partial_\mu + m_f) \psi_{fc} \quad (2.44)$$

and

$$\mathcal{L}_{\text{interaction}}^{\text{euclidean}} = i g \bar{\psi}_{fc} \gamma_\mu A_{\mu, c} t_c \psi_{fc} \quad (2.45)$$

and

$$\mathcal{L}_{\text{gluons}}^{\text{euclidean}} = \frac{1}{4} F_{\mu\nu, a} F_{\mu\nu, a}. \quad (2.46)$$

These Lagrangians need now to be formulated in a discrete version, preserving the gauge invariance. This will allow to continue with the lattice formalism. Before it will be done, we take a look at chiral symmetry or - to be more correct - chiral symmetry breaking, which is not only related to the nucleon mass, but also to center vortices.

We take a closer look at the Lagrangian of a relativistic particle

$$\bar{\psi} \gamma_\mu \partial^\mu \psi + \bar{\psi} m \psi = \psi^\dagger \underbrace{\gamma_0 \gamma_\mu}_{\text{block-diagonal}} \partial^\mu \psi + \psi^\dagger \underbrace{\gamma_0 m}_{\text{block-off-diagonal}} \psi. \quad (2.47)$$

Explicitly written, we have in Weyl representation

$$\begin{aligned} \gamma_0 \gamma_0 &= \begin{pmatrix} 1 & 0 & 0 & 0 \\ 0 & 1 & 0 & 0 \\ 0 & 0 & 1 & 0 \\ 0 & 0 & 0 & 1 \end{pmatrix}, & \gamma_0 \gamma_1 &= \begin{pmatrix} 0 & i & 0 & 0 \\ i & 0 & 0 & 0 \\ 0 & 0 & 0 & -i \\ 0 & 0 & -i & 0 \end{pmatrix}, \\ \gamma_0 \gamma_2 &= \begin{pmatrix} 0 & 1 & 0 & 0 \\ -1 & 0 & 0 & 0 \\ 0 & 0 & 0 & -1 \\ 0 & 0 & 1 & 0 \end{pmatrix}, & \gamma_0 \gamma_3 &= \begin{pmatrix} i & 0 & 0 & 0 \\ 0 & -i & 0 & 0 \\ 0 & 0 & -i & 0 \\ 0 & 0 & 0 & i \end{pmatrix}. \end{aligned} \quad (2.48)$$

Only the **mass term** results in off-diagonal elements and causes a mixing of the two blocks shown in **green** and **red** color.

$$\gamma_0 m = \begin{pmatrix} 0 & 0 & m & 0 \\ 0 & 0 & 0 & m \\ m & 0 & 0 & 0 \\ 0 & m & 0 & 0 \end{pmatrix}. \quad (2.49)$$

We can construct another matrix

$$\gamma_5 = \gamma_0 \gamma_1 \gamma_2 \gamma_3 = \begin{pmatrix} -\mathbb{1}_2 & \mathbb{0}_2 \\ \mathbb{0}_2 & +\mathbb{1}_2 \end{pmatrix} = \underbrace{\begin{pmatrix} -\mathbb{1}_2 & \mathbb{0}_2 \\ \mathbb{0}_2 & \mathbb{0}_2 \end{pmatrix}}_{-P_L} + \underbrace{\begin{pmatrix} \mathbb{0}_2 & \mathbb{0}_2 \\ \mathbb{0}_2 & +\mathbb{1}_2 \end{pmatrix}}_{P_R} \quad (2.50)$$

and use it to decompose the spinor into two components

$$\psi = \underbrace{P_L \psi}_{\psi_L} + \underbrace{P_R \psi}_{\psi_R}. \quad (2.51)$$

Without the mass term, ψ_L and ψ_R would be isolated from one another and the Lagrangian would enjoy *chiral invariance*: transformations that do only rotate within the two chiralities but not between them, would have no influence. This invariance is explicitly broken by the mass term $m\bar{\psi}\psi$, but can also be spontaneously broken by the gluons that dynamically contribute to a non-vanishing chiral condensate $\langle \bar{\psi}_L \psi_R \rangle$: in sufficiently smooth gluonic fields [5] this condensate can be related via the Banks-Casher relation [6] to the spectral density of the euclidean massless Dirac operator and via the Atiyah–Singer index theorem [7] to topological charge. This charge in turn can be related to writhing-points, intersections and the color structure of center vortices. A good review of the most important aspects is given in [8].

With this first motivation of center vortices, we will now find our way onto the lattice.

2.1 Approaching the lattice

The lattice is spanned by a four dimensional vector space with lattice sites $\vec{n} \in \mathbb{N}^4$ on which the spinors $\psi(\vec{n})$ and $\bar{\psi}(\vec{n})$ are encoded. Neighbouring sites are separated by a vector \vec{a}_μ in respective direction μ . The lattice spacing a is given by the length of this vector. Neighbouring lattice sites are joined by a link $U_\mu(\vec{n}) \in SU(3)$ that connects the site \vec{n} to the neighbouring site $\vec{n} + \vec{a}_\mu$. The backwards direction is given by $U_\mu^\dagger(\vec{n})$. These links encode the gluonic field. In Fig. 2.5 a schematic view of a three dimensional lattice is shown, the fourth dimension that correspond to time could not be displayed without loss of clarity. A lattice on which all relevant variables (links and sites) are initialized with a value is referred to as a *configuration*. The lattice comes with periodic boundary

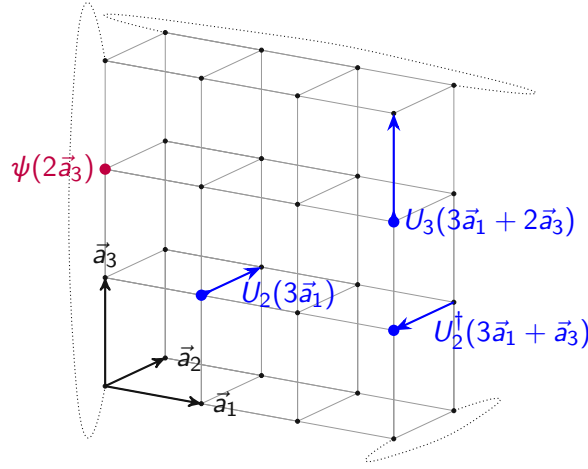


Figure 2.5: A lattice of size $4^2 \times 2$ is shown. The periodic boundary conditions are visualised as dotted lines. The gluonic field is related to the links with some examples shown in blue. The fermionic spinor sits at the lattice sites, an example is shown in purple.

conditions and its extents should be even numbers of lattice sites. The gluonic link is related to the continuum via

$$U_\nu(\vec{x}) = P e^{i \int_{\vec{x}}^{\vec{x}+\vec{a}_\nu} t_i A_i^\nu(x^\mu) dx_\mu} \approx e^{i a t_i A_i^\nu(x^\mu)}, \quad (2.52)$$

with P denoting path ordering, lattice spacing a and \vec{x} being the lattice site that corresponds to the respective x^μ .

Especially in non-abelian gauge fields, only such objects can be compared to one another, that are related to the same spacetime coordinate via parallel transport. The value of given Observable $\hat{O}(\vec{x})$ measured at position \vec{x} can be transported to a position $\vec{x} + \vec{a}_\mu$ using the gluonic link: $U_\mu(\vec{x})\hat{O}(\vec{x})$. Doing a parallel transport in negative direction, the correct link has to be chosen: $U_\mu^\dagger(\vec{x} - \vec{a}_\mu)\hat{O}(\vec{x})$. The links obey the following equations

$$U_{-\mu}(\vec{x}) = U_\mu^\dagger(\vec{x} - \vec{a}_\mu) \quad \text{and} \quad U_\mu(\vec{x})U_{-\mu}(\vec{x}) = 1. \quad (2.53)$$

We will now take a very rough look at the discretization of the fermionic parts of the Lagrangian as given in Equations (2.44) and (2.45). This should only pave the way for a discretization of the gluonic parts that are given in Eq. (2.46). In the following the flavor and color indices are suppressed: Instead of $t_i A_i^\mu$ we write A^μ .

The parallel transport allows to discretize the euclidean Lagrangian for quarks of Eq. (2.44) whilst keeping the gauge invariance and one obtains the *naive fermionic action*

$$S_{\text{quarks}} = a^4 \sum_{\vec{x}, \mu} \bar{\psi}(\vec{x}) \gamma_\mu \left(\frac{U_\mu(\vec{x})\psi(\vec{x} + \vec{e}_\mu) - U_\mu^\dagger(\vec{x} - \vec{a}_\mu)\psi(\vec{x} - \vec{e}_\mu)}{2a} + m\psi(\vec{x}) \right). \quad (2.54)$$

The two evaluations of ψ at different lattice sites originate from the discretization of the derivative. We use the gluonic links to relate both to the lattice site between the sites of the two spinors. A possible discretization of the Lagrangian of Eq. 2.45 is given by

$$S_{\text{interaction}} = i a^4 \sum_{\vec{x}, \mu} \bar{\psi}(\vec{x}) \gamma_\mu \frac{1}{2} (A_\mu(\vec{x}) \psi(\vec{x}) + A_\mu(\vec{x} - \vec{a}_\mu) \psi(\vec{x} - \vec{a}_\mu)), \quad (2.55)$$

with

$$U_\mu \approx \mathbb{1} + i a A_\mu \quad \text{and} \quad U_\mu^\dagger \approx \mathbb{1} - i a A_\mu \quad (2.56)$$

following from Eq. (2.52).

Before we can discuss a discretization of the gluonic Lagrangian, we need to take a look at gauge independent operators. They will be used to construct the gluonic action so that in the continuum limit $a \rightarrow 0$ it becomes identical with the gluonic action of the continuum as given in Eq. (2.46).

The transformation properties of the links are given by

$$U_\mu(\vec{x}) \rightarrow \Omega(\vec{x}) U_\mu(\vec{x}) \Omega^\dagger(\vec{x} + \vec{a}_\mu) \quad (2.57)$$

and the spinors transform as

$$\psi(\vec{x}) \rightarrow \Omega(\vec{x}) \psi(\vec{x}) \quad \text{and} \quad \bar{\psi}(\vec{x}) \rightarrow \bar{\psi}(\vec{x}) \Omega^\dagger(\vec{x}). \quad (2.58)$$

The Matrices $\Omega(\vec{x})$ can be set to accomplish specific gauges. In *temporal gauge* on non-periodic lattices for example, all temporal links can be set to unity $U_0(\vec{x}) = \mathbb{1}$, which corresponds to $A_0(x^\mu) = 0$. On a periodic lattice this gauge can be achieved only up to a single time slice. This gauge will be used in Section 2.4 to allow a better understanding of the Wilson loop that is presented in the following.

Based on the transformation properties two different gauge independent operators can be constructed:

- Particle and anti-particle that are joined via a connected path of links:

$$\bar{\psi}(\vec{x}_1) \overbrace{\Omega^\dagger(\vec{x}_1) \Omega(\vec{x}_1)}^1 U_\mu(\vec{x}_1) \Omega^\dagger(\vec{x}_1 + \vec{a}_\mu) \dots \dots \Omega(\vec{x}_2) U_\nu(\vec{x}_2 + \vec{a}_\nu) \underbrace{\Omega^\dagger(\vec{x}_2 + \vec{a}_\nu) \Omega(\vec{x}_2 + \vec{a}_\nu)}_1 \psi(\vec{x}_2 + \vec{a}_\nu), \quad (2.59)$$

- The trace of closed paths of connected links, a *Wilson loop*:

$$\text{Tr}(\overbrace{\Omega^\dagger(\vec{x}) \Omega(\vec{x})}^1 U_\mu(\vec{x}) \overbrace{\Omega^\dagger(\vec{x} + \vec{a}_\mu) \Omega(\vec{x} + \vec{a}_\mu)}^1 U_\nu(\vec{x} + \vec{a}_\mu) \overbrace{\Omega^\dagger(\vec{x} + \vec{a}_\mu + \vec{a}_\nu) \dots}^1 \dots \underbrace{\Omega(\vec{x} + \vec{a}_\mu + \vec{a}_\nu) U_{-\nu}(\vec{x} + \vec{a}_\mu + \vec{a}_\nu)}_1 \underbrace{\Omega^\dagger(\vec{x} + \vec{a}_\mu) \Omega(\vec{x} + \vec{a}_\mu)}_1 U_{-\mu}(\vec{x} + \vec{a}_\mu)). \quad (2.60)$$

In the continuum such Wilson loop W_C corresponds to a closed curve integral along the path C

$$W_C = \text{Tr} \left(P e^{i \oint_C A^\mu dx_\mu} \right). \quad (2.61)$$

If a loop is closed by the lattice periodicity, we speak of a *Polyakov loop*, see Fig. 2.6 where some examples are shown. The smallest possible Wilson loops built by four links

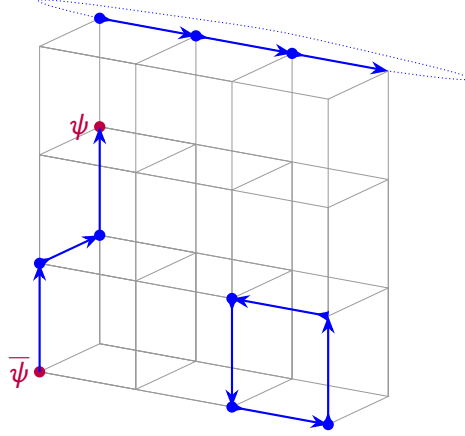


Figure 2.6: A lattice of size $4^2 \times 2$ is shown with some examples for gauge invariant operators: On the upper side, a Polyakov loop P_μ is shown. On the left side a anti-particle is joined with a particle via links. On the lower right side the smallest possible Wilson loop, a *plaquette* $U_{\mu\nu}$, is shown.

are called *plaquettes*. A plaquette in the $\mu\nu$ -plane at lattice site \vec{n} is written with two indices as $U_{\mu\nu}(\vec{n})$. These are used to formulate a simple gluonic action, the *Wilson action* [9],

$$S_{\text{gluons}} = \beta \sum_{\vec{x}, \mu < \nu} \left(1 - \frac{1}{N} \Re \text{Tr}(U_{\mu\nu}(\vec{x})) \right) \quad (2.62)$$

for an $SU(N)$ with *inverse coupling* $\beta = \frac{2N}{g^2}$ and the trace with respect to the color space. This action is solely real, which allows to solve it via the path integral formalism by relating the action to a probability density. It reproduces the continuum version of the action up to $\mathcal{O}(a^2)$ and the value of the lattice spacing a can be adjusted by setting the value for β . A faster approach to the continuum can be achieved, for example, with the *tree level improved Symanzik gauge action* [10, 11] by taking not only plaquettes but also rectangular loops built by 6 links, $\square\square$, into account. For $SU(2)$ it is given by

$$S_{\text{TreeLevelSymanzik}} = \beta \left(\frac{5}{3} \sum_{\vec{x}, \mu < \nu} \left(1 - \frac{1}{2} \text{Tr}(U_{\mu\nu}(\vec{x})) \right) - \frac{1}{12} \sum_{\square\square} \left(1 - \frac{1}{2} \text{Tr}(\square\square) \right) \right). \quad (2.63)$$

We do not require these improvement in this work and stay with the Wilson action.

For center vortices only the gluonic part is of relevance. In this work, Wilson action with further simplification is used: The SU(3) describes rotations in a 3 dimensional color space. We simplify to SU(2), which is also confining and allows for extensive calculations with better statistics. In contrast to SU(3), the vortex structure is less complicated in SU(2). There is only one non-trivial center element in SU(2), whereas there are two of them in SU(3). The generators t_i of SU(2) simplify to the Pauli matrices $\vec{\sigma}$ and with $\sigma_0 = \mathbb{1}$ the links can be written as

$$U(\vec{x}) = \sum_{i=0}^3 c_i(\vec{x})\sigma_i = \mathbb{1} \cos \alpha(\vec{x}) + i \vec{n}(\vec{x})\vec{\sigma} \sin \alpha(\vec{x}) \quad (2.64)$$

with c indicating an element of \mathbb{S}_3 , α governing the strength and $\vec{n} \in \mathbb{S}_2$ the *color vector* of the gluonic link.

The link can be interpreted as a path on the surface of a four dimensional unit sphere: it starts at the north pole at the trivial center element $+1$ and ends somewhere on the sphere. The non-trivial center element -1 is related to the south pole. This path corresponds to a rotation in \mathbb{C}^2 . Such a path is shown schematically in Fig. 2.7. A Wilson

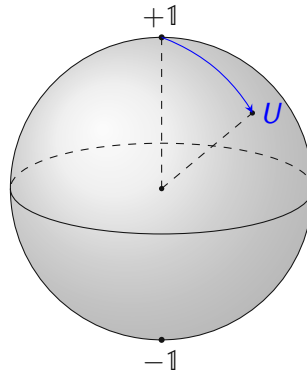


Figure 2.7: The SU(2) link can be interpreted as a path starting at the north pole, $+1$, of a four dimensional unit sphere. The projection on the vertical axes corresponds to the trace operator.

loop is a sequence of links and corresponds to a path starting at $+1$ on this color sphere. The gluonic SU(2) Wilson action favours plaquettes with values near the north pole.

The distance of the paths end point from the vertical axes is related to the flux through the area that is enclosed by the corresponding loop in Minkowski space. The projection of the path on the vertical axes correlates to the action density.

If $c_0 = \cos \alpha$ in Eq. (2.64) is fixed, the remaining degrees of freedom span a two dimensional surface of a sphere with radius $\sin \alpha$. This vanishes for $c_0 = \pm 1$.

The Wilson action prefers plaquettes evaluating in the vicinity of $+1$, it prefers nearly closed paths on the color sphere. We will later see that a plaquette or a bigger Wilson loop pierced by a center vortex, corresponds to a path from $+1$ to -1 on this four

dimensional color sphere. Each such path can be related to a meridian with given color \vec{n} on the sphere. The variation of this color vector along the two dimensional vortex surface defines the color structure of the vortex. This color structure in turn can be related to the chiral properties of the vortex via the Banks-Casher relation [6] and the Atiyah–Singer index theorem [7].

The implementation of the SU(2) Wilson action is shown in Algorithm 2.1 in Pseudocode. In the next section this algorithm is applied to those 6 plaquettes that have one link in

Algorithm 2.1: SU(2) Wilson action

Data: The SU(2) links of the configuration $U_\mu(\vec{x})$: at lattice site \vec{x} , pointing in direction μ . Inverse coupling β .

Result: The Wilson action S_{gluons} for a given configuration

- 1 $S_{\text{gluons}} = 0$;
 - 2 **for** all lattices sites \vec{x} and all direction μ and ν with $0 \leq \mu < \nu$ **do**
 - 3 $S_{\text{gluons}} += \beta * (1 - \frac{1}{2} \text{Tr}(U_\mu(\vec{x}) U_\nu(\vec{x} + \vec{a}_\mu) U_\mu^\dagger(\vec{x} + \vec{a}_\nu) U_\nu^\dagger(\vec{x})));$
 - 4 **end**
-

common to determine the change in action that results from the modified link. In line 3 the plaquette gets calculated by multiplying the four links of the respective plaquette. The relation of links to lattice sites may be confusing for backward links. For clarification the plaquette is schematically shown in Fig. 2.8.

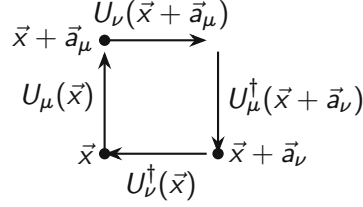


Figure 2.8: A plaquette is constructed from four gluonic links, so that the smallest possible Wilson loop is built. Observe how the links are related to the lattice sites.

Let us now see how this action reproduces the gluonic action in the continuum. The starting point is the Baker–Campbell–Hausdorff formula for the multiplication of two exponentials of non-commutative matrices A and B

$$e^A e^B = e^{A+B+\frac{1}{2}[A,B]+\dots}, \quad (2.65)$$

where orders higher than 2 of the matrices have been absorbed into the three points. Using Eq.(2.52) we write the plaquette as

$$U_{\mu\nu}(\vec{x}) = \text{Tr} \left(\underbrace{e^{i a A_\mu(\vec{x})}}_{U_\mu(\vec{x})} \underbrace{e^{i a A_\nu(\vec{x}+\vec{a}_\mu)}}_{U_\nu(\vec{x}+\vec{a}_\mu)} \underbrace{e^{-i a A_\mu(\vec{x}+\vec{a}_\nu)}}_{U_\mu^\dagger(\vec{x}+\vec{a}_\nu)} \underbrace{e^{-i a A_\nu(\vec{x})}}_{U_\nu^\dagger(\vec{x})} \right) \quad (2.66)$$

and can use the Baker–Campbell–Hausdorff formula up to second order of the matrices

$$\begin{aligned}
 \text{Tr}(U_{\mu\nu}(\vec{x})) &\approx \text{Tr}\left(\exp\left(
 \begin{aligned}
 &i a A_{\mu}(\vec{x}) + i a A_{\nu}(\vec{x} + \vec{a}_{\mu}) - \frac{a^2}{2}[A_{\mu}(\vec{x}), A_{\nu}(\vec{x} + \vec{a}_{\mu})] \\
 &- i a A_{\mu}(\vec{x} + \vec{a}_{\nu}) - i a A_{\nu}(\vec{x}) + \frac{a^2}{2}[A_{\mu}(\vec{x} + \vec{a}_{\nu}), A_{\nu}(\vec{x})] \\
 &+ \frac{a^2}{2}[A_{\nu}(\vec{x} + \vec{a}_{\mu}), A_{\mu}(\vec{x} + \vec{a}_{\nu})] + \frac{a^2}{2}[A_{\mu}(\vec{x}), A_{\nu}(\vec{x})] \\
 &+ \frac{a^2}{2}[A_{\mu}(\vec{x}), A_{\mu}(\vec{x} + \vec{a}_{\nu})] + \frac{a^2}{2}[A_{\nu}(\vec{x} + \vec{a}_{\mu}), A_{\nu}(\vec{x})] + \mathcal{O}(a^3)
 \end{aligned}
 \right)
 \right. \\
 &\left. \right) = \text{Tr}\left(e^{i a^2 F_{\mu\nu}(\vec{x}) + \mathcal{O}(a^3)}\right) \approx \text{Tr}(1) - \frac{a^4}{2} \text{Tr}(F_{\mu\nu} F^{\mu\nu}) + \mathcal{O}(a^2),
 \end{aligned}
 \tag{2.67}$$

where in the second last step we performed a Taylor expansion on the shifted field variables $A_{\mu}(\vec{x} + \vec{a}_{\nu}) \approx A_{\mu}(\vec{x}) + a * \partial_{\nu} A_{\mu}(\vec{x})$, compare Ref. [4]. This relates the Wilson loop to the action density. In the last step we have expanded the exponential and respected that the lowest vanishing contribution to the trace comes from the second order of the field strength tensor.

The lattice formulation naturally introduces a momentum cutoff of the order a^{-1} which regularizes the theory: the lattice constant introduces a lower limit for wavelengths which leads to an upper limit for the momentum. The proportionality of the momentum cutoff to a^{-1} allows to make the momentum scaling ζ of Eq. (2.37) also proportional to a^{-1} ,

$$\zeta = \Lambda^{-1} \frac{1}{a}, \tag{2.68}$$

with Λ being the scale parameter of quantum chromodynamics. We will later use this to determine the physical value of the lattice spacing a for a given inverse coupling β .

Also finite size effects have to be taken into account. They are visualized in Fig. 2.9. The

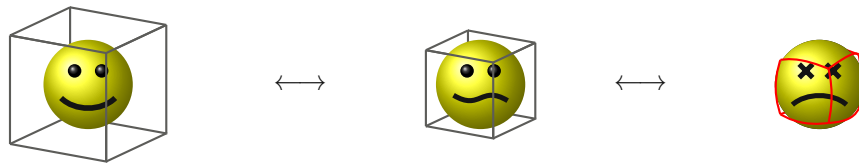


Figure 2.9: If the lattice becomes smaller and smaller, finite size effects set in and distort measurements. This can lead to wrong continuum limits.

lattice has to be big enough for whatever one wants to simulate. This can be accomplished either by ensuring that the lattice spacing is large enough (that is, β small enough) or by keeping the number of lattice sites in each direction large enough. To prevent conflicts with the boundary conditions, the lattice should be kept about twice as large as the object of interest. Finite size effects betray themselves by giving an observable of interest a dependence on the physical lattice extent. To ensure that finite size effects are not

distorting the measurements, at least two different lattice sizes should be probed: if the values measured for different lattice sizes deviate from one another, the data might be flawed. This is shown in Fig. 2.10 for a measurement of the *color-homogeneity* that will be introduced later in section 2.4: With the lattice becoming too small, color-homogeneous

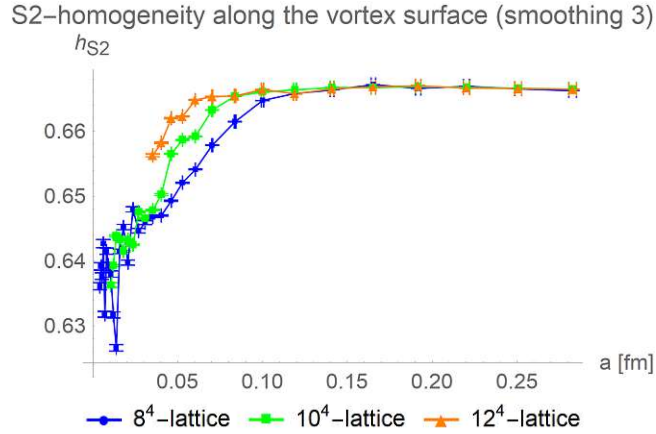


Figure 2.10: Taken from [12], finite size effects concerning measurements of the color homogeneity are shown: they betray themselves by the sudden decrease of h_{S2} with decreasing lattice spacing that occurs at different physical lattice extents.

regions do no longer find place and a sudden decrease of the color homogeneity can be observed. For different lattice sizes this decrease occurs at different values of the lattice spacing a (or β) which is a direct indication for finite size effects.

Despite this negative distortion of measurements due to finite size effects, they can be used to estimate the size of yet unknown structures as we will do in section 4.2 with color homogeneous regions: reducing the lattice size until the onset of finite size effects, the respective lattice extent in physical units gives an estimate or an upper limit for the physical extent of the structure of interest: shrink the lattice until the lion roars to see how fat he is.

Discretization effects are visualized in Fig. 2.11. They occur at low values of β , that is, high values of a . To observe specific structures, the lattice resolution has to be high

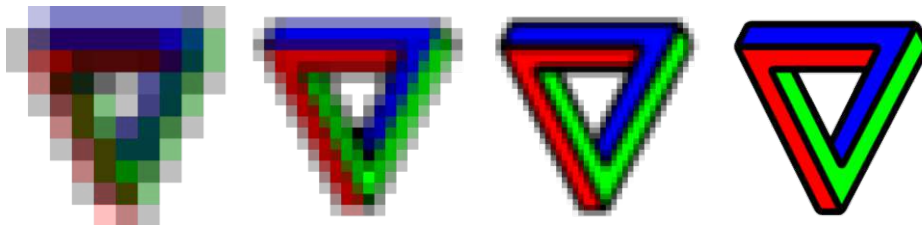


Figure 2.11: The left side corresponds to a large lattice spacing a , towards the right side the lattice resolution is increased. Discretization effects correspond to finite sized pixels due to which a loss of structure occurs.

enough, that is, a has to be small enough. Usually one is interested in the continuum

limit $a \rightarrow 0$. This requires increasing β and numerical extrapolation to infinity. Due to finite size effects, β can not be chosen arbitrarily large: the computational resources limit the calculable lattice size. Hence, there is a *scaling window* of lattice parameters where a correct continuum limit is obtained by extrapolation. Outside this window the extrapolation is flawed by finite size effects and discretization effects.

Simply spoken, each measurement on the lattice is related to collecting statistics on discrete objects: Length is measured by counting links, area is measured by counting plaquettes and so on. These relations of lattice and physical values,

$$l_{\text{physical}} = a l_{\text{lattice}} \quad \text{for lengths} \quad \text{and} \quad m_{\text{physical}} = \frac{m_{\text{lattice}}}{a} \quad \text{for masses}, \quad (2.69)$$

allow to relate a given β to a corresponding value of a by comparison with physical observables $l_{\text{physical}}(a, g(a))$ as will be done in section 2.4. With $a \rightarrow 0$ the observable $l_{\text{lattice}}(a, g(a))$ has to diverge to allow for a finite value of the observable $l_{\text{physical}}(a, g(a))$ in physical units. Based on Eqs.(2.38) and (2.36) we can express this as

$$a \frac{d}{da} l_{\text{physical}}(a, g(a)) = \frac{d}{d(\ln a)} l_{\text{physical}} = \frac{\partial}{\partial(\ln a)} l_{\text{physical}} + \underbrace{\frac{\partial g}{\partial(\ln a)} \frac{\partial}{\partial g}}_{-\beta(g)} l_{\text{physical}} \stackrel{!}{=} 0. \quad (2.70)$$

Together with Eq. (2.39) the lattice spacing a can be related to the coupling constant g and one obtains for $SU(N)$

$$a(\beta) = \frac{1}{\Lambda} \left(\frac{\beta}{2\beta_0 N} \right)^{\frac{\beta_1}{2\beta_0^2}} e^{-\frac{\beta}{4\beta_0 N}} \left(1 + \mathcal{O}\left(\frac{2N}{\beta}\right) \right) \stackrel{*}{\approx} \frac{1}{\Lambda} e^{-\frac{\beta}{4\beta_0 N}}, \quad (2.71)$$

* asymptotic scaling behaviour ($\beta_1 \approx 0$ for $g \rightarrow 0$)

with yet unknown constant Λ that has to be determined by comparison with experimental data and β_i from Eq. (2.40). For a more detailed derivation see [4]. How Λ can be determined will be discussed in section 2.4.

With this our way onto the lattice is nearly finished and we can now introduce the center vortex before quantization via the path integral is discussed in section 2.3.

2.2 From center symmetry to center vortices

We will now introduce and further motivate the concept of *center vortices* starting from the center invariance of the Lagrangian, followed by a short discussion of the relations between center vortices and Wilson loops as well as Polyakov loops.

The *center* $Z(\mathcal{G})$ of a group \mathcal{G} is defined as the set of all its elements commuting with all other group elements

$$Z(\mathcal{G}) = \{z \in \mathcal{G} \mid \forall g \in \mathcal{G} : zg = gz\}. \quad (2.72)$$

For $SU(N)$ it can be represented by the N roots of unity

$$Z(SU(N)) = \{e^{i\vartheta} \mathbb{1}_N \mid \vartheta = \frac{2k\pi}{N}, k = 0, 1, \dots, N-1\}. \quad (2.73)$$

Restricting ourself to $SU(2)$, we deal with $Z_2 = \pm 1_2$.

Lattice Quantum Chromodynamics comes with a global center symmetry: If we multiply all links within the lattice that point in the same direction ν with the same center element z , the evaluation of plaquettes $U_{\mu\nu}$ and arbitrary Wilson loops is unchanged,

$$U_\nu \rightarrow U'_\nu = U_\nu z \Rightarrow U_{\mu\nu} \rightarrow U'_{\mu\nu} = U_\mu \underbrace{U'_\nu}_{U_\nu z} \underbrace{U'_\mu^\dagger}_{z^\dagger U_\mu^\dagger} \underbrace{U'_\nu^\dagger}_{z^\dagger U_\nu^\dagger} = U_\mu U_\nu U_\mu^\dagger U_\nu^\dagger \underbrace{z z^\dagger}_1 = U_{\mu\nu}, \quad (2.74)$$

with the four-dimensional position vectors omitted. Such transformation is called a *center transformation*. The respective invariance is caused by the fact that every loop consists of an even number of transformed links: half of them in forward direction and the other half in backwards direction. An even number of non-trivial center elements multiplies to unity. In contrast to that, a Polyakov loop P_μ is sensitive to a center transformation: it is closed only via the periodicity of the lattice, hence does not consist of pairs of forward and backward links

$$U_\nu \rightarrow U'_\nu = U_\nu z \Rightarrow P_\nu \rightarrow P'_\nu = U'_\nu U'_\nu U'_\nu = P_\nu z. \quad (2.75)$$

This is depicted in Fig. 2.12. Thus, Polyakov loops present an order parameter for

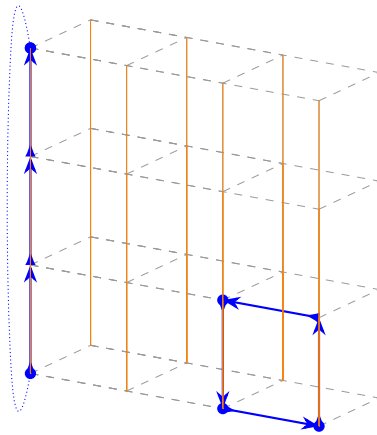


Figure 2.12: Multiplying all links that point in same direction (shown in orange) with a center element does not influence a Wilson loop (shown with blue links in the lower right corner), but a Polyakov loop (shown with blue links on the left side). All trivial links are drawn dashed.

center symmetry and we will later relate them to confinement and vortex percolation: Percolating vortices cause confinement and the transition into deconfinement can be seen as a de-percolation transition of center vortices, that is, a percolating vortex disintegrates into small, non-connected vortex clusters.

A center transformation restricted to a specific volume of the lattice creates such a center vortex: the transformed volume is referred to as the *Dirac volume* and the vortex arises as its surface. This is schematically depicted in Figure 2.13.

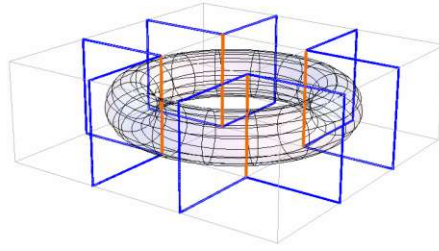


Figure 2.13: A three dimensional slice through a lattice after projection. The links painted in orange evaluate to non-trivial center elements, all other links evaluate to the trivial center element. The plaquettes shown in blue are pierced by the flux building up the vortex (shown as transparent torus). They evaluate to non-trivial center elements. Due to the lattice periodicity the closed flux builds a closed surface in the full four dimensional lattice.

As long as the center vortex surface is closed via the lattice periodicity in all directions, it can be considered as a vortex that percolates through the infinite vacuum.

Starting from a trivial lattice, only the links in vertical direction within the Dirac volume are multiplied with a non-trivial center element. Only such loops evaluate to the non-trivial center that are built by an arbitrary number of trivial links and an odd number of non-trivial links. These are exactly those loops, that touch the Dirac volume once. The smallest possible loops on the lattice, the plaquettes built by exactly four links, have only one possibility to become non-trivial in the aforementioned scenario: if one of their links is part of the Dirac volume. Non-trivial plaquettes are considered pierced by the vortex, hence, the vortex can be seen as given by the surface of the Dirac volume, the *vortex surface*.

In a non-trivial lattice where the links can evaluate to arbitrary group elements, the situation is more complicated: non-trivial center elements can be distributed over many links, which gives rise to a finite thickness of the vortex surface - the flux lines that build the vortex acquire thickness and become flux tubes.

Detecting center vortices is based on reconstructing the Dirac volume. This is related to looking for Wilson loops pierced by a vortex. This is done by projecting the $SU(2)$ links to the center degrees of freedom $U_\mu(\vec{n}) \rightarrow Z_\mu(\vec{n}) = \pm 1$ in a specific gauge. The details will be discussed in chapter 3.

The center vortex model states, that from the center degrees of freedom alone it is possible to reproduce physical observables, especially the string tension, as long as center vortices have been successfully detected. We will now present how exactly observables are evaluated on the lattice using the path integral before the respective observable will be discussed in more detail.

2.3 Implementing the gluonic path integral

Quantization of the Lagrangian of the gluonic dynamics given in Eq. 2.46 is done via the path integral. Within this formalism, the expectation value of a given Operator \hat{O} arises as the weighted average over all possible field configurations

$$\langle \hat{O} \rangle = \frac{\int O[\phi] e^{-S_{\text{gluons}}(\phi)} D\phi}{\int e^{-S_{\text{gluons}}(\phi)} D\phi}, \quad (2.76)$$

with $\phi = \{U_\mu(\vec{n}) \mid \mu \in \{0, 1, 2, 3\} \wedge \vec{n} \text{ a lattice site}\}$ denoting the whole lattice and $O[\phi]$ being an evaluation of the Operator \hat{O} for given ϕ . The higher the action of the configuration, the lower it is weighted within the path integral. The integration measure is given by

$$D\phi = \prod_{\mu\vec{n}} DU_\mu(\vec{n}), \quad \text{so that} \quad \int D\phi = 1. \quad (2.77)$$

The integral runs over all links of the given lattice. It is not analytical solvable and a numerical approach has to be taken: We use a Monte Carlo procedure with a Metropolis algorithm to generate random ensembles.

The general idea is to create an ensemble of lattice configurations by randomly setting the values of all links according to a probability distribution as given by

$$p(\phi) = \frac{e^{-S_{\text{gluons}}(\phi)}}{\int e^{-S_{\text{gluons}}(\phi')} D\phi'}. \quad (2.78)$$

Then one averages the measurement of interest over this ensemble. The configurations of this ensemble can be generated within a Markov chain: Given a valid configuration ϕ , one can generate new valid configurations ϕ' one after another so that the resulting ensemble of configurations fulfills the probability distribution of Eq. 2.78. Such procedure comes with two requirements:

Each possible configuration has to be accessible from each other configuration,

$$p(\phi \rightarrow \phi') > 0 \quad \forall \phi' \quad \text{with} \quad \int p(\phi \rightarrow \phi') d\phi' = 1. \quad (2.79)$$

This property, called strong ergodicity, ensures that the whole phase space can be reached given enough time. Together with a *detailed balance*,

$$\frac{p(\phi \rightarrow \phi')}{p(\phi' \rightarrow \phi)} = \frac{e^{-S_{\text{gluons}}(\phi')}}{e^{-S_{\text{gluons}}(\phi)}}, \quad (2.80)$$

a Boltzmann distribution can be produced via an acceptance probability for a transition $\phi \rightarrow \phi'$ given by

$$p(\phi \rightarrow \phi') = \begin{cases} 1 & \text{if } S_{\text{gluons}}(\phi') < S_{\text{gluons}}(\phi), \\ e^{S_{\text{gluons}}(\phi) - S_{\text{gluons}}(\phi')} & \text{otherwise.} \end{cases} \quad (2.81)$$

This can be implemented using a random number generator $\text{rnd}(0, 1)$ that is restricted to the interval from 0 to 1: only configurations ϕ' are accepted with $p(\phi \rightarrow \phi') \geq \text{rnd}(0, 1)$. Whenever a configuration is rejected, a new configuration ϕ' is tried.

The procedure can be speed up by performing it stepwise on single links instead of performing it on the whole lattice at once. In doing so, the lattice geometry has to be respected by only performing a transition $U_\mu(\vec{n}) \rightarrow U'_\mu(\vec{n})$ on such links not belonging to the same plaquette. On a four dimensional lattice each link is part of 6 plaquettes as is depicted in Fig. 2.14. If of all shown links only the blue one is modified, the influence on

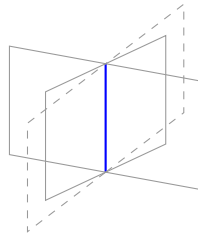


Figure 2.14: The link shown in blue is part of six plaquettes. The plaquettes drawn with dashed lines are located one timestep in positive direction and one timestep in negative direction respective.

the total gluonic action is restricted to the modification of the six plaquettes: No further contributions have to be calculated. Instead of working on the whole lattice at once and always recalculating the total action, one can modify one link after another without the need to recalculate the total action in every step.

When performing the transition from ϕ to ϕ' stepwise, each single link has to have the possibility of getting modified at least once before the new configuration ϕ' is reached. Otherwise the produced ensemble will consist of strongly correlated configurations spoiling the path integral. The number of modification trials per link is dubbed *hits*. If the step-wise procedure was performed on all links, we speak of a *sweep*.

The single modification is done by multiplying the link with a random element of $SU(2)$ spread around unity. Such element can be built from a random three dimensional unit vector according to Eq. 2.64 with a α defining the spread around unity. The naive approach of generating three random numbers between -1 and 1 followed by building a normalized vector results in non-evenly distributed unit vectors. The Box-Muller method allows to generate normal distributed vectors [13]. This method takes two even-distributed random numbers $r_1 = \text{rnd}(0, 1)$ and $r_2 = \text{rnd}(0, 1)$ and produces two normal-distributed random numbers

$$\tilde{c}_1 = \sqrt{-2 \log(r_1)} \cos(2\pi r_2) \quad \text{and} \quad \tilde{c}_2 = \sqrt{-2 \log(r_1)} \sin(2\pi r_2). \quad (2.82)$$

By producing two such random pairs, three of the four normal distributed numbers can be composed into a three dimensional vector. This vector can be normalized to 1 and the random $SU(2)$ element can be built.

Markov chains require several hundred sweeps to reach equilibrium. To allow for a fast and controlled approach towards equilibrium, the spread can be adjusted for a acceptance rate of 50% to 60%. In the pseudocode description of the respective algorithm 2.2, the optimization of the spread is done dynamically in lines 19 to 25 by adjusting the spread in dependence of the number of accepted transitions. A lower spread causes an increased acceptance rate and a higher spread a reduced acceptance rate. In the simulation software used in this work this dynamic optimization is not implemented.

The Monte Carlo approach for solving the path integral requires an ensemble of uncorrelated configurations. Correlated configurations distort the measurements, underestimating the errors. With smaller spread the correlation increases because the modifications from one configuration to the next become small.

For some measurements, especially those that are related to topological charge, sufficiently smooth configurations are required. Of importance is that these smooth configurations have to result in correct continuums limits: They have to correctly reproduce physical observables. One possibility to accomplish smooth configurations is by applying *pisa cooling* [14]. This procedure minimizes the action caused by a single link U by modifying the link to U' under the constraint

$$\delta^2 \geq \frac{1}{2} \text{Tr} \left((U^\dagger - U'^\dagger) (U - U') \right) = 2 - \text{Tr} (U^\dagger U') \quad (2.83)$$

whilst holding all other links fixed. The constraint corresponds to an upper limit of the action of a loop build by the original and the modified link. This is schematically depicted in Fig. 2.15. The modified link is constrained to the vicinity of the original link, that is, only small deviations are allowed.

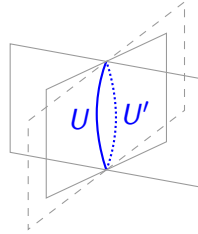


Figure 2.15: Pisa cooling reduces the action by iteratively modifying the single links under the constraint, that the action of a closed loop built by the original link (drawn as solid blue line) and the modified link (drawn as dotted blue line) is limited.

The parameter δ is referred to as *cooling strength*. The procedure is executed iteratively on all links. The number of cooling steps gives the number of full sweeps over all links. The cooling strength as well as the number of cooling steps can not be arbitrarily large without distorting the continuums limit.

A possible alternative is given in the usage of *fat links* [15] instead of the usual links when calculating observables of interest. A fat link $\mathbf{U}_\mu(\vec{x})$ from \vec{x} to $\vec{x} + \vec{a}_\mu$ is calculated

Algorithm 2.2: Markov Chain of configurations according to the path integral**Data:**

- The SU(2) links of the configuration, $U_\mu(\vec{x})$: at lattice site \vec{x} , pointing in direction μ . Either all initialized to $\mathbb{1}$, to a random SU(2) element or taken from a previous step of the Markov chain.
- the number of hits to be performed
- the number of sweeps to be performed

Result: A new configuration according to the path integral

```

1 double spread = 1;
2 for  $i=1$  to sweeps do
3   for all  $\vec{x}$  and  $\mu$  do
4     int accepted = 0;
5     for  $h=1$  to hits do
6       double  $\theta = \frac{\pi}{2} * \text{spread} * \text{rnd}()$ ,  $\vec{n}$  = random 3-d unit vector;
7       matrix  $\Omega = \cos(\theta) * \mathbb{1} + i * \sin(\theta) * \sum_{i=1}^3 n_i * \sigma_i$ ;
8        $U'_\mu(\vec{x}) = \Omega U_\mu(\vec{x})$ ;
9        $S$  = Action of the 8 plaquettes that share the link  $U_\mu(\vec{x})$ ;
10       $S'$  = Action of the 8 plaquettes that share the link  $U'_\mu(\vec{x})$ ;
11       $p = 1$ ;
12      if  $S' \geq S$  then
13        |  $p = e^{S-S'}$ ;
14      end
15      if  $\text{rnd}() < p$  then
16        |  $U_\mu(\vec{x}) = U'_\mu(\vec{x})$ ; accepted++; // accept modified link
17      end
18    end
19    if  $\text{accepted} < 0.5 * \text{hits}$  and  $\text{spread} * 0.9 > 0$  then
20      |  $\text{spread} *= 0.9$ ;
21    end
22    if  $\text{accepted} > 0.6 * \text{hits}$  and  $\text{spread} * 1.1 < 1$  then
23      |  $\text{spread} *= 1.1$ ;
24    end
25    accepted = 0;
26  end
27 end
// Optionally smoothen the configuration before doing the
// measurements
// Perform measurements

```

from different paths that also join \vec{x} and $\vec{x} + \vec{a}_\mu$, so called *staples*,

$$U_\mu(\vec{x}) = (1 - \alpha)U_\mu(\vec{x}) + \frac{\alpha}{6} \sum_{i=1}^6 \text{staple}_i, \quad (2.84)$$

with α governing the fattening of the link. This is schematically depicted in Fig. 2.16. This simple method does not result in $SU(N)$ elements and more elaborate procedures

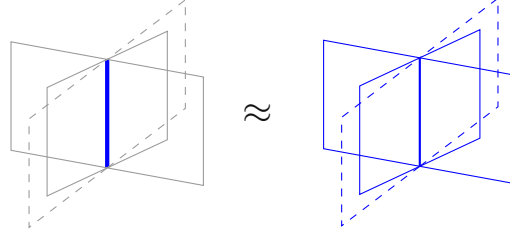


Figure 2.16: A fat link is obtained by averaging the 6 staples and the link itself. It has to be stressed that this does not result in an $SU(N)$ element.

have been developed that preserve the group properties - for example stout or *analytical smearing* [16, 17]. Even more elaborate are the *gradient flow procedures* [18]:

The *Wilson flow* $V_\mu(t, \vec{x})$ is defined via

$$V_\mu(t, \vec{x}) \Big|_{t=0} = U_\mu(\vec{x}), \quad \partial_t V_\mu(t, \vec{x}) = -\frac{2N}{\beta} (\partial_{\vec{x}, \mu} S_{\text{gluons}}(V_\nu(t, \vec{y}))) V_\mu(t, \vec{x}), \quad (2.85)$$

with $S_{\text{gluons}}(V_\mu(t, \vec{x}))$ being the action of the six plaquettes that share the flow $V_\mu(t, \vec{x})$ and the derivative of a function $f(U)$ defined as

$$\partial_{\vec{x}, \mu} f(U_\nu(\vec{y})) = i t_i \frac{d}{ds} f(e^{i s t_i \delta_{\mu\nu} \delta_{\vec{x}\vec{y}}} U_\nu(\vec{y})) \Big|_{s=0}, \quad (2.86)$$

with generators t_i , that is σ_i for $SU(2)$. The action is monotonically decreasing with t and the procedure can be considered as built by an infinite number of infinitesimal stout smearing steps. With increasing t the configuration gets smoother and smoother. With negative t the opposite can be accomplished. With this, enough words on smoothing are given and we will continue with a discussion of several observables.

The path integral formalism allows to evaluate various observables on the lattice. In the next section we will use such observables to set the lattice scale, that is, determine the lattice spacing a . We will also discuss relations to confinement.

2.4 Observables on the lattice

By taking a closer look at Wilson and Polyakov loops we will relate them to the quark anti-quark potential and the free energy of a single quark. Both are directly related to confinement: In confined phase there are no single quarks, hence there is no free energy of a single quark to be measured. Confinement corresponds to a linearly or stronger growing potential. By comparing evaluations of operators in full $SU(2)$ lattice configurations with evaluations taking only the center degrees of freedom into account, it can be tested how well the center vortex model reproduces the observables.

First we want to understand the importance of Wilson loops. We will follow the arguments presented in Ref. [4] and start with the euclidean correlator given by a vacuum to vacuum transition $\langle 0 | \hat{O}_2(t) \hat{O}_1(0) | 0 \rangle$ with arbitrary Operators $\hat{O}_i(t)$. In the Heisenberg picture it can be written as

$$\langle 0 | e^{+t\hat{H}} \hat{O}_2 e^{-t\hat{H}} \hat{O}_1 | 0 \rangle = \sum_n \underbrace{\langle 0 | e^{+t\hat{H}} \hat{O}_2 | n \rangle}_{\langle 0 |} \langle n | e^{-t\hat{H}} \hat{O}_1 | 0 \rangle, \quad (2.87)$$

where we have inserted a unity $\mathbb{1} = \sum_n |n\rangle \langle n|$ and indicated that the vacuum state on the left is unmodified by time propagation. Introducing a basis spanned by the Hamiltonian $\hat{H} |n\rangle = E_n |n\rangle$ we can evaluate this to

$$\langle 0 | e^{+t\hat{H}} \hat{O}_2 e^{-t\hat{H}} \hat{O}_1 | 0 \rangle = \langle 0 | \left(\sum_n e^{-t a E_n} U_C |n\rangle \langle n| U_C^\dagger \right) | 0 \rangle, \quad (2.88)$$

with $\hat{O}_1 = U_C^\dagger$ creating an excited state $|n\rangle$ from the vacuum $|0\rangle$ and $\hat{O}_2 = U_C$ destroying the excitation some time t later.

The energy E_n corresponds to the n -th excitation of whatever system is created with U_C^\dagger . Within the evaluation of the corresponding path integral the excitations are exponentially suppressed with growing t due to the term $e^{-t E_n}$ and one can measure the lowest excitation with sufficient large loop sizes.

Now consider a Wilson loop of size $r \times t$ in temporal gauge. The parts of the loop in time direction can be set to unity and only two components in space direction remain

$$\langle W(r, t) \rangle |_{\text{temporal gauge}} = \langle U_C(t) U_C^\dagger(0) \rangle, \quad (2.89)$$

see Fig. 2.17. Comparing to $\psi(\vec{x}) U_C \bar{\psi}(\vec{x} + r * \vec{a}_x)$ it can be easily seen that they transform identical under gauge transformations. Hence we can assume that the quark propagator for quarks of infinite mass reduces to this U_C^\dagger but leave this to the literature [4].

The energy E_0 is proportional to the potential energy of an infinitely heavy quark antiquark pair $V(r * a)$ separated by a distance that is given by the spacial extent of the Wilson loop

$$\langle W(r, t) \rangle \propto e^{-ta * V(ra)} (1 + \mathcal{O}(e^{-ta * (V(ra) - E_1)})). \quad (2.90)$$

To suppress the systematic error due to higher excitations, large values of t should be used.

Usually one is interested in the string tension σ , the slope of the linear rising potential when assuming a potential of form

$$V(ar) = V_0 + \frac{C}{ar} + \sigma ar, \quad (2.91)$$

with constant term V_0 and constant C governing the dominance of the Coulomb part. It can be extracted from different sized Wilson loops via *Creutz-ratios*

$$\chi(r, t) = -\ln \frac{\langle W(r+1, t+1) \rangle \langle W(r, t) \rangle}{\langle W(r, t+1) \rangle \langle W(r+1, t) \rangle} \approx \sigma a. \quad (2.92)$$

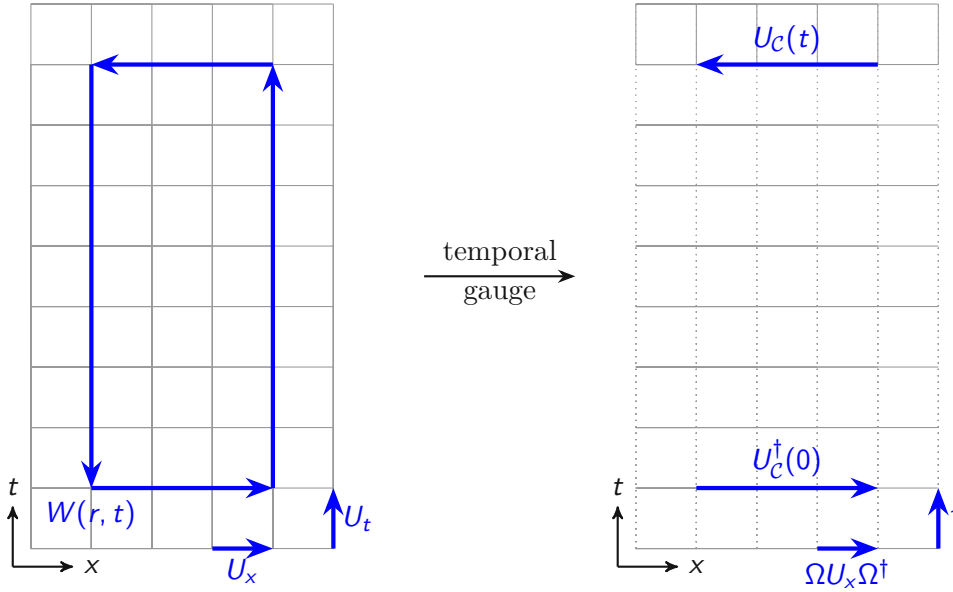


Figure 2.17: A $r \times t$ Wilson loop can be interpreted as the creation of a particle antiparticle pair at time 0 and their annihilation at time t . This is more easily seen in temporal gauge with all links in time direction within the loop fixed to unity.

Knowledge of the potential allows to set the scale, that is, to determine the lattice spacing a in physical units: By identifying that value of ar for which

$$\frac{dV}{dar}(ar)^2 = 1.65 \Rightarrow ar = r_0 \simeq 0.5 \text{ fm} \Rightarrow a \simeq \frac{0.5}{r} \text{ fm}, \quad (2.93)$$

the scale can be set with r being a dimensionless count of lattice spacings and r_0 the Sommer parameter [19]. The string tension itself is another physical observable that can be used to attain the physical value of the lattice spacing. By setting it to its physical value of $(440 \text{ MeV})^2$ one obtains

$$\sigma_{\text{physical}} = \sigma_{\text{lattice}}/a^2 = (440 \text{ MeV})^2 = \frac{440^2}{197^2} \text{ fm}^{-2} \Rightarrow a = \sqrt{\sigma_{\text{lattice}}} * \frac{197}{440} \text{ fm}. \quad (2.94)$$

The value of $(440 \text{ MeV})^2$ is related to the pion mass via Regge trajectories [20] and can further be related to the string breaking distance.

A sanity check of vortex specific measurements is given by a comparison of the string tension in the full $SU(2)$ configuration with the string tension in the Z_2 part of the configuration. The latter is calculated after center vortices are detected by multiplying only the signs of $\text{Tr}(U_\mu(\vec{x}))$ of the links that build the respective Wilson loop instead of the full $SU(2)$ matrix. The string tension is an order parameter for confinement: a vanishing string tension indicates deconfinement.

Let us now interpret the Wilson loop as a measure of flux and write it according to Eq. (2.64) as

$$W_i = \text{Tr}(\cos(\alpha_i) \mathbb{1}_2 + i \sin(\alpha_i) \vec{\sigma} \vec{n}_i), \quad (2.95)$$

with index i collecting reference point, size and plane of the loop. The flux relates to the imaginary part of the loop, hence increases with the trace approaching zero. The vector $\vec{\sigma}$ denotes the Pauli matrices and the unit vector \vec{n} will be referred to as color vector. The trace is given by $2 * \cos \alpha_i$. The color vectors average to zero within the path integral: The color vector is not gauge invariant, hence no physical observable. But by relating two different Wilson loops W_i and W_j to the same point of reference via a parallel transport it can be used to define the *color homogeneity* h_{S_2} ,

$$h_{S_2} := \frac{1}{2} * | \vec{n}_i + \vec{n}_j | . \quad (2.96)$$

This observable vanishes if the two color vectors are anti-parallel and it is 1 for parallel color vectors. It has to be stressed that it is only defined properly for $W_i \neq \pm 2$ and $W_j \neq \pm 2$, that is, non of of the two Wilson loops evaluates to a center element. In Fig. 2.18 three different geometric positions of the respective plaquettes are depicted and allow to define different measurements.

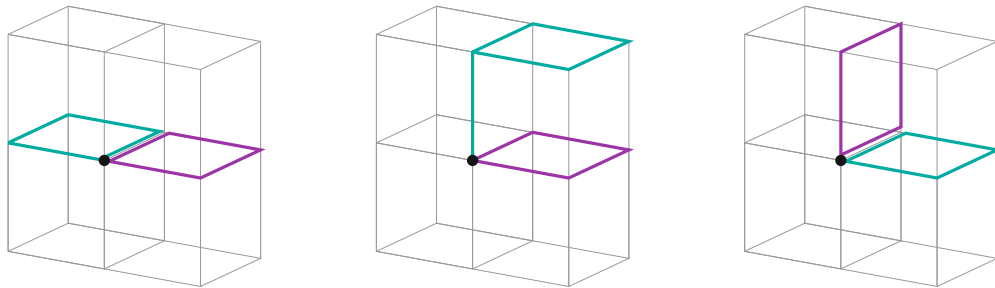


Figure 2.18: By determining the S2-homogeneity for different geometric setups of plaquettes, different properties related to color structure can be measured. On the left side, the homogeneity of flux through two planar loops is measured. We refer to such measurement as *planar homogeneity*. In the middle, the homogeneity along a flux line that pierces both loops is measured. Such measurement will be referred to as *longitudinal homogeneity*. On the right side, the longitudinal homogeneity is measured for a strongly curved flux line.

- Comparing two neighbouring plaquettes which are in the same plane allows to measure the homogeneity of a thick flux tube that pierces through both plaquettes: the *planar homogeneity*.
- comparing two parallel plaquettes which are on top of each other, one can check how homogeneous the color stays along a straight flux line: the *longitudinal homogeneity*.
- by comparing two orthogonal plaquettes that share a link, one can measure the longitudinal homogeneity of a curved flux line.

The definition can be easily generalized to an arbitrary number of plaquettes or bigger loops. By taking not only the color vectors \vec{n}_i but the full 4-dimensional vector $(c_j)_i$ from Eq. (2.64) into account, a S3-homogeneity can be defined. Before discussing the

Polyakov loop we will now argue why the S2-homogeneity should be preferred over the S3-homogeneity with respect to vortices and cooling.

The S2-homogeneity is more stable under the influence of cooling than the S3-homogeneity. This can be seen in the histograms shown in Fig. 2.19 where four planar plaquettes are used to calculate the homogeneity. The histogram of the S3-homogeneity becomes more

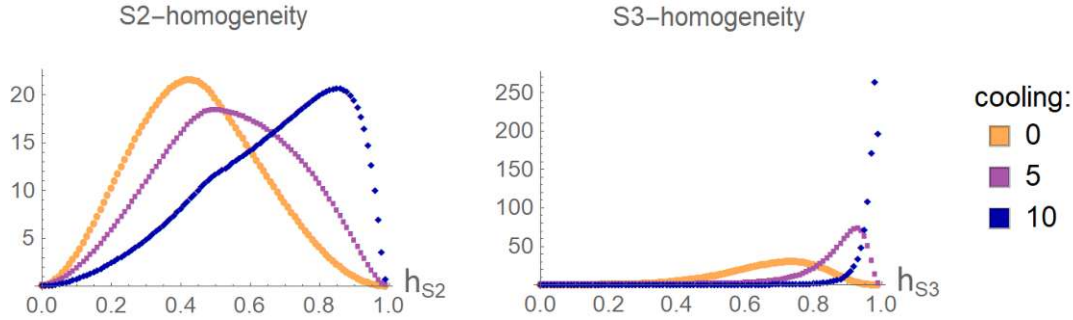


Figure 2.19: Histograms of the S2-homogeneity (left) and the S3-homogeneity (right) are compared with respect to cooling. The data was taken from 400 Wilson configurations per number of cooling steps in an lattice of size 18^4 .

and more narrow when cooling is applied, whereas the S2-homogeneity keeps a broad histogram. By comparing the homogeneity of loops that are pierced by a vortex with the average homogeneity of all loops it can be seen that the S2-homogeneity stays sensitive to vortex piercings when cooling is applied whereas the S3-homogeneity loses its sensitivity to vortex piercings, see Fig. 2.20. With this, the merits of the S2-homogeneity over the

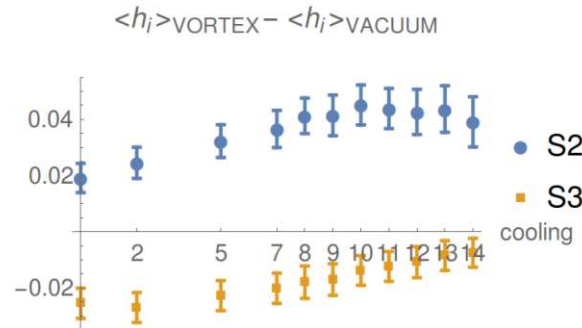


Figure 2.20: When cooling is applied, the S3-homogeneity loses its sensitivity for vortex piercings whereas the sensitivity of the S2-homogeneity is kept. The data is taken from 25 Wilson configurations per number of cooling steps in an lattice of size 12^4 with a four plaquette homogeneity.

S3-homogeneity are clarified and we can continue with the discussion of the Polyakov loop.

Polyakov loops can be related to Wilson loops: Increasing one length of the Wilson loop until it spans the lattice, two Polyakov loops do emerge, see Fig. 2.21. Such Wilson loop can be interpreted as two Polyakov loops that are parallel transported to the same point

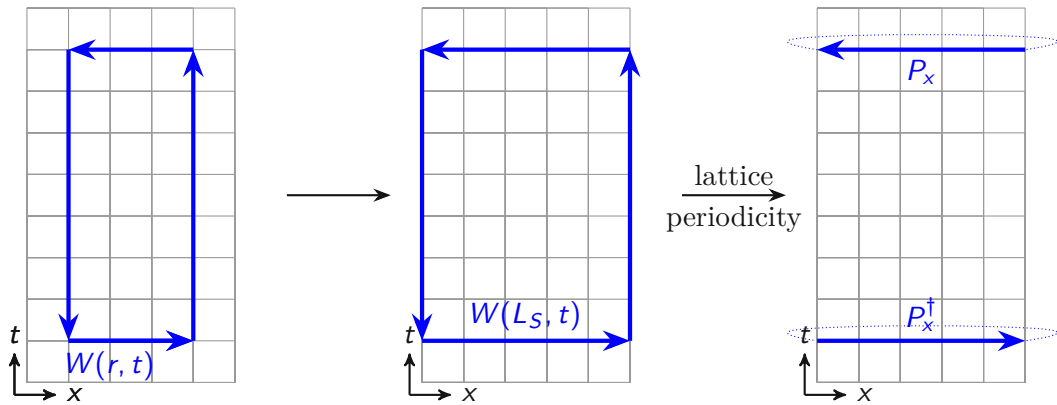


Figure 2.21: A Polyakov loop corresponds to an infinitely separated quark anti-quark pair, that is, two free quarks. This relation can be intuitively understood by considering two Polyakov loops that result from a Wilson loop that is expanded over the lattice.

of reference. Due to the lattice periodicity we end up with two pairs of infinitely separated quarks and anti-quarks that exist for a specific time interval. We will now follow the way from pairs of Polyakov loops to a single Polyakov loop. If the two Operators $P_x(t_2)$ and $P_x^\dagger(t_1)$ are sufficiently far apart, they are not correlated and we can write

$$\langle P_\mu(t_2) P_\mu^\dagger(t_1) \rangle \stackrel{*}{\approx} \langle P_\mu(t_2) \rangle \langle P_\mu^\dagger(t_1) \rangle = \langle P_\mu \rangle^2, \quad (2.97)$$

*if $|t_2 - t_1| \gg 0$

with the single Polyakov loop P_μ being gauge invariant. It is related to the free energy of a free quark. In the confined phase it vanishes: There are no free quarks. In the deconfined phase it evaluates to non-vanishing values. Hence, the Polyakov loop can be seen as an order parameter for deconfinement. A phase transition can only be observed at finite temperature, that is, in asymmetric lattices. Throughout this work we use symmetric lattices and stay in confined phase.

The observables can be evaluated in full $SU(2)$ configurations as well as in center projected Z_2 configurations that are related to vortices. This allows to check for deviations of the center vortex model from $SU(2)$ QCD. We will now look at the procedures for vortex detection.

Detecting center vortices

For the detection of center vortices, three strongly inter-related objects are of relevance: thick vortices, P-vortices and non-trivial center regions. In this chapter we discuss these objects and present how our method of vortex detection makes use of them. A successful vortex detection is schematically depicted in Fig. 3.1. The relevant algorithms will be

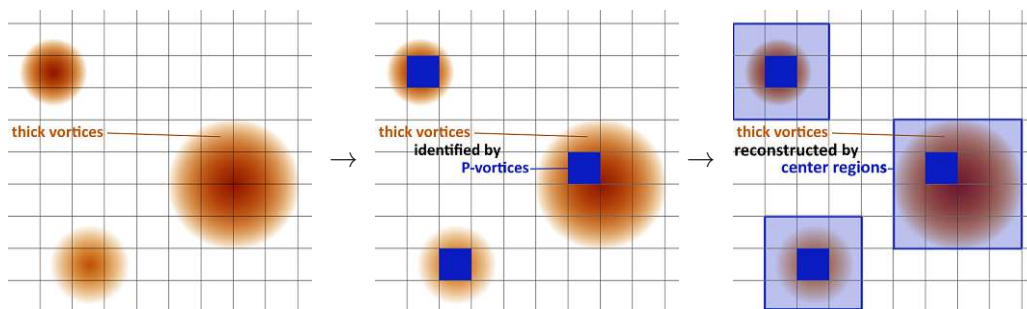


Figure 3.1: Two dimensional slices through a four dimensional lattice are depicted. The vortex detection starts as a best fit procedure of P-Vortices to thick vortices, indicated by the first arrow. Then, starting from the detected P-plaquettes, non-trivial center regions are identified to reconstruct the thick vortex. These non-trivial center regions are in general not rectangular.

described in detail and presented in pseudo-code so that they can be easily rebuilt in any programming language. As computational power is a rare resource when performing lattice simulations, we also mention the worst case runtime of the most intensive parts of the algorithms. Simulations at different lattice parameters need to be run for approaching the continuum limit. The numeric nature of lattice simulations and the vortex physics restrict the functionality of the algorithms to a specific range of parameters.

It is assumed that *thin vortices*, percolating the vacuum, correspond to *thick vortices* on the lattice. These gauge invariant objects are usually detected by gauge dependent *P-vortices*, which are in turn identified by *P-plaquettes*. The central goal of vortex detection

is to locate the thick vortices within lattice simulations. As long as identified P-vortices locate thick vortices we speak of a given *vortex finding property*. The algorithms to be presented manage to preserve this property where older procedures fail. A loss of the vortex finding property can have several causes: a failure of the gauge fixing, too harsh cooling or smoothing procedures or Gribov problems, to list some of them. Once, the P-vortices are correctly identified with given vortex finding property, thick vortices can be reconstructed using *non-trivial center regions* and a study of the vortices percolating the vacuum becomes possible.

The constituents of the whole procedure and how they can be put together to overcome some troubles occurring during vortex detection are presented in the following. Center regions can be used to overcome ambiguities of the gauge fixing procedure required to identify P-vortices and they are used to reconstruct thick vortices from identified P-plaquettes.

The following sections summarize and complement content published in Refs. [21, 22, 23, 24] and document the whole vortex detection procedure in one place.

3.1 Center regions

We first motivate the concept of *center regions* from a theoretical point of view before we relate them to center vortices and present the algorithms to identify non-trivial center regions. These algorithms will be again of relevance when reconstructing thick vortices. The non-trivial center regions allow already to overcome ambiguities of the gauge fixing procedure: They can be used to counteract the Gribov problem in the gauge fixing procedure.

We start with a non-Abelian generalization of the Abelian stokes theorem

$$\begin{aligned}
 P \exp \left(i \oint_{\partial S} A_\mu dx^\mu \right) &= \mathcal{P} \exp \left(\frac{i}{2} \int_S \mathcal{F}_{\mu\nu} dx^\mu dx^\nu \right) \\
 \mathcal{F}_{\mu\nu} &= U^{-1} F_{\mu\nu} U \quad U = P \exp \left(i \int_l A_\eta dy^\eta \right)
 \end{aligned}
 \tag{3.1}$$

with P denoting path ordering, \mathcal{P} "surface ordering" and l being a path from the base O of ∂S to \vec{x} , see [25]. The left hand side of Eq. (3.1) can be identified as the evaluation of a Wilson loop around the region S . The right hand side can be expressed using plaquettes $U_{\mu\nu}(\vec{x})$ via

$$U_{\mu\nu}(\vec{x}) = \exp \left(i a^2 F_{\mu\nu} + \mathcal{O}(a^3) \right),
 \tag{3.2}$$

with lattice spacing a and leads to a product of all the plaquettes building the region S , see [4]. With these ingredients the non-Abelian stokes theorem can be written schematically on the lattice as depicted in figure 3.2. It can be used to factorize a Wilson loop into plaquettes referenced to the same lattice site. This factorization is built out of non-commuting elements with the path ordering and the surface ordering. If we find within

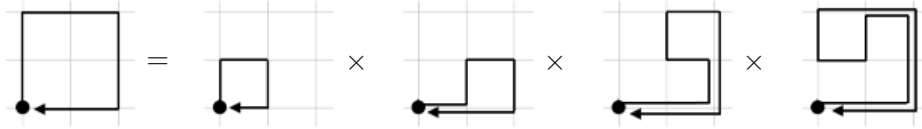
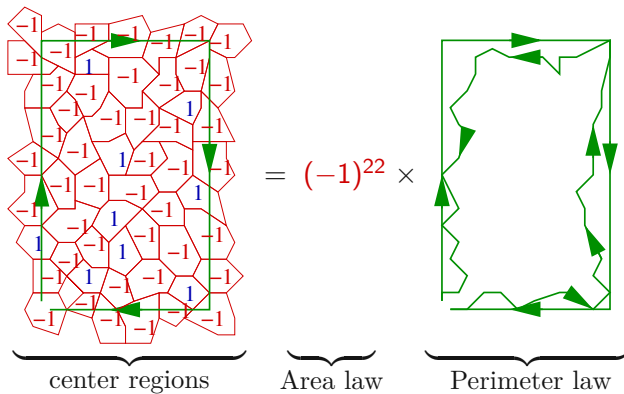


Figure 3.2: The non-Abelian Stokes theorem on the lattice can be used to factorize arbitrary Wilson loops into factors of plaquettes referenced to the same lattice site. The path connecting each plaquette with this lattice site corresponds to the path ordering P used in Eq.3.1.

this factorization neighbouring factors evaluating to a center element, we can pull them in front of the other non-commuting factors: in $SU(2)$ they comprise nothing more than a sign, hence commute with all other factors. By dividing the region S into subregions whose boundaries evaluate to center elements, we can further factorize the Wilson loop into center-regions: we collect all center factors to the left and keep all remaining factors at the right, see Fig. 3.3.



Regions, whose boundaries evaluate to center elements can be used to factorize a Wilson loop into two parts:

- an area factor collecting the fully enclosed non-trivial regions, leading to a linear rising potential,
- a perimeter factor from non-center contributions due to partially enclosed center regions.

Figure 3.3: Center regions explain the Coulombic behaviour and the linear increase of the quark anti-quark potential as they lead to an area law and a perimeter law for Wilson loops.

We now consider each 2-dimensional slice through the lattice and assume that they are covered by non-overlapping center regions. With constant density of non-trivial center regions, the center factor directly relates to the area of the Wilson loop: the bigger the loop, the more negative signs will be acquired due to the enclosed non-trivial center regions. The average trace of a Wilson loop approaches zero with increasing loop area. This behavior corresponds to a linearly rising static quark anti-quark potential causing confinement.

The second factor is related to center regions that are not fully enclosed but intersected by the Wilson loop. As this intersection requires the center region to be sufficiently near to the perimeter of the Wilson loop a perimeter law arises resulting in an Coloumbic potential.

The expected quark anti-quark potential is obtained: Coloumbic for small separations and linearly rising for sufficiently large separations. Thus, center regions are directly

related to confinement. As they are solely identified by the trace of Wilson loops they are gauge invariant objects: They do not suffer from the Gribov problem.

We will later see that trivial center regions can be considered as regions that are pierced an even number of times by a P-vortex. In turn, non-trivial center regions can be considered as regions that are pierced an odd number of times by a P-vortex. Being pierced by a P-vortex is equivalent to enclosing a P-plaquette. This will be used to guide the detection of P-vortices via P-plaquettes. It allows to overcome ambiguities of the gauge fixing procedure, counteracting a loss of the vortex finding property during the identification of P-plaquettes.

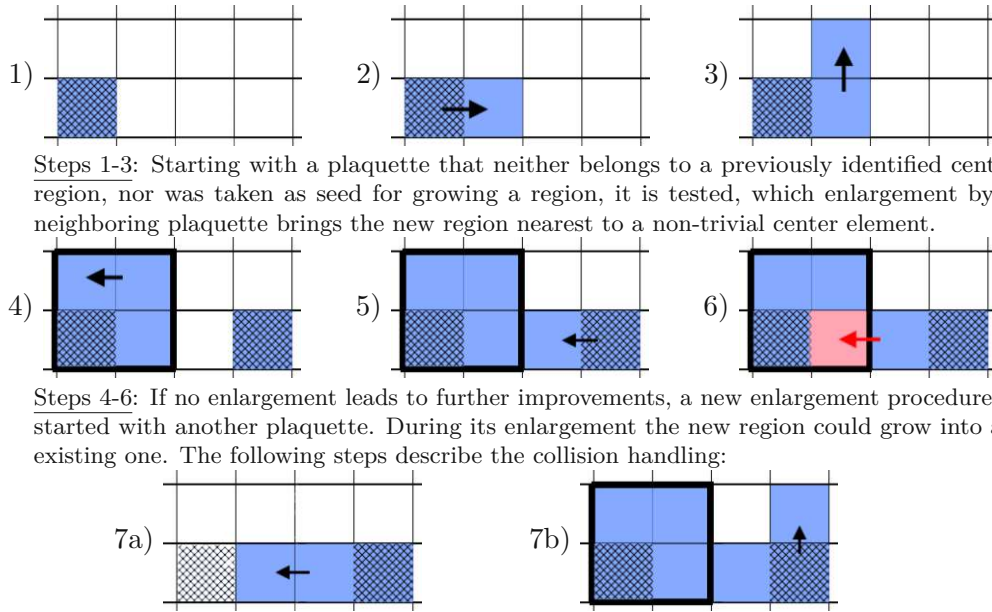
Non-trivial center regions that are pierced exactly once can be considered to enclose a thick vortex. This allows reconstructing thick vortices from identified P-plaquettes: Non-trivial center regions are to the thick vortices, what P-plaquettes are to the P-vortices. With this, the importance of center regions is motivated and we will now present the algorithm for detecting non-trivial center regions. We also give a rough estimate for the asymptotic worst case runtime of the procedures.

The central idea is to start with smaller regions defined by the perimeter of single plaquettes, so called *seeds*. These seeds are enlarged by combining plaquettes to form bigger and bigger loops so that growing regions evaluate nearer and nearer to a non-trivial center element. This enlargement procedure is repeated until no further enlargement brings the evaluation nearer to a non-trivial center element. Then the procedure is repeated with a new seed that neither belongs to an already identified non-trivial center region nor was taken as seed previously.

Whenever a growing region comes into conflict with an already identified one, some collision handling has to be performed: We let the "better" region survive at the cost of deleting the other region. Those plaquettes of the deleted region that have not been taken as seed can be used again as seed for growing a new region. The seed of the deleted regions is excluded as seed for new growing procedures to guarantee halting of the procedure.

The overall procedure stops when each plaquette of the lattice either belongs to an identified non-trivial center region or was taken once as a seed. Thus, the runtime of the algorithm depends not only on the lattice size but also on the specific field configuration encoded in the lattice: if many collisions result in deletions, many calculations get thrown away.

In Fig. 3.4 the central aspects of the procedure are depicted. Considering the runtime, in worst case every plaquette has to be taken once as seed with the majority of regions getting deleted due to collisions. From this we can expect, that the number of executions of the enlargement procedure is proportional to N_{pla} , the number of plaquettes of the lattice. During each of these executions, the best enlargement is identified by evaluating all possible enlargements. Each link belonging to the perimeter of the growing region can be pushed outwards to enlarge the region around a neighbouring plaquette. The number of possible enlargements starting from a single plaquette is again proportional



Steps 1-3: Starting with a plaquette that neither belongs to a previously identified center region, nor was taken as seed for growing a region, it is tested, which enlargement by a neighboring plaquette brings the new region nearest to a non-trivial center element.

Steps 4-6: If no enlargement leads to further improvements, a new enlargement procedure is started with another plaquette. During its enlargement the new region could grow into an existing one. The following steps describe the collision handling:

Step 7a: The evaluation of the growing region is nearer to a non-trivial center element than the evaluation of the old region: Delete the old region, only keeping the mark on its seed plaquette and allow growing.

Step 7b: The growing region deviates more from a non-trivial center element than the existing one: try other enlargements.

Figure 3.4: The algorithm for the detection of non-trivial center regions repeats the depicted procedures until every plaquette either belongs to an identified region or has been taken once as seed for growing a region. The arrow marks the direction of enlargement, plaquettes belonging to a identified region are colored, plaquettes already used as seed are shown shaded.

to the total number of plaquettes, resulting in an overall worst case runtime of $\mathcal{O}(N_{\text{pla}}^2)$ ($\mathcal{O}(L_{\text{latt}}^8)$ with lattice extent L_{latt}) times the runtime of a single enlargement trial.

The whole concept is based on double linked-lists: Each link within the list defining the perimeter of the region stores additional pointers to its proceeding and successive link. Once the full perimeter of the seed plaquette is evaluated the enlargement trial can be performed with a constant number of matrix multiplications. In Fig. 3.5 the necessary matrix multiplications on the double-connected list are schematically depicted. Our current implementation does only store the evaluation of the path ordered perimeter throughout a single enlargement step and recalculates it for the next enlargement. The procedure could be improved with respect to the runtime by storing the relevant evaluations throughout the whole enlargement procedure.

A pseudo-code description of the overall procedure is presented in algorithm 3.1. Keeping the intermediary results is not explicitly given in the description, but takes place in the loop from line 10 on when calculating the new evaluation in line 12. Throughout the enlargement procedure the evaluation of each region is stored so that the calls of " $Tr()$ "

3. DETECTING CENTER VORTICES

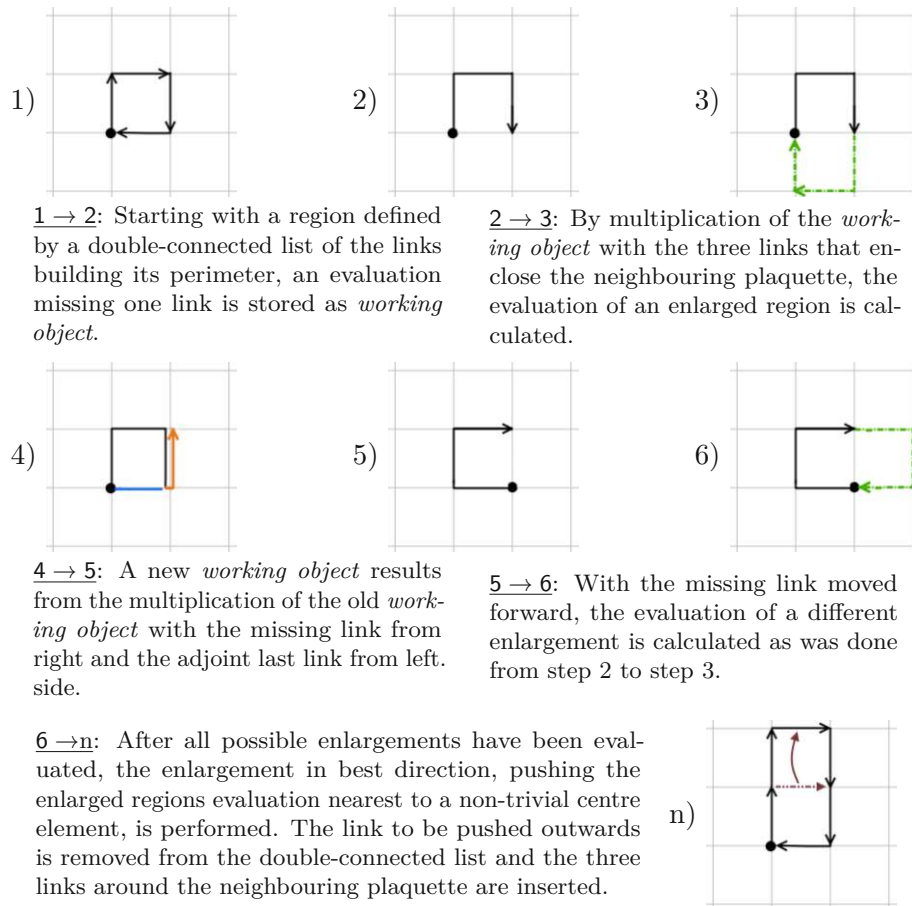


Figure 3.5: The depicted procedure is repeated until no further enlargement gets closer to a non trivial center element.

do not require a full evaluation of the respective region. Thus, the collision handling does not require a full re-evaluation of the respective regions.

Algorithm 3.1: Detection of non-trivial center regions**Data:** S_{pl} = stack of all plaquettes sorted by rising trace.**Result:** List of non-trivial center regions C_R , each given as a double-connected list of links.

```

1 while  $S_{pl}.size() > 0$  do
2   markPlaquette( $S_{pl}.Last()$ );
3    $C_R.push\_back(convertToDoubleConnectedList(S_{pl}.last()))$ ;
4    $S_{pl}.remove\_last()$ ;
5   repeat
6     link bestLink = none;
7     double bestEvaluation =  $Tr(C_R.last())$ ;
8     integer collidedWith = none;
9     for each link as  $l$  within  $C_R.last()$  do
10      plaquette neighbour = plaquette,  $l$  will be pushed over;
11      double newEvaluation =  $Tr(C_R.last()$  with  $l$  pushed outwards);
12      integer collisionID = ID of region neighbour-plaquette belongs to or
13      none;
14      if  $newEvaluation < bestEvaluation$  then
15        if  $collisionID == none$  or  $Tr(C_R[collisionID]) > newEvaluation$ 
16          then
17            bestEvaluation = newEvaluation;
18            bestLink =  $l$ ;
19            collidedWith = none;
20          end
21          if  $Tr(C_R[collisionID]) > newEvaluation$  then
22            collidedWith = collisionID;
23          end
24        end
25      if bestLink  $\neq$  none then
26         $C_R.last().EnlargeByPushingLinkOutwards(bestLink)$ ;
27         $S_{pl}.remove(plaquette$  that got added to the region  $C_R.last()$ );
28        if  $collidedWith \neq none$  then
29          for each plaquette as  $p$  within  $C_R[collidedWith]$  do
30            if  $isMarked(p) == False$  then
31               $S_{pl}.push\_back(p)$ ;
32            end
33          end
34           $C_R.delete(collidedWith)$ ;
35        end
36      end
37    until bestLink == none;
38  end

```

In practice the non-trivial center is never reached. Hence we select a set of regions with most negative trace to guide the gauge fixing procedure.

We assume that the good non-trivial center regions evaluate somewhere near to the non-trivial center, while bad non-trivial center regions can evaluate arbitrary near to the trivial center. Our method of collision handling causes better non-trivial center regions to replace some worse regions. Hence we chose an upper limit for the trace up to which the identified regions should be taken into account. This upper limit is determined dynamically for a given list of center regions:

We sort the regions by rising trace and look for an inflection point, see Fig. 3.6. For a

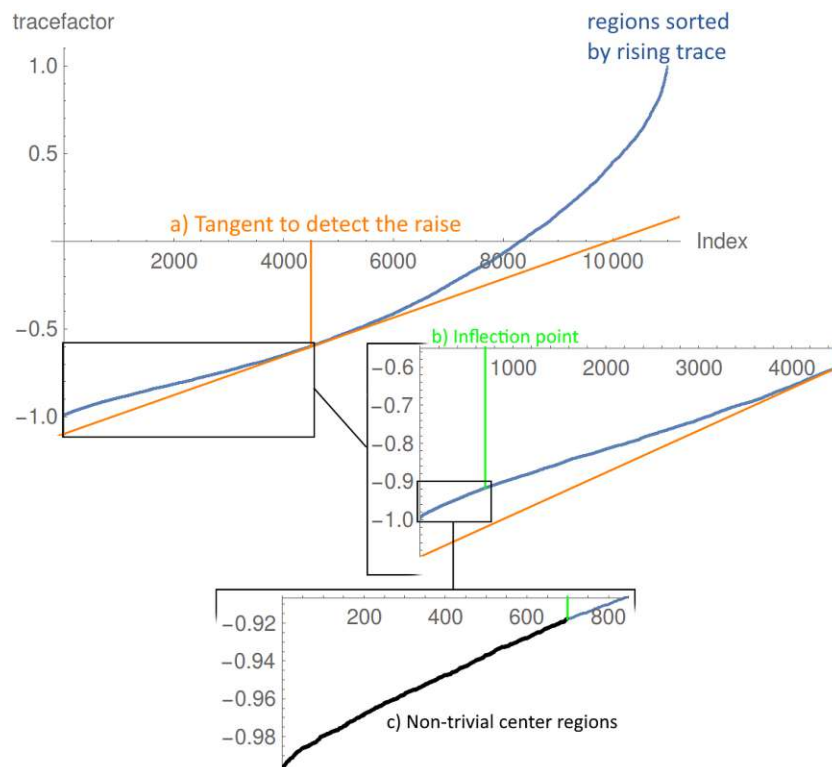


Figure 3.6: Many of the detected non-trivial center regions do not evaluate sufficiently near to a non-trivial center element. Selecting non-trivial center regions for the guidance of the gauge fixing procedure starts with sorting the regions by rising trace factor. a) Then, a tangent (orange line) through the point at index 0 and tracefactor equal to 1.1 times the tracefactor of the first regions within the list is identified. b) Up to the index at which the tangent touches the blue line, an inflection point is identified. c) All regions with index below the inflection point are selected for guidance.

smooth configuration we expect a single inflection point. On the lattice it can be hidden in noise. The numerical determination needs careful investigation. The procedure is documented in algorithm 3.2.

Algorithm 3.2: Selection of non-trivial center regions**Data:**

- C_R , list of center regions.
- srt , indices of center regions sorted by rising tracefactor.

Result: maximal ID $maxID$ of srt up to which regions are taken for guidance at the gauge fixing procedure

```

1 double minK=10;
2 integer riseID=1, maxID=1;
  // find tangent with minimal slope
3 for id=1 to  $C_R.size()$  do
4   if  $Tr(C_R[srt[id]]) > 0$  then break;
5   double k =  $\frac{Tr(C_R[srt[id]]) - Tr(C_R[srt[0]]) * 1.1}{id - 0.9}$ ;
6   if  $k < minK$  then
7     minK = k;
8     riseID = id;
9   end
10 end
  // find the one relevant inflection point
11 maxID = riseID ;      // no regions above riseID will be taken
12 integer strt=1, stp=riseID, signchanges=0;      // search-interval
13 integer h=1;      // step-width for second difference quotient
14 double dd =  $Tr(C_R[srt(strt+2*h)]) - 2 * Tr(C_R[srt(h+strt)]) + Tr(C_R[srt(strt)])$ ;
15 for id=strt + h to stp - h do
16   double dd' =  $Tr(C_R[srt(id+2*h)]) - 2 * Tr(C_R[srt(h+id)]) + Tr(C_R[srt(id)])$ ;
17   if  $dd * dd' \leq 0$  then
18     dd=dd';
19     signchanges++;
20     riseID=id;
21     if  $signchanges > 1$  then
22       h++;
23       signchanges=0;
24       goto line 14;
25     end
26   end
27   dd=dd';
28 end
29 maxID = riseID;
30 if  $stp - strt > 3$  then
31   strt = maxID+1-h;
32   stp = maxID+1;
33   h=1;
34   goto line 14;
35 end

```

The first step consist in identifying the index at which a strong rise of the trace within the list of center regions sorted by rising trace occurs. We can reduce the interval in which we search for the inflection point by fitting an appropriate tangent to the distribution, see Fig.3.6 and lines 1 to 10 in algorithm 3.2. The index at which the tangent touches the curve of the listed regions defines an upper limit to a search interval. In this search interval we identify the inflection point by looking for a sign change of the second difference quotient. To cope with the fluctuations of the data, the step-width used to calculate the difference quotient is step-wise increased until only a single inflection point is found. Then, from lines 30 to 35, the search interval is reduced and the procedure repeated until the inflection point is located within a sufficiently small interval.

The non-trivial center regions with traces below this limit guide the gauge fixing procedure used to locate the P-plaquettes that identify the P-vortex. The algorithms and their physical backgrounds are presented in the following.

3.2 P-Vortices

P-vortices are thin, closed surfaces in 4-dimensional spacetime. They are built by closed flux lines evolving in time. Given, the vortex finding property holds, they locate thick vortices. P-vortices themselves are identified by looking for P-plaquettes, plaquettes that evaluate to the non-trivial center after projection to the center degrees of freedom in a maximal center gauge. In the vortex picture it is assumed that these P-plaquettes are pierced by the flux line that builds the P-vortex. Fig. 3.7 schematically depicts the relation between the closed surface of the P-vortex, the flux line building the P-vortex and the P-plaquettes that are pierced by the flux line.

The flux building the P-vortex is conserved. This corresponds to a geometric relation: given a P-plaquette, in all four of its neighbouring unit cubes another plaquette has to be pierced. A plaquette is considered pierced if it is built by an odd number of non-trivial links. For each non-trivial link one of the following holds: either it belongs to a P-plaquette or it belongs to a plaquette containing an even number of non-trivial links. The volume enclosed by the vortex, the *Dirac volume*, is occupied by non-trivial links. The detection of P-vortices is based on identifying the Dirac volume, which is done in *Maximal Center Gauge* (MCG) and directly allows to identify the plaquettes pierced by the P-vortex, the P-plaquettes.

The concept of "being pierced" can be extended from plaquettes to bigger Wilson loops: each piercing contributes a non-trivial factor to the evaluation of a Wilson loop, see Fig. 3.8, but this non-trivial factor does not need to be localized on a single link. It can extent over an arbitrary number of links. Such spread out center flux corresponds to a thick vortex. We want to stress again: P-plaquettes are to the P-vortex, what the non-trivial center regions are to the thick vortex and each trivial center region has to contain an even number of P-plaquettes and each non-trivial center region contains an odd number of P-plaquettes. This knowledge is used to guide the detection of P-plaquettes by enforcing that the non-triviality of regions is preserved during the gauge

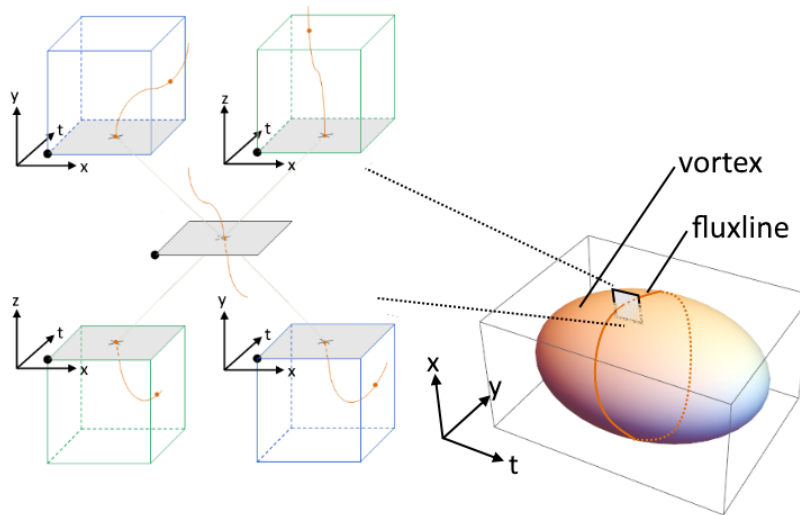


Figure 3.7: The geometric relation between piercings, the flux line and the vortex surface is depicted schematically. Left: A flux line (depicted as orange line) can be traced by following non-trivial plaquettes after transformation to maximal center gauge and projection to the center degrees of freedom. Each non-trivial plaquette belongs to four elementary cubes, where the flux enters and has to leave through another plaquette. The depicted grey rectangles correspond to the same plaquette. For each cube, the three involved coordinates are indicated. Right: Due to the evolution in time, the flux line forms a closed two-dimensional surface in four-dimensional spacetime. This is only a schematic diagram because it is difficult to depict the four dimensional geometry of the vortex.

fixing procedure and center projection. This guidance ensures that also in the case of a center element spread over many links, an odd number of P-plaquettes are enclosed. The overall procedure of this *Guided Maximal Center Gauge* (GMCG) will be presented in the following.

3.2.1 The Guided Maximal Center Gauge

The *Guided Maximal Center Gauge* (GMCG) is based on a *Direct Maximal Center Gauge* [26], but uses *simulated annealing* to find gauge matrices $\Omega(x)$ so that

$$U'_\mu(\vec{x}) = \Omega(\vec{x})U_\mu(\vec{x})\Omega^\dagger(\vec{x} + \vec{a}_\mu) \text{ maximizes } R_{\text{MCG}} = \sum_{\vec{x}} \sum_{\mu} |\text{Tr}(U'_\mu(\vec{x}))|^2. \quad (3.3)$$

It brings each link as near to a center element as possible.

The simulated annealing procedure is modified using center projection, projecting the single links to the closest center element. Preserving the non-triviality of center regions ensures that no flux building the vortex is lost:

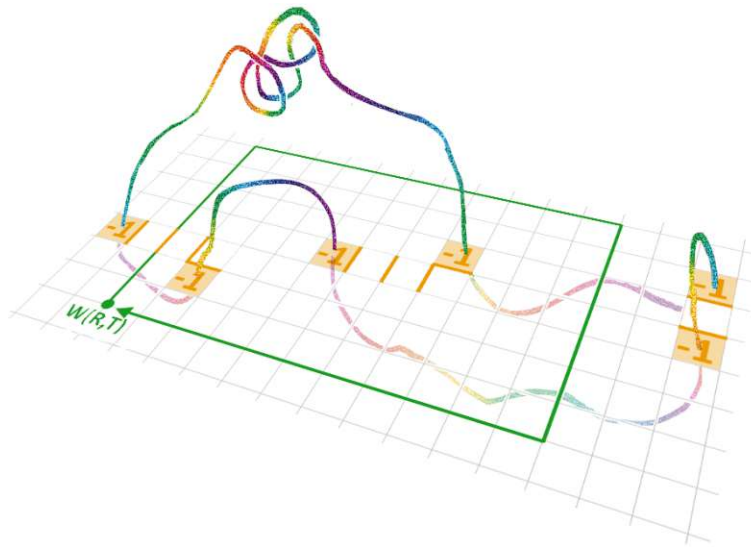


Figure 3.8: A flux line of a vortex can be traced by following non-trivial plaquettes (depicted in orange with a "-1") after transformation to maximal center gauge and projection to the center degrees of freedom: each P-plaquette is considered pierced by the vortex. Every piercing contributes a non-trivial factor to an enclosing Wilson loop $W(R,T)$.

- We prevent gauge transformations that would result in a non-trivial center region projecting to the trivial center.
- We enforce transformations resulting in non-trivial regions projecting to the non-trivial center.

A Pseudo-code description of the overall procedure is give in Algorithm 3.3.

Algorithm 3.3: Guided Maximal Center Gauge**Data:**

- $U_\mu(x)$, gluonic SU(2)-link at site x pointing in direction μ
- N_S , number of sweeps to be performed,
- C_R , non-trivial center regions as double-connected lists of their links.

Result: $U_\mu(x)$ in maximal center gauge **preserving non-trivial center regions**

```

1 double spread = 1,  $T_{SA} = 2$ ,  $\Delta T = \frac{T_{SA}}{N_S+0.5}$ ;
2 for sweeps = 1 to  $N_S$  do
3   integer Accepted = 0;
4   for hits=1 to 10 do
5     for all LatticeSites  $x$ , never selecting neighbours one after the other do
6       double  $\theta = \frac{\pi}{2} * \text{spread} * \text{rnd}()$ ,  $\vec{n}$  = random unit vector;
7       matrix  $\Omega = \cos(\theta) * \mathbb{1} + i * \sin(\theta) * \sum_{i=1}^3 n_i * \sigma_i$ ;
8       double  $R_{MCG} = \sum_\mu (| \text{Tr}[U_\mu(x)] |^2 + | \text{Tr}[U_\mu(x - e_\mu)] |^2)$  ;
9        $c_-$  = count of  $C_R$  evaluating to  $-1$  calculated on center projected  $U_\mu$ ;
10       $c_+$  = count of  $C_R$  evaluating to  $+1$  calculated on center projected  $U_\mu$ ;
11      for  $\mu = 1$  to 4 do
12        |  $U'_\mu(x) = \Omega U_\mu(x)$ ;  $U'_\mu(x - e_\mu) = U_\mu(x - e_\mu) \Omega^\dagger$ ;
13      end
14      double  $R'_{MCG} = \sum_\mu (| \text{Tr}[U'_\mu(x)] |^2 + | \text{Tr}[U'_\mu(x - e_\mu)] |^2)$ ;
15       $c'_-$  = count of  $C_R$  evaluating to  $-1$  calculated on center projected  $U'_\mu$ ;
16       $c'_+$  = count of  $C_R$  evaluating to  $+1$  calculated on center projected  $U'_\mu$ ;
17      double  $T'_{SA} = T_{SA} * (1 + \frac{c_+}{1+c_-+c_+})$ ; // Temperature increase
           proportional to wrong regions
18      if  $\text{rnd}() < \exp\left(\frac{R'_{MCG} - R_{MCG}}{T'_{SA}}\right)$  or  $c'_- > c_-$  then
19        | if  $c'_- \geq c_-$  then
20          | for  $\mu = 1$  to 4 do
21            | |  $U_\mu(x) = U'_\mu(x)$ ;  $U_\mu(x - e_\mu) = U'_\mu(x - e_\mu)$ ;
22          | end
23        | end
24        | Accepted+=1;
25      end
26    end
27  end
28  if  $\frac{\text{Accepted}}{|\text{LatticeSites}|} < 5$  and  $\text{Accepted} * 0.9 > 0$  then
29    | spread* = 0.9;
30  end
31  if  $T_{SA} \leq 2 * \Delta T$  and  $\Delta T * 0.1 > 0$  then
32    |  $\Delta T* = 0.1$ ;
33  end
34   $T_{SA} - = \Delta T$ ;
35 end

```

The central idea is to perform the gauge transformation in small steps using random gauge matrices Ω spreading around unity that are accepted (line 21) or rejected. Independence of the single gauge transformations is achieved by never taking neighbouring sites one after another in line 5: $\Omega(\vec{x} + \vec{a}_\mu) = 1$ for all \vec{a}_μ during the transformation of the lattice site \vec{x} . The gauge matrix is generated in lines 6 and 7 with specific spread from unity using the function `rnd()` which produces random numbers between zero and one. The random unit vector is created using the Box Muller method. For each lattice site the gauge functional with (R_{MCG} in line 8) and without (R'_{MCG} in line 15) gauge transformation is calculated taking into account all 8 links that are connected to the respective lattice site \vec{x} . Also the number of non-trivial center regions that evaluate to $+1$ (c_+ and c'_+) and -1 (c_- and c'_-) respective when evaluated on center projected links is calculated with (lines 9 and 19) and without (lines 15 and 16) the gauge transformation. The single region is evaluated by multiplying the projected links that are part of its perimeter. Then the number of positive and negative regions is counted. Taking into account only regions whose perimeter trespasses the transformed lattice site, unnecessary evaluations can be prevented.

The gauge transformation gets accepted in lines 18 and 19

- if the number of negative projecting non-trivial center regions is increased: $c'_- > c_-$,
- if the gauge functional is increased and no center region got lost: $R'_{\text{MCG}} > R_{\text{MCG}}$ and $c'_- \geq c_-$
- with specific probability (governed by T_{SA}) if the gauge functional decreases but no center region is lost

and is rejected otherwise. An accepted gauge transformation causes the links to get overwritten in line 20 to 22.

If a transformation gets rejected due to lost non-trivial center regions, it is still counted by the variable "Accepted". This ensures that the spread is not reduced without need in lines 28 to 30. If less than 50% of the generated gauge matrices during 10 consecutive trials are rejected due to the gauge functional, the spread is decreased: the gauge matrices are generated less distant from unity in the following runs. After each run T_{SA} is reduced, resulting in a lower acceptance probability for a decrease of the gauge functional: A climb towards a local maximum of the gauge functional is guaranteed. To ensure enough flexibility for the preservation of non-trivial center regions, T_{SA} is multiplied with a factor proportional to the number of wrong projecting non-trivial center regions.

After the gauge fixing procedure the P-plaquettes are identified in the center projected configuration

$$Z_\mu(\vec{x}) := \text{sign}(U_\mu(\vec{x})). \quad (3.4)$$

The P-vortex is built by all plaquettes that are dual to a P-plaquette, that is, the plaquettes that are spanned by the two normal vectors of P-plaquettes.

Within the resulting P-vortex many short range fluctuations that do strongly depend on the gauge can be embedded. They cause unphysical distortions of the vortex surface. For the reconstruction of the thick vortex these distortions can become problematic since they might result in a mistakenly high count of plaquettes related to the thick vortex: as collision handling can not come to use when reconstructing the thick vortex, short range fluctuations can result in a possible double counting of plaquettes. Smoothing the vortex surface is possible without influencing long-range effects and suppresses double counting.

3.2.2 Smoothing the P-vortex surface

The local geometry of the P-vortex is gauge dependent: There are many local maxima of the gauge functional that correspond to slightly different vortex surfaces. The P-vortex fluctuates around the core of the thick vortex. These short range fluctuations are not considered physical and may trouble the measurement of physical observables. To get rid of them and allow for clearer observation of the long range effects, the vortex surface can be smoothed. This is based on cutting out parts of the vortex surface and closing arising holes as shown in Fig.3.9. It is done by multiplying specific links of the center projected

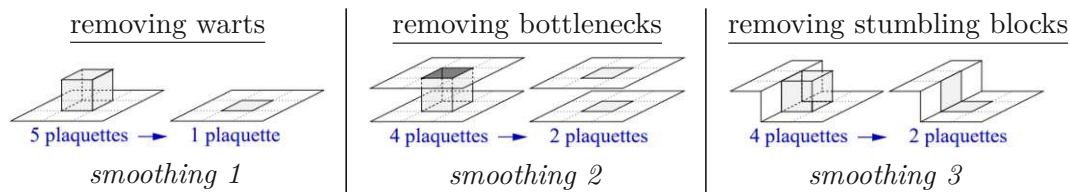


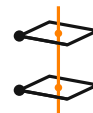
Figure 3.9: The effect of the smoothing procedures on the vortex surface is depicted, taken from [27, Fig.5.8.].

configuration $Z_\mu(x)$ with -1 so that the Dirac volume gets more compact without getting disconnected from the lattice boundary. Thus, the number of P-plaquettes decreases and short range fluctuations are removed from the vortex surface. The different smoothing steps are described in detail in Refs. [28, 27]. In addition to the depicted smoothing procedures there is *smoothing 0* which removes unit cubes and is part of every other smoothing.

Procedures that modify the topology of the vortex surface should be considered with care as they might influence the vortex physics. For example, smoothing 2 disconnects parts from the vortex surface by removing bottlenecks.

To understand the effect of such procedure let us quantify the average smoothness of the vortex surface by looking at P-plaquette pairs:

- P-plaquette pair corresponding to straight flux line:



- P-plaquette pair corresponding to curved flux line:



In Fig. 3.10 the proportion of P-plaquette pairs corresponding to a curved flux line is shown for the different smoothing procedures and numbers of cooling steps. As can be

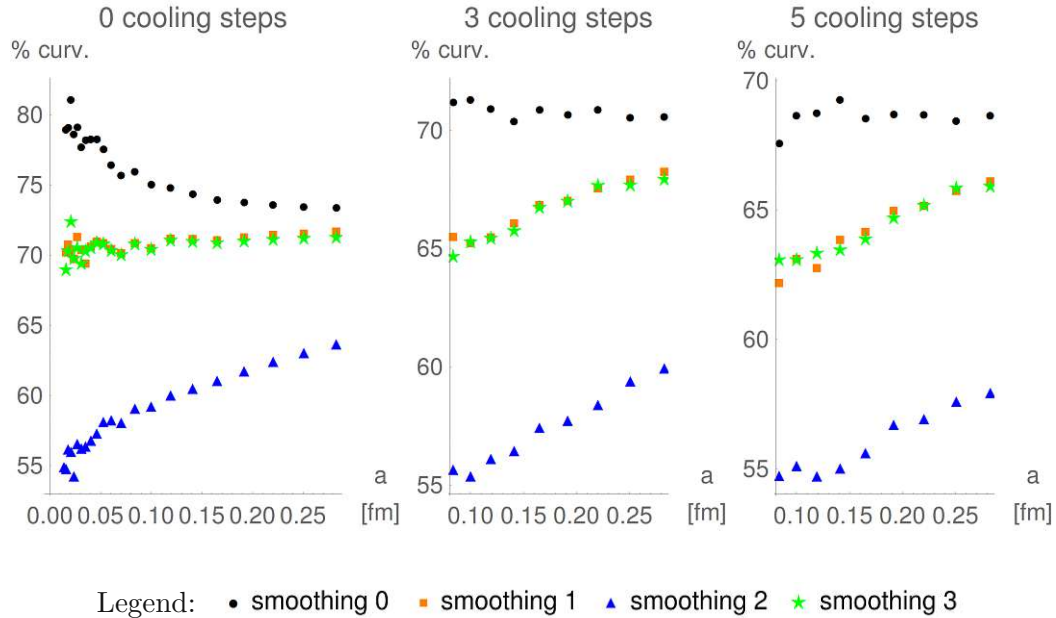


Figure 3.10: The average curvature of the vortex surface can be estimated by the proportion of P-plaquette pairs that correspond to a curved flux line. The data is taken from 10 Wilson configurations on lattices of size 16^4 and compares the different smoothing procedures at different number of cooling steps. The deviation of smoothing 0 and smoothing 2 from linear behaviour at small lattice spacings for 0 cooling steps may be caused by finite size effects and discretization effects.

expected, the smoothing procedures reduce the average curvature of the vortex surface. The difficult question that arises is, how much smoothing can be done without losing relevant physics. Of all listed procedures smoothing 0 has the least possible impact on the vortex surface as it removes only unit cubes that are not connected to the vortex surface whilst smoothing 2 even impacts the topology of the vortex surface.

The increase of the average curvature for smoothing 0 with decreasing lattice spacing when no cooling is applied, may be understood as discretization effect, but could also be caused by finite size effects: With increasing lattice resolution, that is, decreasing pixel size, more and more structure can be observed and with smaller physical lattice volume the vortex surface may get distorted. That smoothing 2 shows opposite behaviour should urge caution: We will see a correlation of curvature to color inhomogeneity. Hence, the strongly reduced average curvature of the vortex surface due to smoothing 2 may come with an impact on the color structure.

3.3 Thick vortices

Thick vortices are gauge independent excitations considered relevant for confinement and chiral symmetry breaking. With given vortex finding property this vortices are located by the P-vortices and can be reconstructed using P-plaquettes as seeds for the enlargement procedure of non-trivial center regions. When reconstructing thick vortices, collisions of the growing non-trivial center regions are ignored to allow overlaps. This is, because thick vortex piercings might be separated by distances below a single lattice spacing. If collisions were prevented, parts of the reconstructed thick vortices may be cut away, resulting in underestimated tracefactors related to piercings of the thick vortex through a given Wilson loop. Pseudo-code of the relevant procedure is shown in algorithm 3.4.

Algorithm 3.4: Reconstruction of thick vortices from P-plaquettes.

Result: List of non-trivial center regions C_R , corresponding to thick vortex piercings

```

1  $S_{pl}$  = stack of P-plaquettes;
2  $C_R$ .clear();
3 while  $S_{pl}.size() > 0$  do
4    $C_R$ .push_back(convertToDoubleConnectedList( $S_{pl}.last()$ ));
5    $S_{pl}.remove\_last()$ ;
6   repeat
7     link bestLink = none;
8     double bestEvaluation = Tr( $C_R$ .last());
9     for each link as  $l$  within  $C_R$ .last() do
10      double newEvaluation = Tr( $C_R$ .last() with  $l$  pushed outwards);
11      if newEvaluation < bestEvaluation then
12        bestEvaluation = newEvaluation;
13        bestLink =  $l$ ;
14      end
15    end
16    if bestLink  $\neq$  none then
17       $C_R$ .last().EnlargeByPushingLinkOutwards(bestLink);
18       $S_{pl}$ .remove(plaquette that got added to the region  $C_R$ .last());
19    end
20  until bestLink == none;
21 end

```

Once this algorithm halted, a list of non-trivial center regions is generated. Each of this center regions can be assumed to be pierced by a thick vortex. If the P-plaquettes taken as seeds correspond to an unsmoothed vortex surface, many overlapping center regions might be generated. This can result in a double counting of plaquettes during the measurement of vortex specific observables. By analyzing the overlaps of the center regions enclosing the thick flux tubes, double counting can also be prevented, but this is

not yet done in our current implementations.

3.4 Achieved improvements and restrictions

To see what improvement is achieved by usage of center regions as guidance in the gauge fixing procedure, we will now compare simulated annealing without guidance to simulated annealing with guidance with respect to measurements of the string tension via Creutz ratios. This allows to estimate the range of lattice parameters in which a successfully vortex detection is possible. As for studies of the chiral properties of center vortices smooth lattice configurations are required, we will also take a first look at the influence of Pisa cooling.

When no center regions are taken as guidance for the gauge fixing procedure, it can be observed, that strong simulated annealing results in an underestimation of the string tension: with rising number of simulated annealing steps the Creutz ratios give lower and lower values for the string tension, whereas with usage of non-trivial center regions as guidance, this loss of the string tension is prevented. In Fig. 3.11 it can be seen that this comes at the cost of increased error bars. The step count is given in multiples of 250. Harsh simulated annealing without taking into account non-trivial

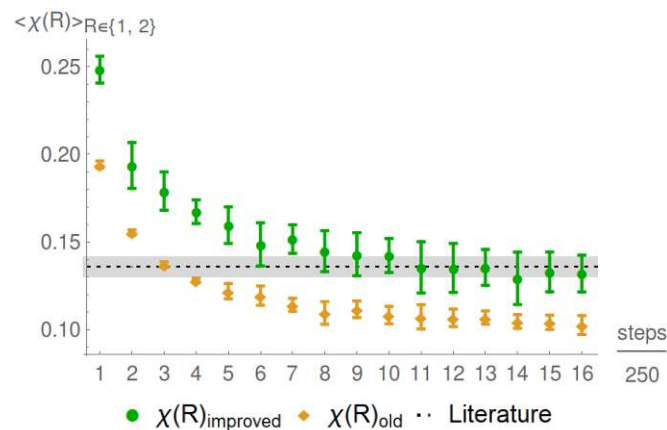


Figure 3.11: With rising number of simulated annealing steps a simulated annealing procedure that does not use non-trivial center regions leads to an underestimation of the string tension ($\chi(R)_{\text{old}}$), while the guided version ($\chi(R)_{\text{improved}}$) stays on literature value after reaching it at 2500 steps. The step count is given in multiples of 250. The data was calculated in a lattice of size 14^4 for $\beta = 2.3$ from 300 $SU(2)$ configurations. The literature value is based on [29].

center regions underestimates the string tension after 750 steps. This loss of the string tension is prevented by taking into account non-trivial center regions and higher numbers of simulated annealing steps become reachable. How fast the gauge fixing procedure converges may depend on the lattice size. On lattices of size 14^4 at least 2500 simulated annealing steps are recommended.

The literature string tension is well reproduced already with Creutz ratios of small loop sizes but the error bars increase faster with rising loop size when using guidance by center regions than without such guidance, see Fig. 3.12. With increased value of β larger loop

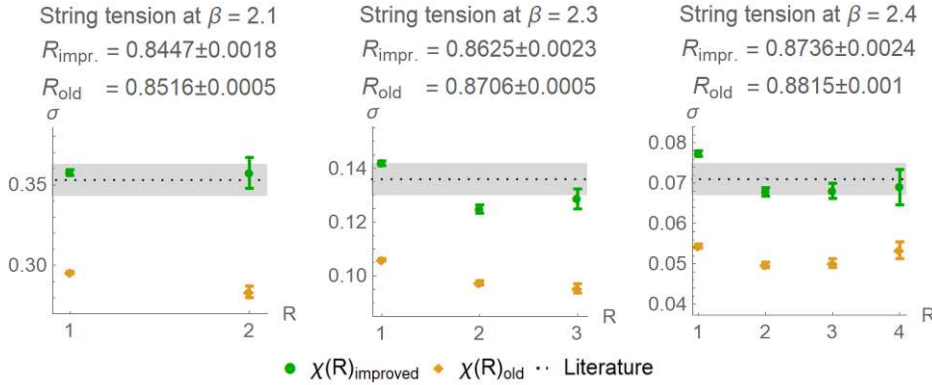


Figure 3.12: We compare the original simulated annealing that is not guided by non-trivial center regions with the guided version after 5000 simulated annealing steps for 300 SU(2) Wilson configurations on lattices of size 12^4 (left), 14^4 (middle) and 12^4 (right) for different values of β . The literature value is based on [29].

sizes become reachable for the Creutz ratios. The good compatibility to the literature string tension is kept over a wide range of β -values, see Fig. 3.13. In the lattice of size 10^4 the string tension is reproduced well up to β -values of 2.7, but finite size effects setting in at β about 2.35 in the smaller lattice of size 8^4 urge caution.

When Pisa cooling is used, a reduction of the observed string tension occurs as can be seen in Fig. 3.14. From the two given lattice sizes it can be seen, that finite size effects lead to a sudden decrease of the observed string tension. Until this sudden decrease the measurements slowly approach the asymptotic prediction with increasing β . Linearly extrapolating this approach to higher values of β allows to estimate at which β the string tension might be restored: With 5 cooling steps a restoration should not be expected with β below approximately 2.45 and for 10 cooling steps not before a β of about 2.8. Reaching these values of β requires larger lattices to prevent finite size effects. A detailed study of finite size and discretization effects will be presented in chapter 4.

These effects hint at a failing vortex detection for small lattice sizes or large values of β . This failing vortex detection can be related to a troubled guidance of the gauge fixing procedure: the simulated annealing maximizing the gauge functional does no longer manage to keep the non-triviality of non-trivial center regions throughout gauge fixing and center projection: There are non-trivial center regions that are not related to a P-plaquette in the center projected configuration, thick vortices got lost.

By taking a look at the ensemble used to calculate the string tension, one can determine the proportion of configurations in which more non-trivial center regions have been identified than P-plaquettes where found. For a successful gauge fixing this proportion

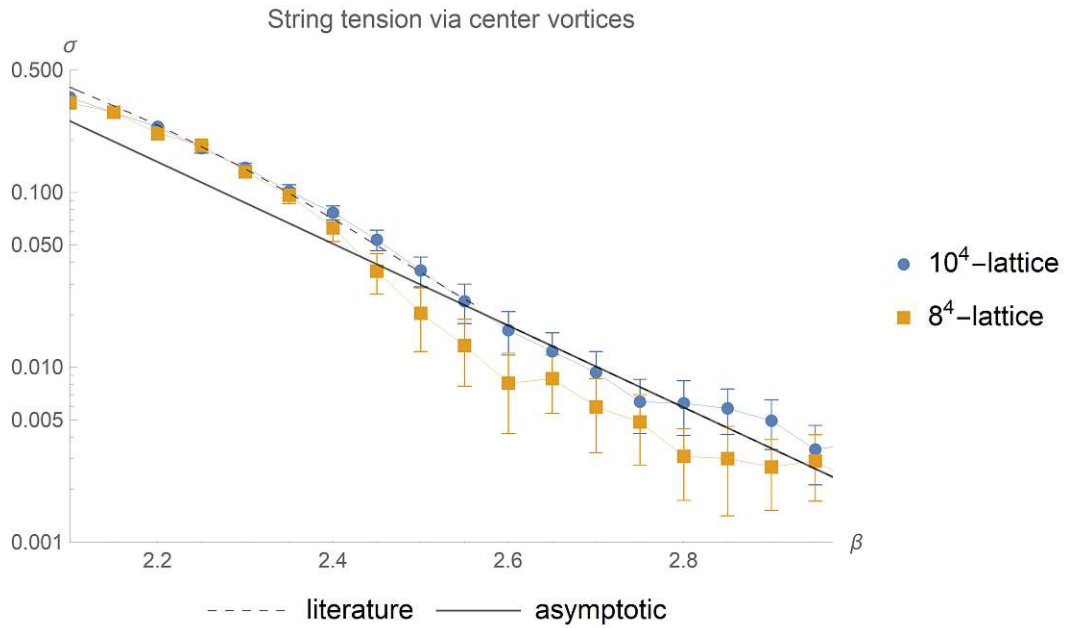


Figure 3.13: The string tension σ is estimated via the average of the Creutz ratios $\chi(1)$ and $\chi(2)$ calculated in center-projected configurations. The literature values are taken from [29, 30, 31, 32, 33] and the asymptotic behaviour is based on a fit of the asymptotic renormalization group equation for $\beta > 2.576$.

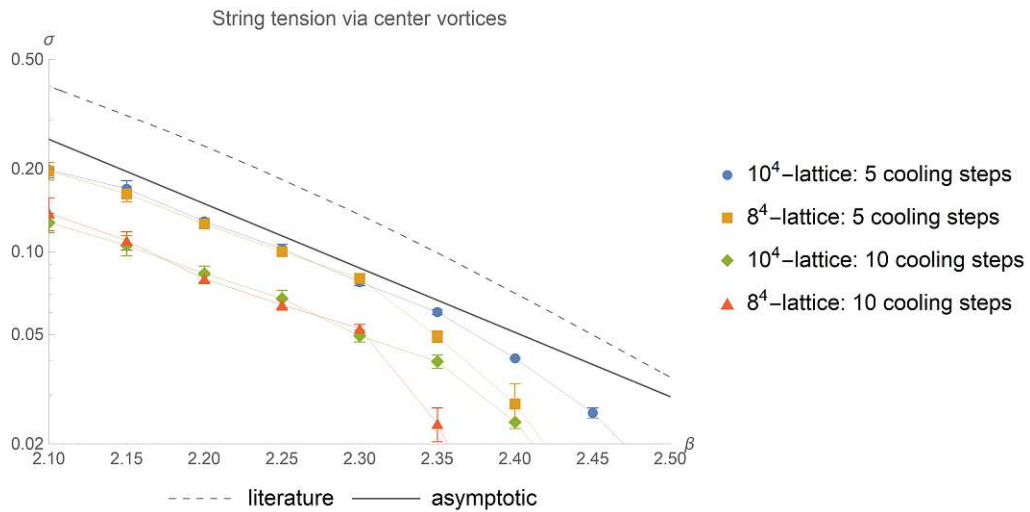


Figure 3.14: The string tension σ is estimated via the average of the Creutz ratios $\chi(1)$ and $\chi(2)$ calculated in center-projected configurations. The literature values are taken from [29, 30, 31, 32, 33] and the asymptotic behaviour is based on a fit of the asymptotic renormalization group equation for $\beta > 2.576$. A clear indication of finite size effects is given by the deviation of the measurements on different sized lattices.

should be vanishing. It is depicted in Fig. 3.15 for different lattice sizes and numbers of cooling steps. That a reduced lattice size shifts the curves to lower values of β is a clear

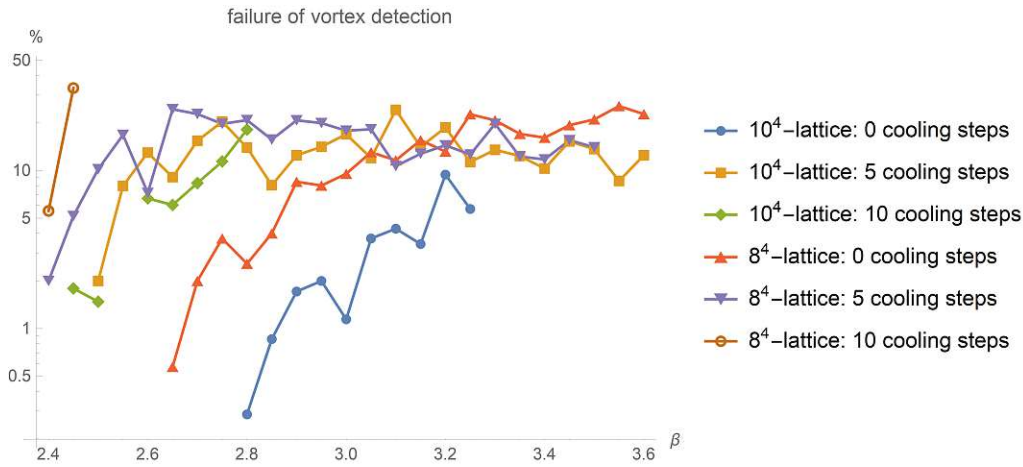


Figure 3.15: The proportion of configurations is depicted where less non-trivial plaquettes have been identified than non-trivial regions exist. The datapoints are joined to guide the eye. Due to the logarithmic scaling of the axes, only non-vanishing values are depicted: all lines start with 0% at lower values of β . The interruption of the green line corresponding to the lattice of size 10^4 at 10 cooling steps at $\beta = 2.55$ results from a vanishing percentage at the respective β -value. Observe that the curves rise at different values of β for different number of cooling steps and different lattice sizes.

indication for finite size effects. Also a dependence on the number of cooling steps can be seen.

Vortex specific properties allow a better understanding of the cause for the finite size and discretization effects and enable a better quantification of the restrictions on the lattice parameters for a successful vortex detection. This will be presented chapter 4.

Algorithmic restrictions from vortex properties

Once the non-trivial center regions that enclose the thick vortices are identified, vortex specific analysis becomes possible. Based on thickness, size and color structure of the vortices, restrictions to the detection algorithms can be derived. This allows to understand the troubles of the original gauge fixing procedure. We will now take a look at the thickness of the vortex surface and relate it via the flux tube diameter to discretization and finite size effects. This will be followed by an analysis of the vortex color structure which will strengthen some of the results that are based on the vortex thickness.

The following sections summarize and complement content already published in [34, 12, 35]

4.1 Thickness and size

Assuming circular cross sections of the vortex flux tubes, their diameter defines the thickness of the vortex. Such a non-vanishing diameter can cause finite size effects: At least two vortex piercings need to find place in each two dimensional slice through the lattice to allow a closed flux. Hence, twice the diameter of a thick flux tube gives a lower limit for the required lattice extent.

Once the P-plaquettes are identified and the thick vortex is reconstructed, non-trivial center regions enclosing the thick vortex piercings can be used to measure the piercing area. Multiplying the plaquette number of the non-trivial center region with the physical size of a plaquette, a^2 , gives an approximation of the piercing area. This approximation gets better with decreased lattice spacing a . During refinement of the lattice a specific scaling behaviour can be expected from geometric arguments: linear for finite objects, non-linear for singular objects. A simplified scheme is given in Fig. 4.1, where measurements of

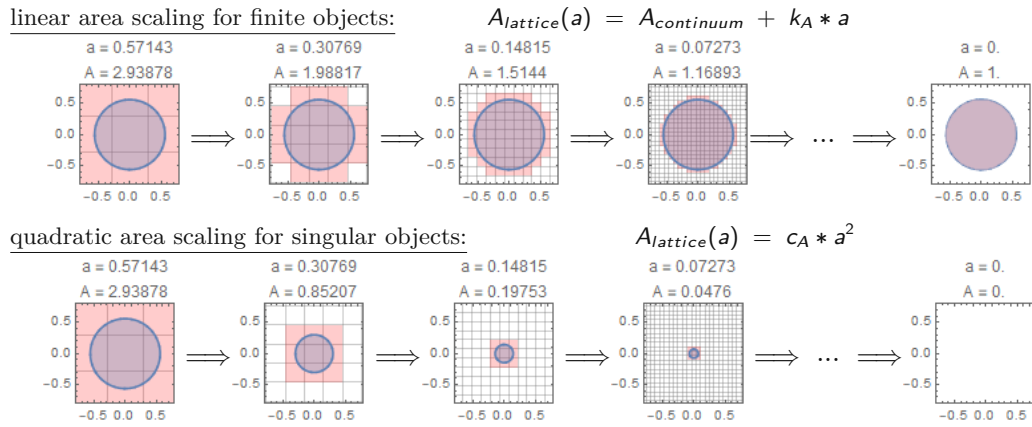


Figure 4.1: Due to the finite pixel size a linear dependence on the lattice constant a is expected, as depicted in the upper part. Objects with cross sections proportional to plaquette areas lead to contributions of the order a^2 , as is depicted in the lower part.

circular areas based on counting plaquettes are shown for varying lattice spacings.

In Fig. 4.2 measurements of the average flux tube cross sections are shown as a plaquette number in dependence of β for different lattice sizes and cooling steps. Observe that until 10 cooling steps the dependence of the plaquette count on β can be well approximated linearly. Thresholds at which finite size effects can be expected are shown as dashed

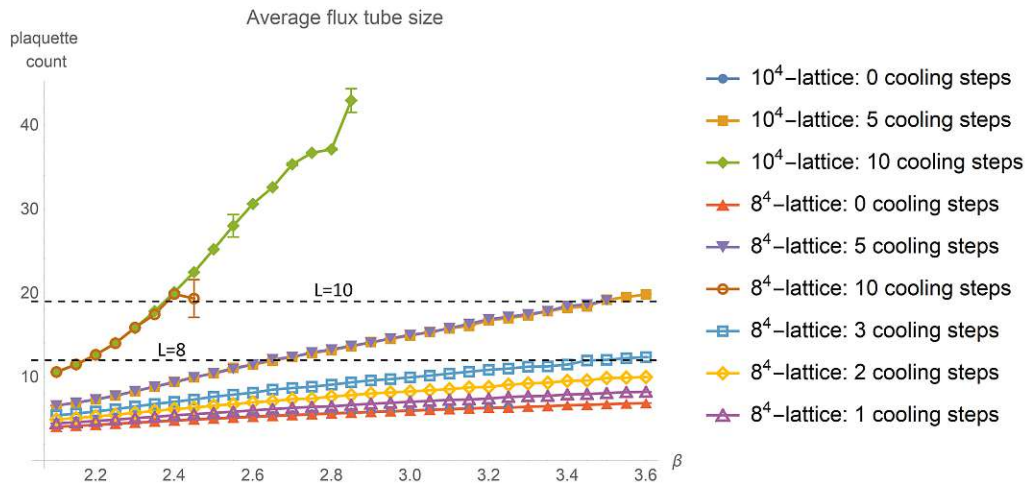


Figure 4.2: Average cross-sections of flux tubes, measured by counting plaquettes, increase when cooling is applied. They reach a threshold at which finite size effects are expected to become problematic, shown as a dashed line for the two lattice sizes. This threshold is based on the assumption of circular cross sections. Measurements performed on lattices of different size have good compatibility.

lines for the two different lattice sizes. They are determined by assuming a circular cross section of the flux tube and demanding that two piercings need to fit into a 2-dimensional

lattice slice:

$$\text{threshold} = \frac{L^2 * \pi}{16}, \quad (4.1)$$

with lattice extent L . The lattice extent should be chosen so that the cross section of the flux tube is below the threshold.

Taking a look not at the average flux tube cross sections but the maximal cross section per configuration of the ensemble used for the calculations, more strict limits arise. Measurements of these maximal cross sections are shown in Fig. 4.3. Observe the

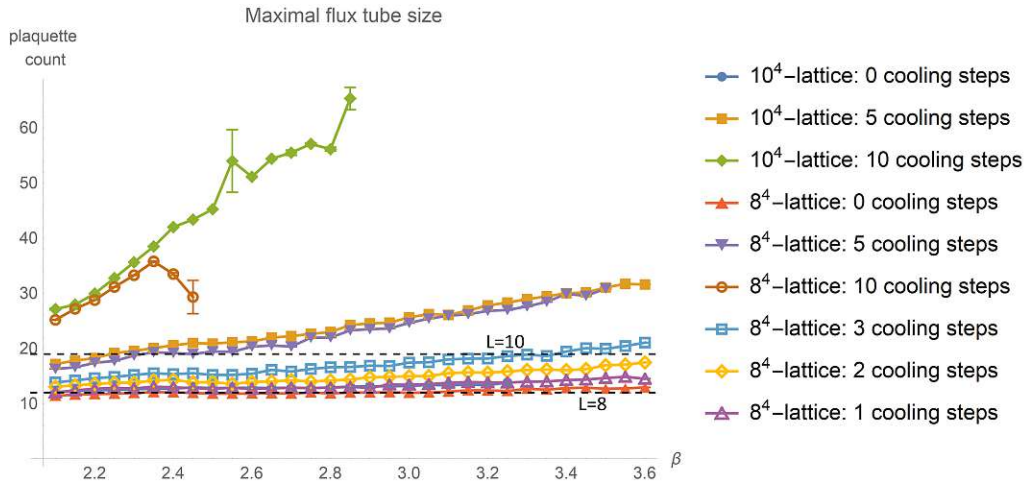


Figure 4.3: Maximal cross-sections of the flux tubes hint at finite size effects. Within our β -interval, only the lattice of size 10^4 stays below the threshold when cooling is applied. With cooling, the different lattice sizes become more and more incompatible.

increased plaquette count and the surpassed thresholds especially with larger number of cooling steps. With 10 cooling steps the 8^4 -lattice deviates from the 10^4 -lattice at $\beta \approx 2.4$. This deviation is caused by the diameter of the cross section becoming comparable to the lattice extent.

It can be clearly seen that the flux tubes expand with cooling. As the flux tube is identified by a non-trivial center region enclosing the flux tube piercing, this expansion can be related to the center element spreading over more and more links of a Wilson loop enclosing the flux tube. As long as the center element is located on a sufficiently low number of links, center projection can identify corresponding P-plaquettes. If the center element is distributed over too many links and the gauge transformation does not manage to compress it, then no P-plaquette that corresponds to the piercing of the thick vortex can be identified: The vortex finding property can get lost due to the expansion of the flux tubes. The guidance of the gauge fixing procedure by non-trivial center regions can counteract this loss up to a specific degree. We will now go from lattice units to physical units and derive formulas for limits on the lattice parameters in dependence of the cooling steps. This also limits the number of cooling steps that can be performed before a loss of the vortex finding property occurs.

Fitting the average flux tube cross-sections for configurations without cooling for $2.1 \leq \beta \leq 2.3$ by a polynomial up to quadratic order with respect to the lattice spacing a gives

$$A_{\text{vort}}^{\text{average}}(0) \approx 3.367(38) a^2 + 0.200(9) \text{ fm } a \quad (4.2)$$

and a fit to the maximal cross-sections without cooling for $2.1 \leq \beta \leq 2.3$ results in higher fit parameters

$$A_{\text{vort}}^{\text{max}}(0) \approx 11.3(2) a^2 + 0.224(37) \text{ fm } a, \quad (4.3)$$

where the parameter zero corresponds to the number of cooling steps. In both cases the quadratic term of the polynomial dominates and a constant term was negligible. Keep in mind the scaling behaviour depicted in Fig. 4.1. The dependence of the cross section on the number of cooling steps can be roughly modelled as

$$A_{\text{vort}}^i(N_{\text{cool}}) = A_{\text{vort}}^i(0) e^{N_{\text{cool}} (g_{\text{cool}}^i + g_{\text{discret}}^i a)}, \quad (4.4)$$

with $i \in \{\text{average, max}\}$ and N_{cool} the number of cooling steps: An exponential growth of the flux tube with cooling is assumed and discretization effects bring about a dependence on the lattice spacing a .

An unlimited growth of the flux tube would push the flux tubes further and further apart with cooling. This in turn would result in a vanishing vortex density that will be modelled later. One can expect that the exponential growth hits a limit that is not covered by this simple model. We will see hints at this limited growth in the values of the fit parameters and also later when the color structure of the vortex is discussed.

We first apply this model to the average flux tube sizes. The data is presented in physical units together with a fit of Eq. (4.4) in Fig. 4.4. The fit parameters are shown in Table 4.1. Observe that the discretization effects governed by g_{discrete}^i in Eq. (4.4) counteract the growth of the flux tube. This can be intuitively understood by looking again at

fit parameter	Estimate	t-Statistic	p-Value
$g_{\text{cool}}^{\text{average}}$	0.14(1)	13.6393	6.3×10^{-11}
$g_{\text{discret}}^{\text{average}}$	$-0.17(5) \text{ fm}^{-1}$	-3.62376	1.9×10^{-3}

Table 4.1: The parameters of the model described by Equation (4.4) and depicted in Figure 4.4 for average cross-sections are shown.

Fig. 4.1: On the leftmost side of the figure we see a large pixel size. A small expansion of the circle does not increase the measured area. In contrast, on the right side of the figure, a growth of the piercing directly results in more pixels covered by the area.

Looking now at the maximal sized flux tubes we observe that the growth slows down, see Fig. 4.5 and the corresponding fit parameters presented in Table 4.2: The absolute values of the parameters decrease when looking at bigger piercing areas. Hence, the model may overestimate the growth of the flux tube caused by cooling. Equations (4.1) and (4.4) in combination with the fit parameters in table 4.1 or table 4.2 result in the first limit

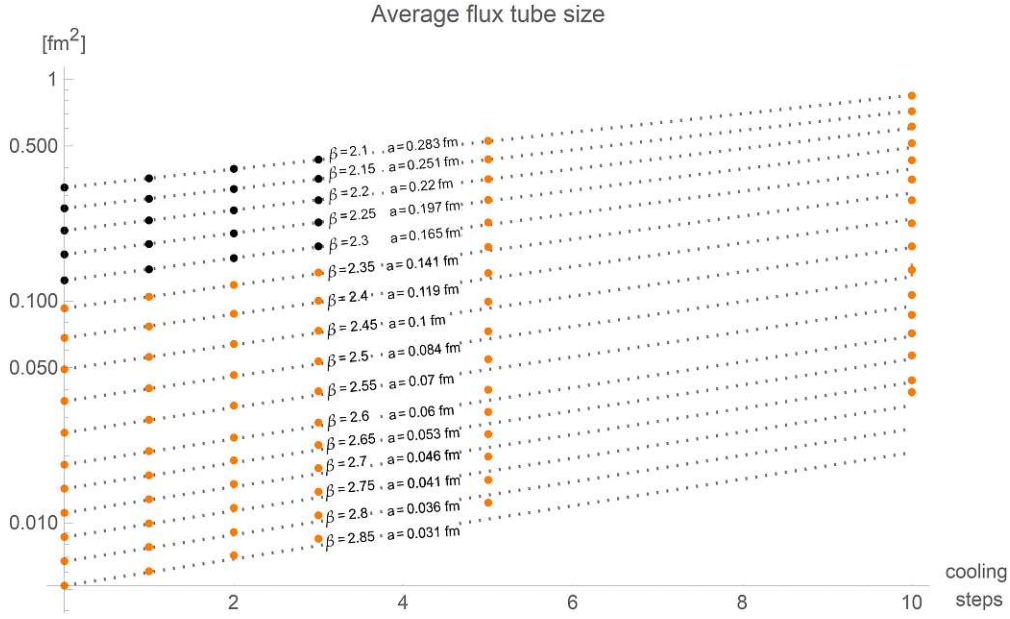


Figure 4.4: The measured data of the average flux tube cross-section for various numbers of cooling steps and several β are shown by black and orange points. The dashed lines depict the fits according to Eq. (4.4), where only the black datapoints were used. The corresponding fit parameters are given in Table 4.1. Deviations of the data from the fits can be related to finite size effects.

fit parameter	Estimate	t-Statistic	p-Value
$g_{\text{cool}}^{\text{max}}$	0.0999(10)	9.1369	3.5×10^{-8}
$g_{\text{discret}}^{\text{max}}$	$-0.13(5) \text{ fm}^{-1}$	-2.61939	1.7×10^{-2}

Table 4.2: The parameters of the model described by Equation (4.4) and depicted in Figure 4.5 for maximal cross-sections are shown.

of the lattice parameters: a lower limit on the lattice extent or an upper limit on β if the lattice size is fixed. Also the number of cooling steps is limited by these equations. In addition to these restrictions we will now take a look at discretization effects that result from neighbouring flux tubes coming too close to one another. From this, opposite limits, an upper limit for β or a lower limit for the lattice extent, can be derived. Thus, a window of valid lattice parameters and cooling numbers is given. To determine this window we investigate the vortex density ϱ_{vort} .

ϱ_{vort} is usually calculated by dividing the number of P-plaquettes by the total plaquette number. It is related to the string tension via

$$\sigma \approx -\ln(1 - 2 * \varrho_{\text{vort}}) \quad (4.5)$$

as long as all short range fluctuations have been smoothed out of the vortex surface. Given enough statistics, it can be determined by counting the number of piercings N_{vort}

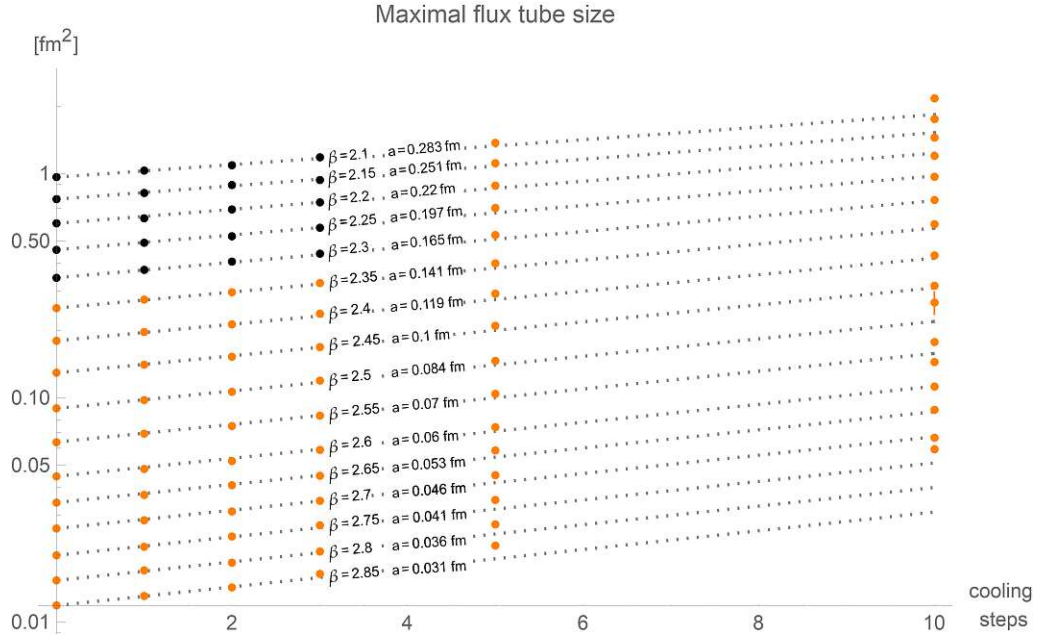


Figure 4.5: The measured data of the maximal flux tube cross-section for various numbers of cooling steps and several β are shown by black and orange points. The dashed lines depict the fits according to Eq. (4.4), where only the black datapoints were used. The corresponding fit parameters are given in Table 4.2. The deviations of the measured data from the fits can be explained by finite size effects.

within a sufficiently large Wilson loop of Area A_{loop} built by N_{loop} plaquettes

$$\varrho_{\text{vort}} = \frac{N_{\text{vort}}}{N_{\text{loop}}} = \frac{N_{\text{vort}}}{A_{\text{loop}} * a^{-2}} = \frac{N_{\text{vort}}}{(A_{\text{free}} + N_{\text{vort}} * A_{\text{max}}) * a^{-2}}. \quad (4.6)$$

In the last identity, we have split the area of the loop into two non-overlapping parts: each piercing is enclosed by a circular area of maximal possible size given by A_{max} and A_{free} covers the remaining part of the loop, see Fig. 4.6. We want to stress that A_{max} is not the area of the piercing, but related to the average distance between the centers of piercings. It can be seen as the "private space" each piercing is allowed to cover. When cooling is applied, we have to take into account that the flux tubes grow and A_{max} might be influenced: if the flux tubes push one another apart, they acquire more "private space". The same holds true if some piercings get deleted. Thus, we model the influence of cooling on the vortex density by allowing A_{max} to grow:

$$\varrho_{\text{vort}}(N_{\text{cool}}) = \frac{N_{\text{vort}}}{(A_{\text{free}} + N_{\text{vort}} * (A_{\text{max}}(0) + \delta A_{\text{max}}(N_{\text{cool}}))) * a^{-2}}. \quad (4.7)$$

Using $A_{\text{loop}} = A_{\text{free}} + N_{\text{vort}} * A_{\text{max}}(0)$ and a model of the form given in Equation (4.4) for $A_{\text{max}}(N_{\text{cool}})$ we attain $\delta A_{\text{max}} = A_{\text{max}}(0)(e^{N_{\text{cool}}(\mathcal{G}_{\text{cool}} + \mathcal{G}_{\text{discrete}} a)} - 1)$. It follows

$$\varrho_{\text{vort}}(N_{\text{cool}}) = \frac{\varrho_{\text{vort}}(0)}{1 + \varrho_{\text{vort}}(0) A_{\text{max}}(0) a^{-2} (e^{N_{\text{cool}}(\mathcal{G}_{\text{cool}} + \mathcal{G}_{\text{discrete}} a)} - 1)}. \quad (4.8)$$

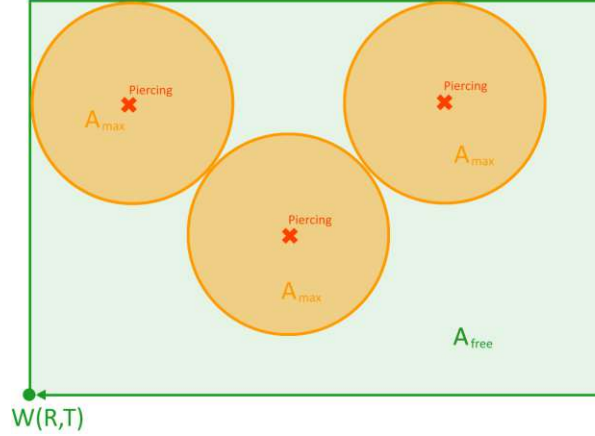


Figure 4.6: Splitting the area of a Wilson loop into disks around piercings with area A_{\max} and remaining loop area A_{free} allows to estimate the separation of neighbouring piercings.

It can be assumed that cooling reduces short range fluctuations of the vortex surface, resembling a vortex smoothing that reduces the vortex density. Hence, a reduction of the vortex density is not necessarily unwanted since only the long range effects are of relevance and it can be advantageous to get rid of the short range fluctuations.

We fit g_{cool} , g_{discrete} and $A_{\max}(0)$ to the measurements of ϱ_{vort} . Due to the smoothing effect of cooling these parameters may be less disturbed by short range fluctuations and allow another quantification of the long range flux tube growth. The measured data and the fit are shown in Figure 4.7. Observe the even lower value of g_{cool} . It hints again at a limited growth of the flux tubes. The value of $A_{\max}(0)$ is larger than the flux tube

fit parameter	Estimate	t-Statistic	p-Value
g_{cool}	0.035(1)	26.5368	2.8×10^{-15}
g_{discret}	0.066(2) fm ⁻¹	27.6254 fm ⁻¹	1.5×10^{-15}
$A_{\max}(0)$	1.41(5) fm ²	25.8937 fm ²	4.2×10^{-15}

Table 4.3: The parameters of the model described by Equation (4.8) showing the loss of the vortex density during cooling.

cross-sections depicted in Figure 4.4. Assuming circular geometry, we can calculate the minimal possible distance between vortex centers

$$d_{\text{center}}(N_{\text{cool}}) = 2\sqrt{\frac{A_{\max}(N_{\text{cool}})}{\pi}}. \quad (4.9)$$

To determine how many cooling steps are possible, we need to know how much the vortices can grow by cooling without getting into conflict with one another. We estimate

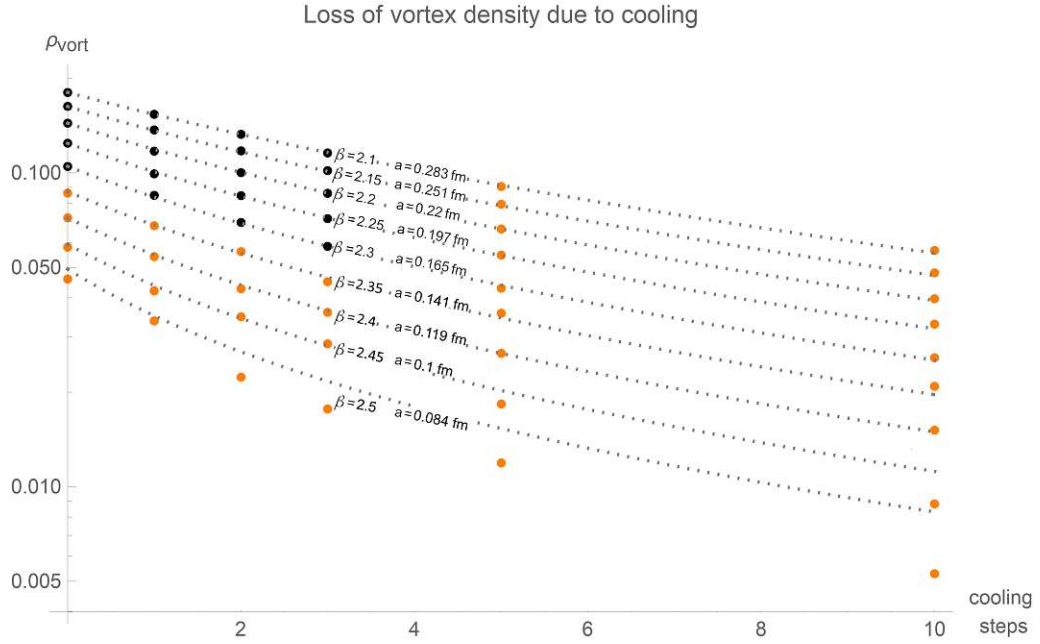


Figure 4.7: The vortex density is depicted for different values of β and different numbers of cooling steps. For the model prediction, shown as dashed lines, only the black datapoints were used. That the datapoints fall below the model prediction at specific numbers of cooling steps for different values of β can be explained by finite size effects. The corresponding parameters of the model are given in Table 4.3.

the minimal available separation by

$$s_{\text{flux}}(N_{\text{cool}}) = 2 \underbrace{\sqrt{\frac{A_{\text{max}}(0)}{\pi}}}_{d_{\text{center}}(0)} - 2 \underbrace{\sqrt{\frac{A_{\text{vort}}(N_{\text{cool}})}{\pi}}}_{d_{\text{flux}}(N_{\text{cool}})}. \quad (4.10)$$

We use $d_{\text{center}}(0)$, the average distance between piercings when no loss of the vortex density occurred, and subtract the average diameter of the flux tubes $d_{\text{flux}}(N_{\text{cool}})$ with cooling applied. If $s_{\text{flux}}(N_{\text{cool}})$ becomes smaller than one lattice spacing, our methods of center vortex detection are likely to fail: we can no longer find two non-overlapping non-trivial center regions enclosing the thick vortex flux tubes. This allows to derive a limit for the lattice spacing and a limit for L based on Eq. (4.1)

$$a < s_{\text{flux}} \quad \text{and} \quad L > \text{Max}(2\overline{d_{\text{flux}}}, \text{Max}(d_{\text{flux}})). \quad (4.11)$$

The requirement for the lattice extent L is based on the fact that two vortex piercings have to fit in every lattice cross-section. Assuming a vanishing minimal flux tube size, the limit is given either by two times the average diameter $\overline{d_{\text{flux}}}$ or one times the maximal diameter $\text{Max}(d_{\text{flux}})$ - whatever is bigger.

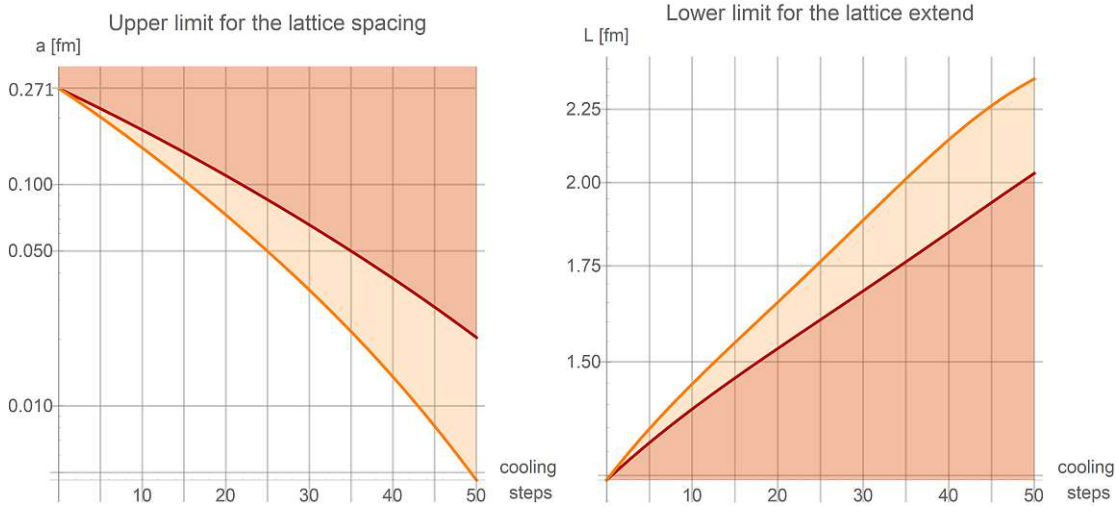


Figure 4.8: Based on the growth of the flux tubes and the reduction in the vortex density in dependence of the number of cooling steps, an upper limit for the lattice spacing (left) and a lower limit for the lattice extent (right) can be derived. The stronger limit depicted in orange is based on cautious calculations potentially overestimating the flux tubes cross-section, the red limit in contrast may come from underestimated cross-sections.

The limits are shown in Figure 4.8 for the two different values of g_{cool} resulting from average and maximal flux tube sizes from Tables 4.1 and 4.2.

Taking the stronger limits with $g_{\text{cool}} = 0.14$, we determine the corresponding limits of β for given lattice size and number of cooling steps. In Table 4.4 some numerical values are shown.

These limits restrict β to quite low values and very small windows. As long as the lattice parameters are kept within this window, specific finite size effects and discretization effects can be excluded, but this alone does not guarantee that the asymptotic string tension is well reproduced. We observe that within this window the measured string tension approaches the asymptotic value with increased β until the onset of the finite size effects. In Fig. 3.14 this was shown for 5 and 10 cooling steps. From the two given lattice sizes it can be seen that finite size effects lead to a sudden decrease of the observed string tension, but until this sudden decrease the measurements slowly approach the asymptotic prediction. A full recovery of the string tension should not be expected at β -values below 2.45 for 5 cooling steps and not before 2.8 for 10 cooling steps. Reaching these β -values without suffering from finite size effects requires larger lattices.

Table 4.4: For different numbers of cooling steps and different lattice extents, the table gives a lower and an upper limit for β based on the more cautious estimates of the cross-section of vortex piercings. “None” indicates that the limits exclude one another.

$N_{\text{cool}} \setminus L$	8	10	14	20	30	40	50
0	2.12	2.12	2.12	2.12	2.12	2.12	2.12
	2.32	2.39	2.48	2.58	2.73	2.84	2.92
1	2.14	2.14	2.14	2.14	2.14	2.14	2.14
	2.31	2.38	2.48	2.58	2.73	2.83	2.91
2	2.16	2.16	2.16	2.16	2.16	2.16	2.16
	2.31	2.38	2.47	2.58	2.72	2.83	2.91
3	2.19	2.19	2.19	2.19	2.19	2.19	2.19
	2.3	2.37	2.47	2.57	2.71	2.82	2.9
5	2.23	2.23	2.23	2.23	2.23	2.23	2.23
	2.29	2.36	2.46	2.56	2.7	2.81	2.89
10	None	2.34	2.34	2.34	2.34	2.34	2.34
		2.34	2.44	2.54	2.67	2.78	2.86
15	None	None	None	2.44	2.44	2.44	2.44
				2.52	2.65	2.76	2.84
20	None	None	None	None	2.54	2.54	2.54
					2.63	2.73	2.82
25	None	None	None	None	None	2.66	2.66
						2.71	2.79

4.2 Color structure

As the color structure of the vortex may be related to its topological charge, we require that it is preserved during the vortex detection procedure. We use the S2-homogeneity based on two plaquettes as defined in Eq. (2.18) to probe this color structure. In dependence of the orientation of these plaquettes and whether or not they are pierced or part of a non-trivial center region we distinguish the following scenarios:

- Planar homogeneities

- Flux tube interior:



Measures, if color structure is present in the cross sections of a vortex flux tube.

- Flux tube edge:



Measures, how sharply a vortex flux tube is separated from the surrounding vacuum with respect to color.

- Longitudinal homogeneities

- Straight flux line:



Measures, if color structure is present along a vortex flux line, that is, on the vortex surface.

- Curved flux line:



In combination with the previous measurement, this allows to quantify the correlation of curvature to color homogeneity.

The two plaquettes that are used to calculate the S2-homogeneity are colored in green and purple as in Fig. 2.96 and the vortex flux line or the flux tube cross section are shown in orange. For the longitudinal homogeneities only the flux lines identified via P-plaquettes are considered, for the planar homogeneities non-trivial center regions corresponding to the cross sections of thick flux tubes are taken into account. In addition to these four scenarios we also performed measurements restricted to non-pierced plaquettes, that is, off the vortex, and also without any restrictions, that is, for the full vacuum.

We find deviations of the respective color-homogeneities from those of the full vacuum as can be seen in Fig. 4.9: The color within the cross-section of a flux tube is more homogeneous than the surrounding vacuum from which it is separated. This separation is indicated by the reduced color homogeneity of the flux tubes edge compared to the vacuum. Along the flux line the color fluctuates stronger than in the surrounding vacuum if the flux line has non-vanishing curvature, that is, color inhomogeneity correlates to curvature of the vortex surface. Observe that the homogeneity of the straight flux lines deviates more from the vacuum than those of the curved flux lines.

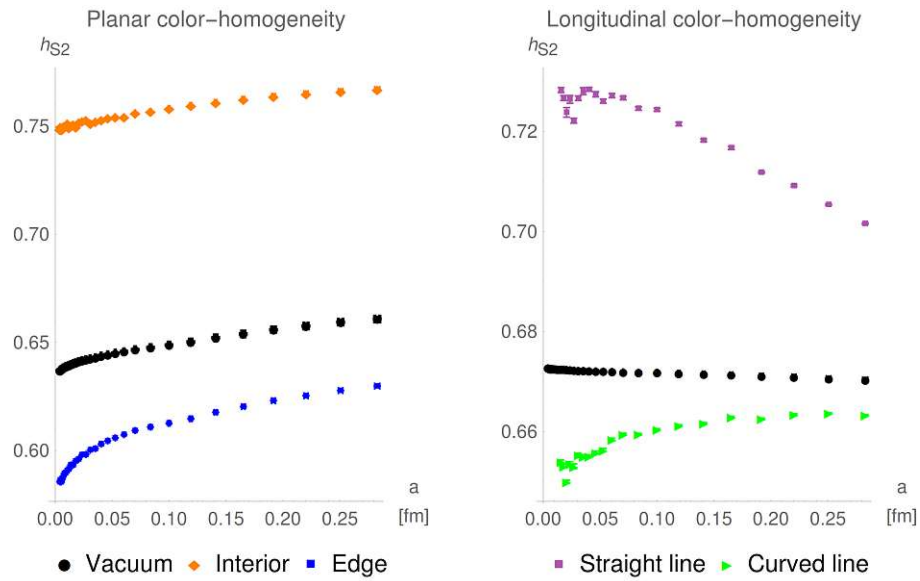


Figure 4.9: The data is taken from 350 Wilson configurations on lattices of size 8^4 with smoothing 0 applied. The black line depicts the vacuum values for the respective measurements. On the left side it can be seen, that the interior of a flux tubes cross sections is more homogeneous than the surrounding vacuum and that the color fluctuates when entering the cross section. On the right side it can be seen that the color fluctuates more strongly along a curved flux line than along a straight flux line. In both graphs, the reduction in homogeneity at low lattice spacings is related to finite size effects.

This correlation urges caution when using smoothing procedures: Vortex smoothing as well as cooling can have an influence on the curvature of the vortex surface and this may influence potential color structure. The vortex structure as well as writhing- and intersection-points of vortices are related to topological charge, see References [36, 37]. To study the topological properties of center vortices in smooth configurations one needs to ensure that no relevant color structure is lost. Looking at the influence of cooling and smoothing procedures, we see that the correlation of curvature to color inhomogeneity not only survives cooling, but even increases with rising number of cooling steps.

In Fig. 4.10 the difference in color-homogeneity for straight and curved flux lines is shown for different number of cooling steps and different vortex smoothings. Observe that cooling increases not only the overall homogeneity but also the differences between straight and curved flux lines. This correlation of curvature and inhomogeneity is less dominant for smoothing 2.

To determine which potential restriction for the vortex detection arise from the color structure, we will look for finite size effects within the total color-homogeneity along the flux line. This approach was already published in [12].

Finite size effects result in a decrease of this color homogeneity, see Fig. 4.11. This decrease indicates that structures causing homogeneity are lost due to the finite sized

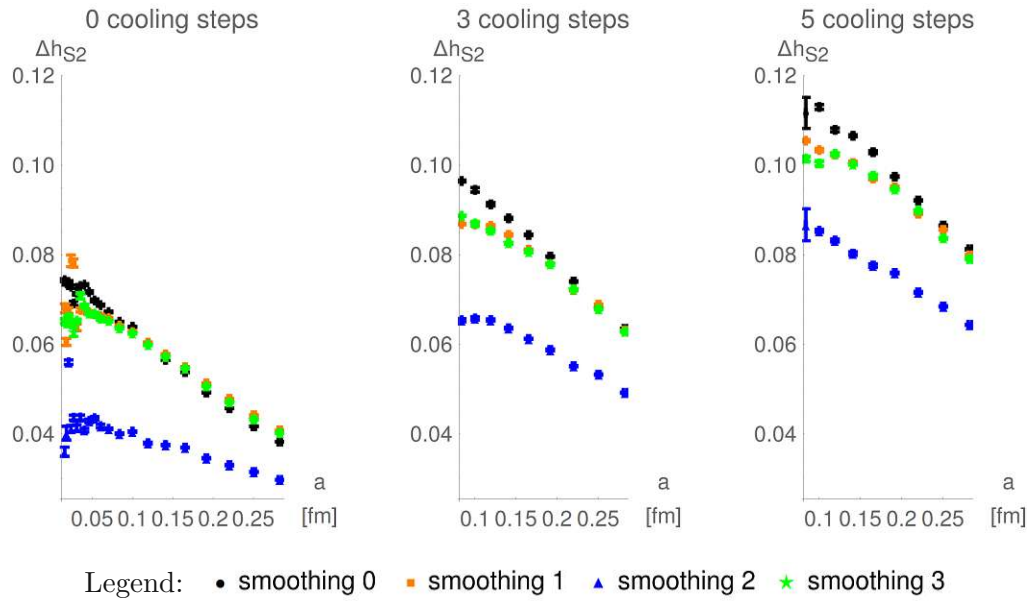


Figure 4.10: The differences in homogeneity between straight and curved flux lines are measured from 10 Wilson configurations on lattices of size 16^4 . Observe that for smoothing 2 the difference between straight and curved flux lines is reduced compared to the other procedures. Cooling increases the overall differences.

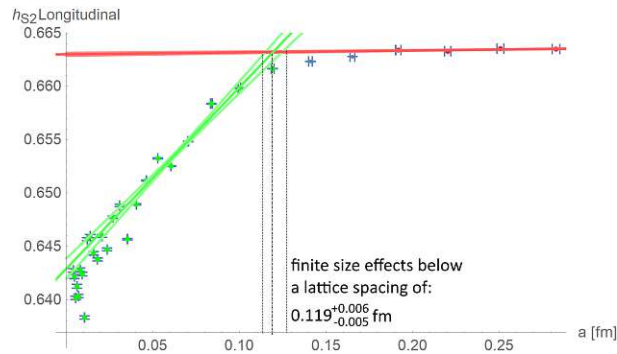


Figure 4.11: Taken from [12], the S2-Homogeneity on the vortex surface is shown for an 8^4 -lattice for different lattice spacings. The data points, used for the fit of the upper (nearly horizontal) red line are marked in red. The green line at small values of the lattice spacing a is fit to the green data points. The allocation of the data points to the lines is based on minimizing the sum of horizontal and vertical squared deviations. For both lines a mean prediction band is calculated and the respective intersections define the lattice spacing below which finite size effects dominate. Multiplying this lattice spacing with the lattice size gives the physical size of the homogeneous regions.

lattice. We refer to these structures as *color homogeneous regions* and use the finite size effects to determine their size. The onset of finite size effects is identified by fitting two lines to the curve and looking for their intersection. The mean prediction bands of these

fits are used to quantify the error. Multiplying the lattice spacing in physical units at which the finite size effects set in with the lattice extent gives a rough estimate of the size of the homogeneous regions in physical units. For physical objects the size has to be independent of the lattice size. This allows to collect more statistics by repeating the measurements in different sized lattices.

The homogeneities along the vortex surface for the different smoothing procedures without applied cooling are shown in Fig. 4.12. Observe the similarity of smoothing 1

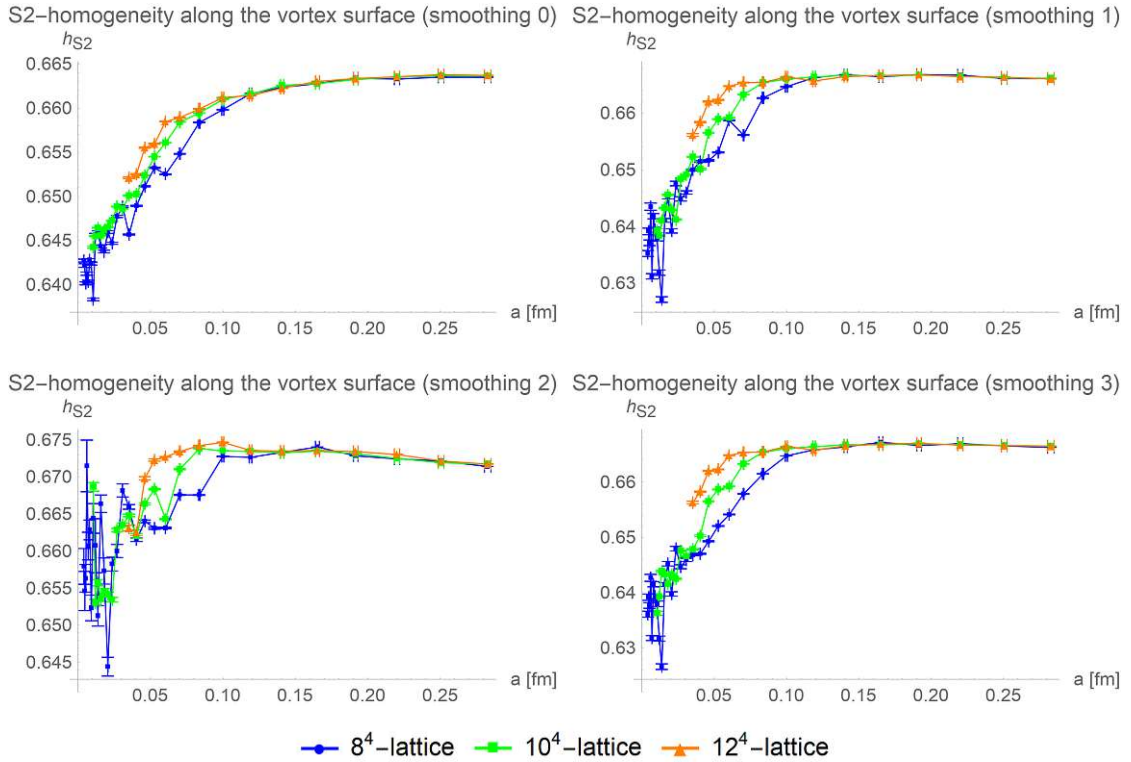


Figure 4.12: Averaged over 100 configurations, the S2-homogeneity along the vortex surface is compared for different lattice sizes and smoothing procedures. With increasing lattice size the curves shift to smaller lattice spacing indicating finite size effects.

and smoothing 3: both saturate faster towards a constant value than smoothing 0 does. In contrast to that, smoothing 2 does not approach a constant but decreases linearly with increasing lattice spacing. The estimations for the size of homogeneous regions are shown in Fig. 4.13. The bigger the lattice gets, the smaller the lattice spacing needs to be to allow identification of the onset of finite size effects. The high values of β that are required to reach such low values of the lattice spacing may be problematic: the correct scaling behaviour can not be guaranteed and the determination of the physical value comes with a large error. Hence the measurements on the 12^4 -lattice might be flawed. We also do not consider the data from smoothing 2 trustworthy. Despite that,

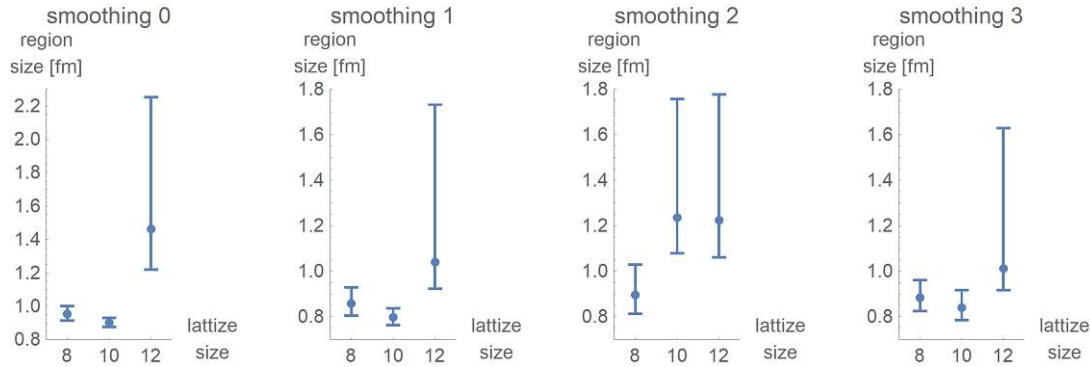


Figure 4.13: The estimation of the size of color-homogeneous regions on the vortex surface is done by fitting two lines to the data, see Fig. 4.11. The asymmetric errors are calculated via the mean prediction bands of the respective fits.

the high values for the size of the homogeneous regions resulting from smoothing 2 and the 12^4 -lattice may hint at an underestimation of the size of homogeneous regions. Thus, we advice to keep the physical lattice extent above approximately 2.3 fm.

We will now look at the influence of cooling to see if even larger lattices are required when cooling is applied. The estimate of the size of homogeneous regions is repeated for different numbers of cooling steps. We only perform the determination with the lattices of size 8^4 and the 10^4 . As the deviation from the vacuum might be relevant for the color structure, we also show the vacuum values.

The measurements after 1 cooling step are shown in Fig. 4.14. Observe that smoothing 2, in contrast to all other smoothings, results in the homogeneity along the vortex surface to be higher than those of the vacuum. The corresponding sizes of the homogeneous regions are shown in Fig. 4.15. With a single cooling step no significant increase of the sizes is seen, but this will change with increased number of cooling steps.

After 2 cooling steps only smoothing 0 results in a homogeneity along the vortex surface below those of the vacuum, see Fig. 4.16. At small lattice spacings the homogeneities after smoothing 2 fluctuate more strongly than they do for the other smoothings. The error bars of the size determination increase, see Fig. 4.17. The strong fluctuations at small lattice spacings trouble the line fit procedures that are used to determine the onset of the finite size effects. Despite that, an overall increase of the size of homogeneous regions can be observed.

After 3 cooling steps no smoothing procedure results in a color homogeneity of the vortex surface clearly below those of the vacuum. With increasing lattice spacing the homogeneities along the surface seem to approach those of the vacuum. No further significant growth of the regions sizes can be seen due to the large error bars, see Fig. 4.15.

After 5 cooling steps each smoothing procedure results in homogeneities along the vortex

4. ALGORITHMIC RESTRICTIONS FROM VORTEX PROPERTIES

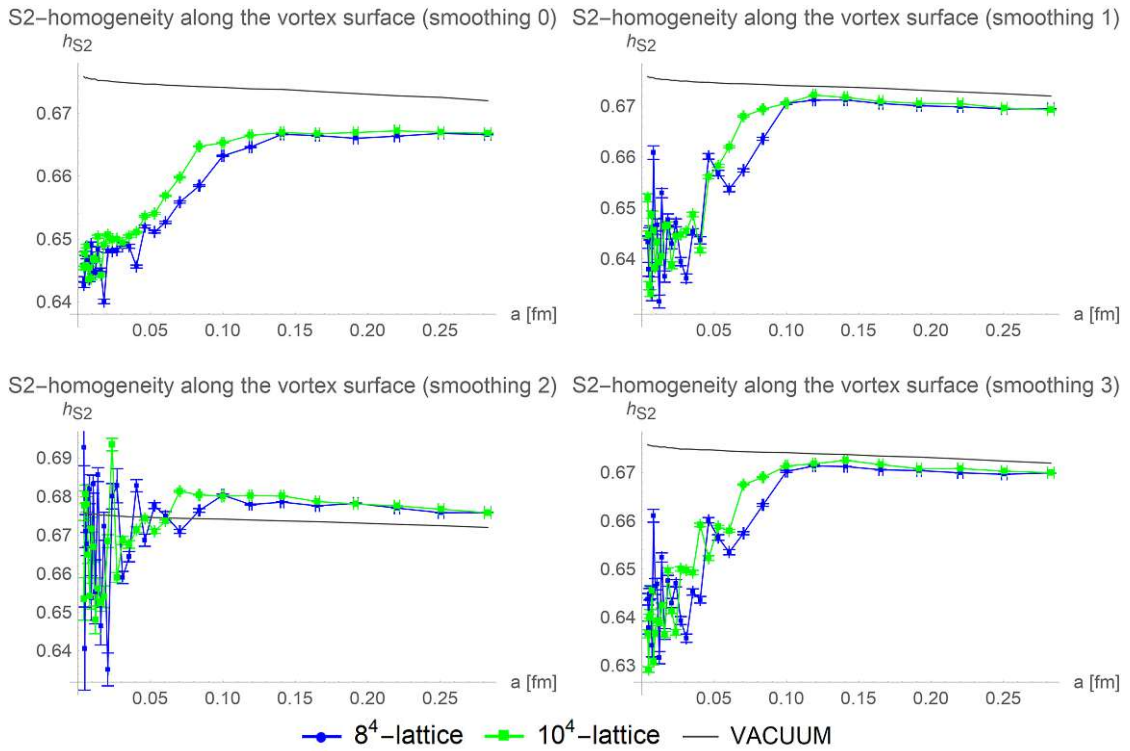


Figure 4.14: Averaged over 100 configurations, the S2-homogeneity along the vortex surface is compared for different lattice sizes and smoothing procedures after 1 cooling step. Observe that cooling increases the overall homogeneity on the vortex surface.

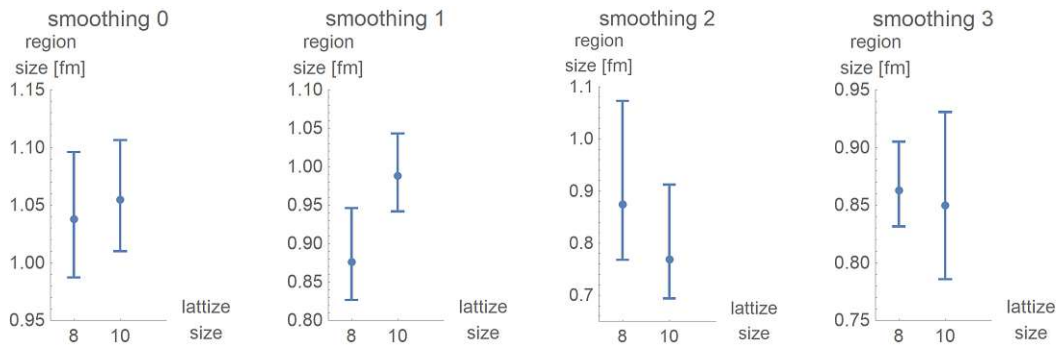


Figure 4.15: After 1 cooling step the extent of homogeneous regions is not significantly bigger than without cooling.

surface clearly above those of the vacuum, see Fig. 4.20. The error bars of the sizes become even larger and no significant further increase can be observed as can be seen in Fig. 4.21.

The last number of cooling steps to be tested is 10. The respective homogeneities are

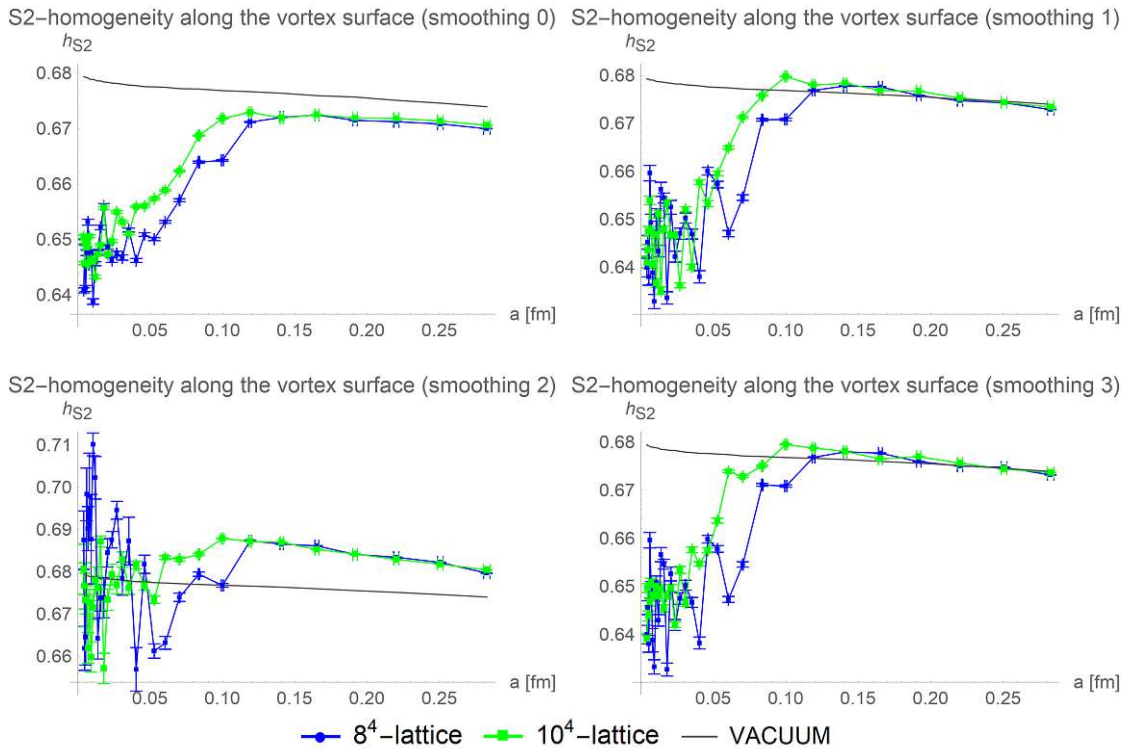


Figure 4.16: Averaged over 100 configurations, the S2-homogeneity along the vortex surface is compared for different lattice sizes and smoothing procedures after 2 cooling steps. Observe that for smoothing 1 and smoothing 3 the homogeneity along the vortex is no longer distinguishable from the vacuum.

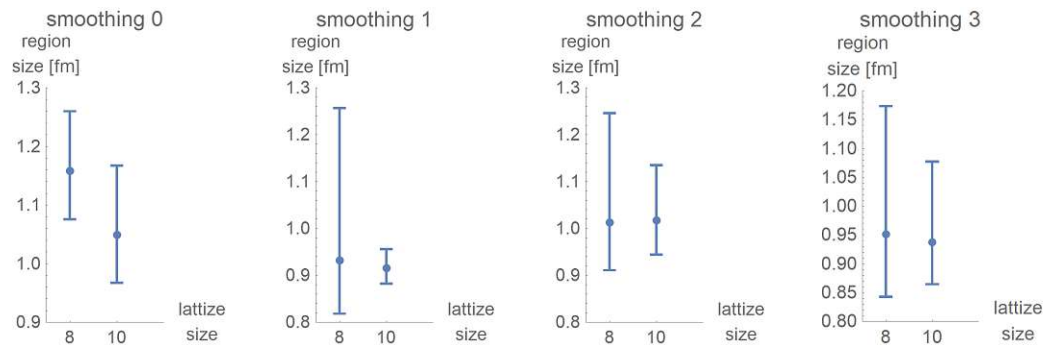


Figure 4.17: After 2 cooling steps only a small increase of the size can be observed.

depicted in Figure 4.22. The size estimates for homogeneous regions can be seen in Fig. 4.23.

To combine the different measurements of lattice sizes and smoothing procedures we interpreted each data point with its error as a set of three datapoints without error and

4. ALGORITHMIC RESTRICTIONS FROM VORTEX PROPERTIES

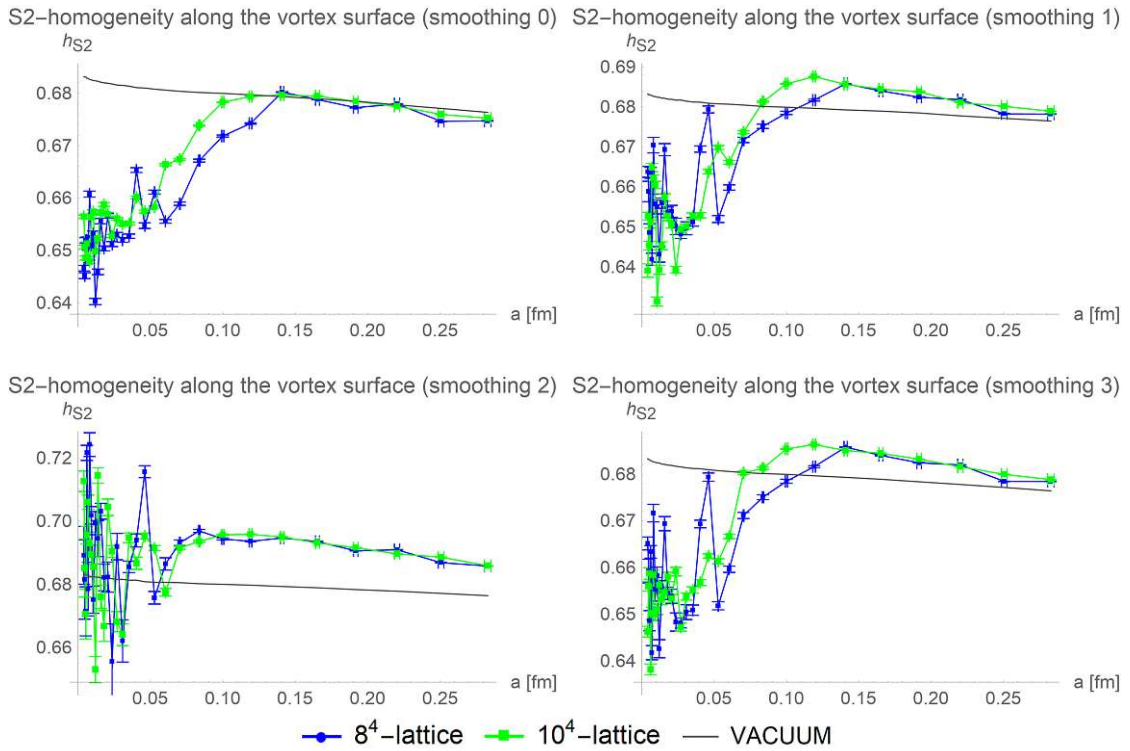


Figure 4.18: Averaged over 100 configurations, the S2-homogeneity along the vortex surface is compared for different lattice sizes and smoothing procedures after 3 cooling steps. Observe that the cooling cause the vortex surface to become more homogeneous than the surrounding vacuum for all smoothing procedures except smoothing 0.

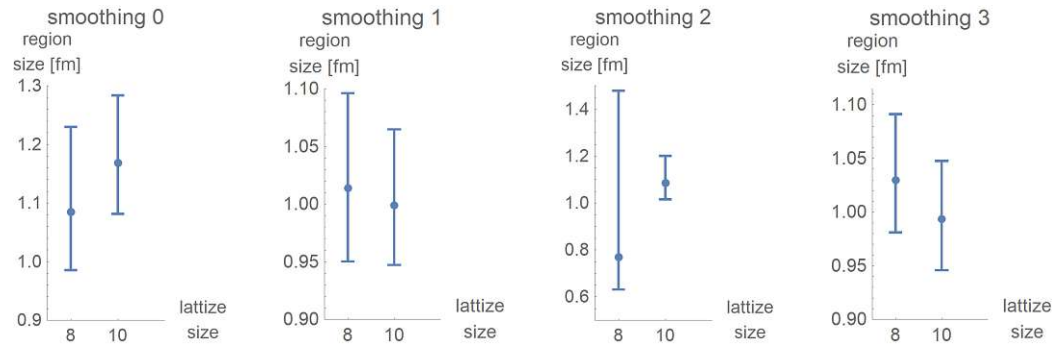


Figure 4.19: After 3 cooling steps the increase of the size seems to slow down.

determine their average and standard deviation for the respective numbers of cooling steps. All data except those from smoothing 2 and the 12^4 lattice are combined to determine the dependence of the size of color homogeneous regions on the number of cooling steps. The results are depicted in Fig. 4.24. Observe that the growth of the

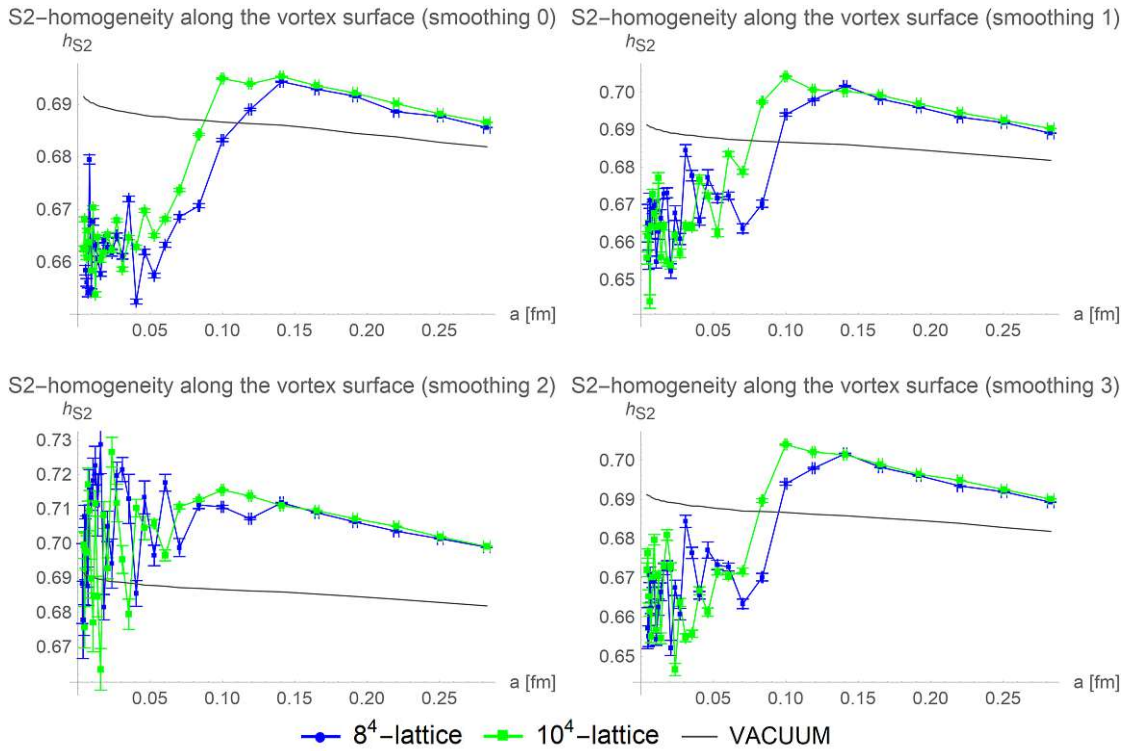


Figure 4.20: Averaged over 100 configurations, the S2-homogeneity along the vortex surface is compared for different lattice sizes and smoothing procedures after 5 cooling steps. Observe that every smoothing procedure results in the vortex being more homogeneous than the surrounding vacuum and the finite size effects persist.

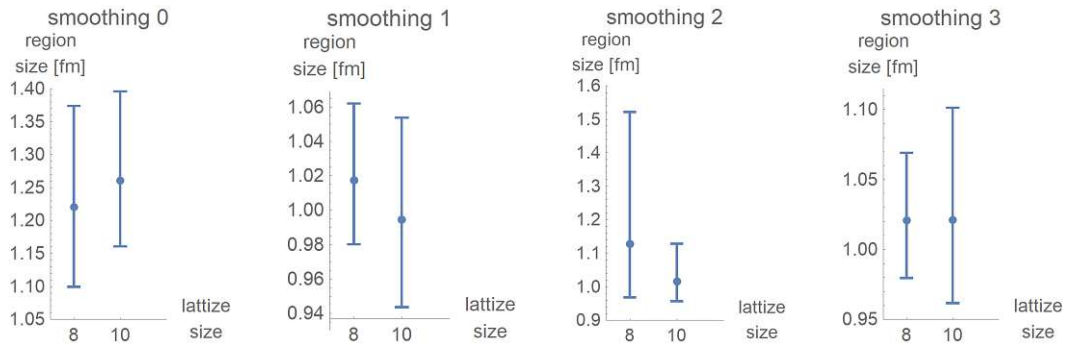


Figure 4.21: After 5 cooling steps, no clear further increase of the size of the color-homogeneous regions can be observed.

homogeneous regions saturates: The regions do not grow arbitrarily large with cooling. This is compatible to the growth of the flux tubes that was discussed in Section 4.1. Thus, we do not need to take a growth of the color homogeneous regions due to cooling

4. ALGORITHMIC RESTRICTIONS FROM VORTEX PROPERTIES

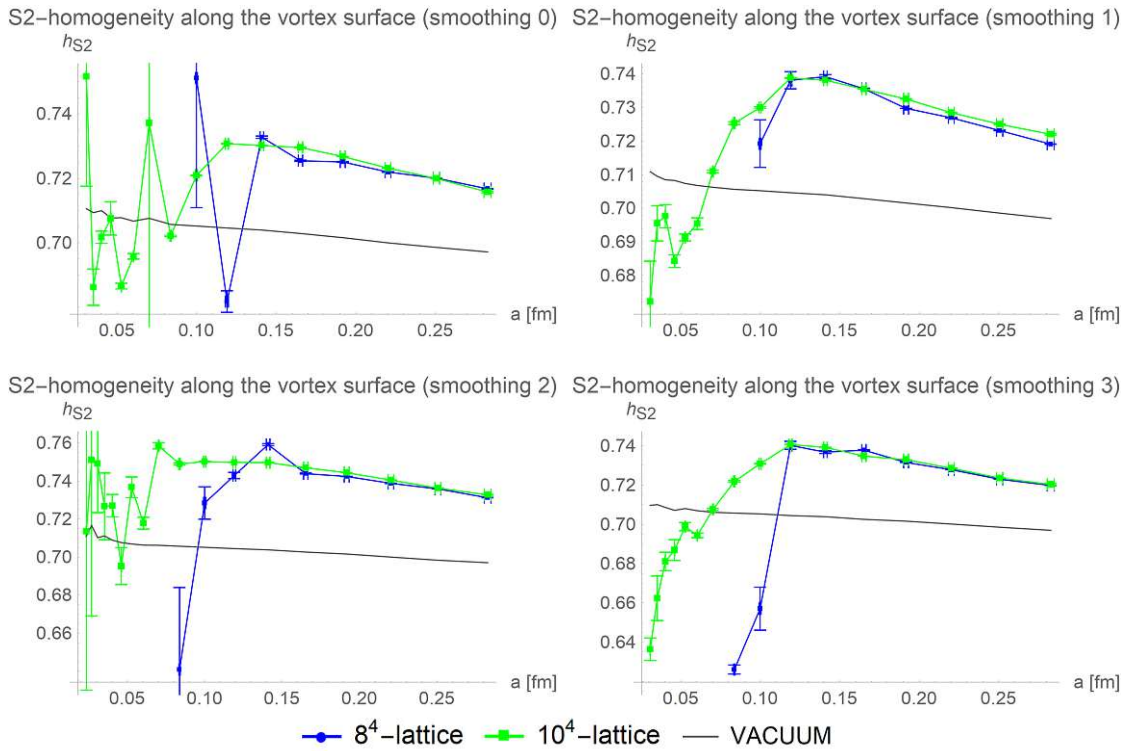


Figure 4.22: Averaged over 100 configurations, the S2-homogeneity along the vortex surface is compared for different lattice sizes and smoothing procedures after 10 cooling steps.

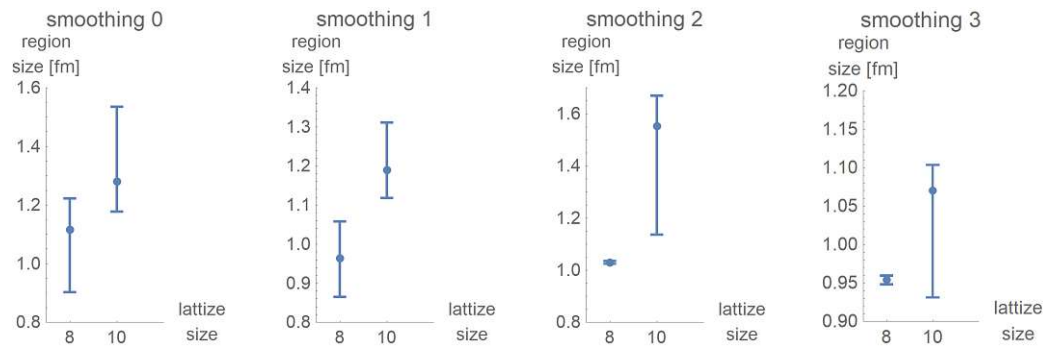


Figure 4.23: After 10 cooling steps one observes that the growth of color homogeneous regions has saturated.

into account and can enforce that the physical lattice extent stays above ≈ 2.3 fm to preserve color homogeneous regions. We obtain the following upper bounds for β in dependence of the lattice size: Including these stronger bounds in the scaling windows as given in Table 4.4, we attain the stronger limits presented in the following.

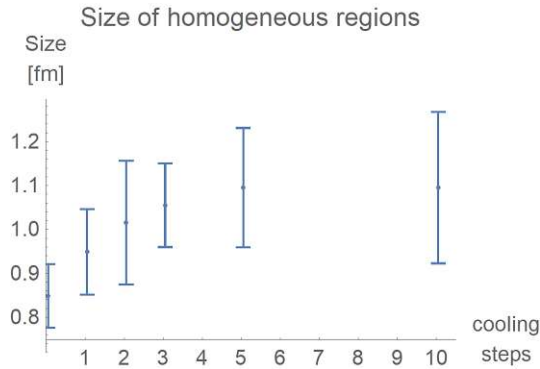


Figure 4.24: The dependence of the size of homogeneous regions on the number of cooling steps is estimated by combining the data from the lattice sizes 8^4 , 10^4 , respective smoothing 0, smoothing 1 and smoothing 3.

Lattice size	10^4	12^4	14^4	20^4	30^4	40^4	50^4
β lower bound	$\lesssim 2.18$	$\lesssim 2.25$	$\lesssim 2.3$	$\lesssim 2.41$	$\lesssim 2.52$	$\lesssim 2.61$	$\lesssim 2.7$

Table 4.5: Upper bounds of β for different lattice sizes to ensure that the lattice is big enough for the color homogeneous regions.

4.3 Combined restrictions

We now take into account the finite size of color-homogeneous regions and the growth of the flux tube due to cooling. The scaling windows given in Table 4.4 get more narrow: A lattice size below 10^4 is no longer trustworthy, the number of possible cooling steps is reduced and the upper limits of β are lowered, see Table 4.6. Within these β -intervals we expect, that the correct scaling behaviour is approached with increasing β . Below these limits the separation between neighbouring flux tubes may be smaller than one lattice spacing. This can cause the vortex detection to fail due to a loss of non-trivial center regions. Above the upper limits of β , the closedness of the flux tubes that build the vortex surface or the extent of color homogeneous regions can come in conflict with the lattice size. The latter may lead to a loss of color structure.

Table 4.6: For different numbers of cooling steps and different lattice extents, the table gives a lower and an upper limit for β based on the more cautious estimates of the cross-section of vortex piercings. “None” indicates that the limits exclude one another. Outside this window a successful vortex detection can not be expected.

$N_{\text{cool}} \setminus L$	10	14	20	30	40	50
0	2.12	2.12	2.12	2.12	2.12	2.12
	2.39	2.48	2.58	2.73	2.84	2.92
1	2.14	2.14	2.14	2.14	2.14	2.14
	2.18	2.3	2.41	2.52	2.61	2.7
2	2.16	2.16	2.16	2.16	2.16	2.16
	2.18	2.3	2.41	2.52	2.61	2.7
3	None	2.19	2.19	2.19	2.19	2.19
		2.3	2.41	2.52	2.61	2.7
5	None	2.23	2.23	2.23	2.23	2.23
		2.3	2.41	2.52	2.61	2.7
10	None	None	2.34	2.34	2.34	2.34
			2.41	2.52	2.61	2.7
15	None	None	None	2.44	2.44	2.44
				2.52	2.61	2.7
20	None	None	None	None	2.54	2.54
					2.61	2.7
25	None	None	None	None	None	2.66
						2.7

Future outlook and perspectives

With the obtained data further possibilities to improve the vortex detection became apparent. Our current implementation is troubled if two thick vortex flux tubes get closer than one lattice spacing. In such a scenario the algorithm may fail to distinguish them and results in the flux tubes being not enclosed by non-trivial center regions. This in turn can cause a loss of P-vortices. It may be counteracted by allowing overlaps of non-trivial center regions during the procedure presented in section 3.1. Uncontrolled overlaps may lead to double counting of regions because they can cause redundant regions to arise from the detection procedures. This can be prevented by limiting the overlaps extent to a single lattice spacing.

In section 4.2 we found that smoothing procedures may cause a loss of color structure, especially, if they modify the topology of the vortex. The identification of thick vortices, that is, the identification of non-trivial center regions that enclose P-plaquettes, could lead to improved smoothing procedures: We expect that the flux line building the P-vortex does not follow exactly the core of the thick flux tube but fluctuates around it. These fluctuations are gauge dependent and relate to a rough vortex surface that can be further smoothed without influencing the topology of the vortex. In the vicinity of perpendicular non-trivial center regions we expect the center flux line to bend along the curved thick vortex flux tube. Smoothing can be accomplished by shifting P-plaquettes within the surrounding non-trivial center region. Finally a minimal vortex surface should be achieved. It should preserve the topology of the vortex whilst resulting in a smooth surface. This could also reduce the gauge dependence of P-vortices preventing gauge ambiguities.

The restrictions on the lattice parameters that were presented in sections 4.1 and 4.2 and combined in section 4.3 may be stronger than required. By testing the scaling behaviour of the string tension one may find that the scaling window is larger than expected. It would be also interesting to test whether the scaling behaviour is reproduced for given number of cooling steps in sufficiently large lattices. With 5 cooling steps the lattice

size required for a full restoration of the string tension should be reachable with present computational power.

When generalizing to $SU(3)$, two different non-trivial center elements need to be taken care of instead of one. This gives rise to splitting and fusing of vortex surfaces. The generalization can be done in two different ways: Either each of the two non-trivial center elements of $SU(3)$ is treated separately, that is, one looks for two different types of non-trivial center regions and considers these two types independent of one another. In this approach, overlaps of non-trivial center regions of different type would be ignored and the gauge fixing procedure needs to fit the flux lines accordingly. No modification of the algorithms for detecting non-trivial center regions would be needed and they could be executed in parallel for the two non-trivial center elements. Another approach could be based on the modification of the growing procedure for non-trivial center regions: instead of letting the region grow so that a specific center-element is approached, one could let the region approach the nearest non-trivial center element in each enlargement step. Each lattice slice would be subdivided into non-overlapping center regions and the Guided Maximal Center gauge could be used without the need of modifications.

Let us now discuss future research possibilities regarding the vortex structure that arise from our notion of the S2-homogeneity. In section 4.2 we looked at finite size effects of the color homogeneity along the vortex surface, but did not distinguish between straight or curved flux. Repeating the measurements for straight and curved surfaces separately would allow to gain more insight on the correlation of curvature and color-structure. This could pave the way for further improvements of the smoothing procedures: it could allow to distinguish irrelevant fluctuations of the vortex surface from fluctuations relevant for the color structure. One could also look for finite size effects in the planar sector, that is, the cross-section of the flux tubes. Such finite size effects would hint at a finite thickness of the vortex surface in the continuum limit.

Let us end now with a recapitulation of the vortex picture as arising from this work:

The vortex surface is built from closed center flux lines evolving in time. On the lattice this flux lines get a finite diameter and a vortex surface of finite thickness is built by flux tubes evolving in time. The flux tubes cross section is homogeneous with respect to the color when compared to the surrounding vacuum, remember the left side of Fig. 4.9. The color along the flux tube is less homogeneous than the surrounding vacuum if the flux tube is curved but more homogeneous if it is straight: Curvature correlates to inhomogeneity. When cooling is applied, the flux tube diameter increases, but this growth seems to have an upper limit as was shown in section 4.1. Also a limited enlargement of color homogeneous regions was found in section 4.2.

The usage of center regions proved successful at the detection of thick center vortices. In combination with the notion of S2-homogeneity it allowed for new analyses of the center vortex structure and opens up possibilities for future research.

List of Figures

1.1	Schematics of color confinement	1
1.2	String-breaking	2
2.1	Weight diagram of $SU(3)$	5
2.2	The threefold symmetry of $SU(3)$	6
2.3	Quarks and anti-quarks in the Y, T_3 plane	6
2.4	Meson structure	9
2.5	Lattice schematics	17
2.6	Gauge invariant operators	19
2.7	$SU(2)$ link and color sphere	20
2.8	A plaquette on the lattice	21
2.9	Finite size effects	22
2.10	Example for finite size effects	23
2.11	Discretization effects	23
2.12	Center transformation	25
2.13	Vortex-Identification	26
2.14	A link and the six plaquettes it belongs to	28
2.15	Pisa cooling	29
2.16	Fat links	31
2.17	Wilson loop and quark anti-quark pair	33
2.18	Measuring color properties	34
2.19	Histograms of S2-homogeneity and S3-homogeneity for different numbers of cooling steps	35
2.20	Vortex sensitivity of S2- and S3-homogeneity for different number of cooling steps	35
2.21	Polyakov loop and quark anti-quark pair	36
3.1	Schematics of the vortex detection procedure	37
3.2	The non-Abelian stokes theorem on the lattice	39
3.3	Factorization of a Wilson loop using center regions	39
3.4	Algorithm for the detection of non-trivial center regions	41
3.5	Algorithm for enlarging regions towards the non-trivial center	42
3.6	Algorithm for the selection of non-trivial center regions	44
3.7	Geometry of a P-vortex	47
		83

3.8	The vortex and the Wilson loop	48
3.9	Smoothing the vortex surface	51
3.10	Curvature of the vortex surface for different numbers of cooling steps	52
3.11	Effect of strong simulated annealing	54
3.12	Comparison of Creutz ratios for guided and original gauge fixing procedure	55
3.13	string tension for different lattice sizes over wide range of β	56
3.14	String tension in dependence of β with cooling applied	56
3.15	Proportion of failed gauge fixing procedures	57
4.1	Area scaling on the lattice	60
4.2	Average flux tube cross-section	60
4.3	Maximal flux tube cross-section	61
4.4	Fits to average flux tube cross-sections	63
4.5	Fits to maximal flux tube cross-sections	64
4.6	Wilson loop area and piercing separation	65
4.7	Loss of vortex density due to cooling	66
4.8	Limits on the lattice parameters	67
4.9	Planar and longitudinal color-homogeneity of the vortex	70
4.10	Homogeneity difference for straight and curved flux lines	71
4.11	Fitting procedure for the identification of the onset of finite size effects	71
4.12	Longitudinal color homogeneity	72
4.13	Size of color-homogeneous region with no cooling applied	73
4.14	Longitudinal color homogeneity (1 cooling steps)	74
4.15	Size of color-homogeneous regions after 1 cooling steps	74
4.16	Longitudinal color homogeneity (2 cooling steps)	75
4.17	Size of color-homogeneous regions after 2 cooling steps	75
4.18	Longitudinal color homogeneity (3 cooling steps)	76
4.19	Size of color-homogeneous regions after 3 cooling steps	76
4.20	Longitudinal color homogeneity (5 cooling steps)	77
4.21	Size of color-homogeneous regions after 5 cooling steps	77
4.22	Longitudinal color homogeneity (10 cooling steps)	78
4.23	Size of color-homogeneous regions after 10 cooling steps	78
4.24	Size of color-homogeneous regions in dependence of the number of cooling steps	79

List of Algorithms

2.1	SU(2) Wilson action	21
2.2	Markov Chain of configurations according to the path integral	30
3.1	Detection of non-trivial center regions	43
3.2	Selection of non-trivial center regions	45
3.3	Guided Maximal Center Gauge	49
3.4	Reconstruction of thick vortices from P-plaquettes.	53

Bibliography

- [1] V.G. Bornyakov, D.A. Komarov, and M.I. Polikarpov. P-vortices and drama of gribov copies. *Physics Letters B*, 497(1-2):151–158, Jan 2001.
- [2] V. G. Bornyakov, D. A. Komarov, M. I. Polikarpov, and A. I. Veselov. P vortices, nexuses and effects of Gribov copies in the center gauges. In *Quantum chromodynamics and color confinement. Proceedings, International Symposium, Confinement 2000, Osaka, Japan, March 7-10, 2000*, pages 133–140, 2002.
- [3] P.A. Zyla et al. Review of Particle Physics. *PTEP*, 2020(8):083C01, 2020.
- [4] C. Gattringer and C.B. Lang. *Quantum Chromodynamics on the Lattice: An Introductory Presentation*. Springer-Verlag, 2010.
- [5] M. Luscher. Topology of Lattice Gauge Fields. *Commun. Math. Phys.*, 85:39, 1982.
- [6] T. Banks and A. Casher. Chiral symmetry breaking in confining theories. *Nuclear Physics B*, 169(1):103–125, 1980.
- [7] M. F. Atiyah and I. M. Singer. The index of elliptic operators on compact manifolds. *Bull. Am. Math. Soc.*, 69:422–433, 1969.
- [8] Roman Höllwieser, Thomas Schweigler, Manfred Faber, and Urs M. Heller. Center vortices and topological charge. *PoS, ConfinementX:078*, 2012.
- [9] Kenneth G. Wilson. Confinement of quarks. *Phys. Rev. D*, 10:2445–2459, Oct 1974.
- [10] P. Weisz. Continuum limit improved lattice action for pure yang-mills theory (i). *Nuclear Physics B*, 212(1):1 – 17, 1983.
- [11] G. Curci, P. Menotti, and G. Paffuti. Symanzik’s improved lagrangian for lattice gauge theory. *Physics Letters B*, 130(3-4):205–208, Oct 1983.
- [12] Rudolf Golubich and Manfred Faber. Properties of su(2) center vortex structure in smooth configurations. *Particles*, 2021.
- [13] G. E. P. Box and Mervin E. Muller. A Note on the Generation of Random Normal Deviates. *The Annals of Mathematical Statistics*, 29(2):610 – 611, 1958.

- [14] Massimo Campostrini, Adriano Di Giacomo, Michele Maggiore, Haralambos Panagopoulos, and Ettore Vicari. Cooling and the String Tension in Lattice Gauge Theories. *Phys. Lett. B*, 225:403–406, 1989.
- [15] W. Bietenholz. Convergence rate and locality of improved overlap fermions. *Nuclear Physics B*, 644(1-2):223–247, Nov 2002.
- [16] J. B. Zhang, Peter J. Moran, Patrick O. Bowman, Derek B. Leinweber, and Anthony G. Williams. Stout-link smearing in lattice fermion actions. *Physical Review D*, 80(7), Oct 2009.
- [17] Colin Morningstar and Mike Peardon. Analytic smearing of $su(3)$ link variables in lattice qcd. *Physical Review D*, 69(5), Mar 2004.
- [18] Martin Lüscher. Properties and uses of the wilson flow in lattice qcd. *Journal of High Energy Physics*, 2010(8), Aug 2010.
- [19] R. Sommer. A new way to set the energy scale in lattice gauge theories and its application to the static force and α_s in $su(2)$ yang-mills theory. *Nuclear Physics B*, 411(2-3):839–854, Jan 1994.
- [20] Jeff Greensite. *An introduction to the confinement problem*, volume 821. 2011.
- [21] Rudolf Golubich and Manfred Faber. Vortex model of the qcd-vacuum — successes and problems. *Acta Physica Polonica B Proceedings Supplement*, 2018.
- [22] Rudolf Golubich and Manfred Faber. Improving center vortex detection by usage of center regions as guidance for the direct maximal center gauge. *Particles*, 2019.
- [23] Rudolf Golubich and Manfred Faber. The Road to Solving the Gribov Problem of the Center Vortex Model in Quantum Chromodynamics. *Acta Physica Polonica B Proceedings Supplement*, 13:59–65, 2020.
- [24] R. Golubich and M. Faber. Center regions as a solution to the gribov problem of the center vortex model. *Acta Physica Polonica B Proceedings Supplement*, 14(1):87, 2021.
- [25] Boguslaw Broda. Non-abelian stokes theorem. 12 1995.
- [26] L. Del Debbio, Manfred Faber, J. Giedt, J. Greensite, and S. Olejnik. Detection of center vortices in the lattice Yang-Mills vacuum. *Phys. Rev.*, D58:094501, 1998.
- [27] Roman Bertle. The vortex model in lattice quantum chromo dynamics, Sept. 2005. doctoral thesis.
- [28] R. Bertle, Manfred Faber, J. Greensite, and S. Olejnik. The Structure of projected center vortices in lattice gauge theory. *JHEP*, 03:019, 1999.

- [29] Gunnar S. Bali, Christoph Schlichter, and Klaus Schilling. Observing long color flux tubes in $su(2)$ lattice gauge theory. *Physical Review D*, 51(9):5165–5198, May 1995.
- [30] S. P. Booth, A. Hulsebos, A. C. Irving, A. McKerrell, Christopher Michael, P. S. Spencer, and P. W. Stephenson. $SU(2)$ potentials from large lattices. *Nucl. Phys.*, B394:509–526, 1993.
- [31] Christopher Michael and M. Teper. Towards the Continuum Limit of $SU(2)$ Lattice Gauge Theory. *Phys. Lett.*, B199:95–100, 1987.
- [32] S. Perantonis, A. Huntley, and Christopher Michael. Static Potentials From Pure $SU(2)$ Lattice Gauge Theory. *Nucl. Phys.*, B326:544–556, 1989.
- [33] G. S. Bali, J. Fingberg, Urs M. Heller, F. Karsch, and K. Schilling. The Spatial string tension in the deconfined phase of the $(3+1)$ -dimensional $SU(2)$ gauge theory. *Phys. Rev. Lett.*, 71:3059–3062, 1993.
- [34] Rudolf Golubich and Manfred Faber. Thickness and color structure of center vortices in gluonic $SU(2)$ QCD. *Particles*, 3(2):444–455, may 2020.
- [35] Rudolf Golubich and Manfred Faber. A possible resolution to troubles of $su(2)$ center vortex detection in smooth lattice configurations. *Universe*, 2021.
- [36] Roman Höllwieser, Thomas Schweigler, Manfred Faber, and Urs M. Heller. Center Vortices and Chiral Symmetry Breaking in $SU(2)$ Lattice Gauge Theory. *Phys. Rev.*, D88:114505, 2013.
- [37] Roman Höllwieser, Manfred Faber, Thomas Schweigler, and Urs M. Heller. Chiral symmetry breaking from center vortices, 2014.